A Conjunction of Spheres:
Colloidal Quantum Dot Microlasers Towards Chipscale Biosensors

PhD Thesis

Bethan K. Charlton
Department of Physics
University of Strathclyde, Glasgow

23rd February 2026

Declaration

This thesis is the result of the author's original research. It has been composed by the author and has not been previously submitted for examination which has led to the award of a degree.

The copyright of this thesis belongs to the author under the terms of the United Kingdom Copyright Acts as qualified by University of Strathclyde Regulation 3.50. Due acknowledgement must always be made of the use of any material contained in, or derived from, this thesis.

Signed: B Charlton

Date: 23/02/2026

Abstract

Biosensing is one of the most important current areas of research with the COVID-19 pandemic highlighting the need for easy to use, reliable, and portable biosensors. Whispering Gallery Mode (WGM) lasers have been a popular choice for biosensing research due to their capability for label-free sensing, rapid detection response, high sensitivity, and high signal to noise ratio when operating above the lasing threshold. Colloidal Quantum Dots (CQDs) are an important class of new material and are attractive for use in lasers due to their high density of states, high photostability, and high quantum yield. In 2018, the fabrication of microspheres consisting entirely of CQDs, called supraparticles (SPs), which could demonstrate WGM lasing was first published and inspired a new area of research due to their promising use as tiny lasers. In this work, the focus was on the use of these CQD supraparticles (SPs) as laser biosensors because the microscale size of these SP lasers would enable their integration into a microfluidic chip to create easy to use and portable devices. First, the fabrication of these SPs was achieved using an emulsion templated fabrication, along with two additional variants, yielding SPs with laser thresholds as low as 4.1 ± 0.4 mJ/cm^2 under free space excitation. To be able to use these SPs as laser biosensors, SPs were modified with the protein Neutravidin and a DNA aptamer with 15 bases called the Thrombin Binding Aptamer (TBA-15). Both Neutravidin-coated SPs and TBA-15 coated SPs (TBA-SPs) retained lasing functionality post- functionalisation with thresholds of 25.1 ± 3.5 mJ/cm^2 and 19.8 ± 2.7 mJ/cm^2, respectively. Finally, a crude study to demonstrate biosensing capabilities of TBA-SPs for the protein thrombin in solution, with a possible detection limit around 1.5 mg/mL. This is an exciting new development which can act as a platform for further study and to create a lab on a chip sensing device.

Contents

List of Figures

List of Tables

List of Abbreviations

3S-SP	Supraparticle synthesised using the 3 Surfactant Method
ANOVA	Analysis of Variance
AR	Auger Recombination
BSA	Bovine Serum Albumin
CQD	Colloidal Quantum Dots
DMF	Dimethyl Formamide
EDC	*N*-(3-Dimethylaminopropyl)-*N'*-ethyl carbodiimide
FTIR	Fourier Transform Infrared Spectroscopy
FWHM	Full Width Half Maximum
HEC	Hydroxyethyl Cellulose
LoD	Limit of Detection
LTF	Laser Transfer Function
MPA	3-Mercaptopropionic Acid
MPA-SP	MPA-capped Supraparticle
Neut-SP	Neutravidin-capped Supraparticle
NHS	*N*-Hydroxysuccinimide
OA	Oleic acid
OA-SP	Oleic acid-capped Supraparticle
O/W	Oil-in-water Emulsion
O/W/O	Oil-in-water-in-oil Emulsion
PBS	Phosphate buffered saline
PDMS	Poly(dimethyl siloxane)
PL	Photoluminescence

PVA	Poly(vinyl alcohol)
PVA-SP	Supraparticle synthesised using the Emulsion method
QCE	Quantum Confinement Effect
SDS	Sodium Dodecyl Sulfate
SF-SP	Supraparticle synthesised using the Surfactant Free method
SEM	Scanning Electron Microscope
SP	Supraparticle
TBA-15	Thrombin Binding Aptamer containing 15 bases
TBA-SP	Supraparticle capped with Thrombin Binding Aptamer
TIR	Total Internal Reflection
WGM	Whispering Gallery Mode
W/O	Water-in-oil Emulsion
W/O/W	Water-in-oil-in-water Emulsion

Acknowledgements

First and foremost I would like to acknowledge Dr. Nicolas Laurand for granting me the opportunity to conduct this PhD. I would also like to thank him for his endless patience, fantastic advice, and kind and relaxed approach to academic research and supervision. Even with the difficult start during the pandemic, his skill for transmitting support, knowledge, and guidance through a single zoom call remains unmatched. I would also like to thank Dr. Charlotte Eling without whom I could not have got through this PhD, she is truly a fantastic researcher and colleague who is always ready to give out advice and guidance whenever it is needed.

I would also like to thank our research group. It has been a pleasure to work with such a collaborative, open, and supportive group of people, particularly as moving to a whole new city (and changing subjects!) is quite a daunting experience. I am specifically going to name and shame Dillon Downie, Emma McCormick, and Becca Craig because the daily coffee and chaotic chat was an integral part of my PhD experience and certainly kept me (and I think all of us) going through the more frustrating research periods.

To my parents, Meg and Aidy, thank you again for all of the support you have shown me throughout this PhD and beyond. My mam in particular for the good natured nagging at the final push to finish this thesis. To my dad, I hope this thesis acts as a sufficient replacement for getting a real job. To my partner Reece, thank you for putting up with me, moving to Glasgow, and showing up daily to provide all the love and support I could ever need. To our cat Terra, thanks for the 6 am wake ups and near constant yelling while writing this thesis.

Finally, to my grandfather Tony Edwards for showing me that common sense is not a requirement to complete a PhD.

Mitigating Circumstances

This project was started in October 2020 during the COVID-19 pandemic. This meant that due to lockdown restrictions and workplace capacity restrictions, the laboratory work detailed in this thesis could not begin until August 2021. After 2021, it took another few months for these restrictions to ease further, meaning that for that period of time the laboratory could only be accessed for up to two days a week due to five people needing to conduct their own experiments. The majority of time during this PhD was spent working on the different methods of producing SPs and developing the subsequent surface functionalisation procedure. Building the optical setup for the biosensing tests along with the experiments themselves was done towards the latter 6 months of the project, with other delays due to the pump laser (along with the backup) breaking down for 2-3 months and needing to be sent away for repairs.

Chapter 1

Introduction

1.1 Aims and Objectives

The main aims and objectives of this PhD was to be able to produce self assembled supraparticle microlasers using emulsion templated self assembly, and be able to suitable alter the surface chemistry to be able to use these SPs in sensing applications. A further original aim was to be able to integrate these SP microlasers into optical substrates, with creating flexible, wearable devices as a possible goal. The objectives of this project did evolve as more time was able to be spent in the laboratory where the main goal ended up being focused on demonstrating successful surface functionalisation, which took longer than expected due to difficulties with the stability of SPs in buffer solutions and at higher pHs required for EDC/NHS coupling in addition to some difficulties collecting suitable characterisation data. Initially, the idea was to functionalise the SP surface with Neutravidin to be able to exploit the avidin-biotin interaction for the sensing mechanism, however limiting the size of molecules attached to the surface of SPs became a concern, meaning this objective altered to functionalising SPs with a DNA aptamer using EDC/NHS coupling. Before this research, surface functionalisation of SPs such as these had not yet been demonstrated and makes this a scientific contribution that can act as a platform from which functional laser biosensors from these SP microlasers could be developed. In terms of demonstrating successful biosensing, this goal was not fully realised, with these experiments would requiring an improved design, for example encasing SPs in a small chamber within a simple microfluidic cell to be able to introduce different sample solutions more effectively and obtain more stable PL spectra.

1.2 Motivation and Rationale

For decades, the development of rapid and reliable testing for cancer and various other diseases has been a major research focus, particularly as a result of the pandemic and the longer waiting time for diagnoses. As a result of growing healthcare needs both nationally and globally, biosensing is a huge area of research potential and innovation. A recent innovation in photonics with the potential for biosensing is the fabrication of optically active microspheres constructed entirely of colloidal quantum dots (CQDs), hence the name supraparticle (SP) lasers. [1] These SPs could be used as tiny lasers in solution and in lab on a chip configurations. These microsphere lasers work using whispering gallery modes (WGM), where the high refractive index of the CQDs that make up the microlaser comparative to the surrounding environment means light can be 'captured', then travels around the equator of the cavity through total internal reflection and becomes in phase with itself to produce whispering gallery modes. As a result of the CQDs acting as both the resonant cavity and the gain medium, these microspheres can act as tiny, free floating laser which can be optically excited by a remote light source rather than the precise excitation usually required for passive whispering gallery mode resonators in photonics. The strong resonances produced by WGMs in such small volumes enhance light-matter interactions and through their evanescent field are very sensitive to changes at the surface and immediate surrounding environment of WGM resonators, making them suitable for sensing applications. In addition to the high sensitivity that can be achieved using WGM sensors, the ability to pump these lasers from a remote source opens up new possibilities for creating microscale biosensing chips with multiple microsphere lasers being excited simultaneously to sense for different biomarkers that may be present in single samples, for example testing for multiple protein biomarkers that may be present in blood. Using WGM microsphere lasers made entirely out of CQDs also streamlines and simplifies the cavity production process which, until now, has meant fabricating the cavity, then incorporating the optically active gain medium into the cavity separately - a less efficient strategy that can also limit the optical performance of such microsphere lasers. At time of writing, no literature has been published demonstrating the use of self-assembled CQD microsphere lasers for biosensing. In this context, this thesis investigates colloidal quantum dot supraparticle microlasers and their bio-functionalisation with the aim to assess and progress their capability for biosensing. The rest of this Chapter gives an overview of the key concepts, elements and state-of-the-art research within this field.

1.3 Colloidal Quantum Dots

1.3.1 Background

Quantum dots (QDs) are semiconductor nanocrystals with a diameter in the order of a few nanometres that were first synthesised in the 1980s. Due to their size, QDs exhibit quantum confinement in all three dimensions which gives QDs unique physical, electronic and optical properties. One of the most well documented properties is the ability to alter the band gap, and from that the emission wavelength, by controlling the size of the crystal which allows QDs to be used in a wide variety of different optical applications. Since the first publication regarding QDs, there has been tens of thousands of articles published on QDs as they are an important class of new material with huge scope for future applications. [2] The importance of these nanocrystals was further acknowledged in 2023 with the Nobel Prize in Chemistry awarded to Yekimov, Brus and Bawendi for their discovery of QDs and the Quantum Confinement Effect (QCE) [3, 4] and development of colloidal quantum dots (CQDs). [5]

High temperature colloidal synthesis of quantum dots was developed to create monodisperse colloidal quantum dots (CQDs) with a high level of control over the resulting size of the CQDs produced. This simple and scalable method paved the way for widespread studies on the properties and applications of CQDs with CQDs now readily available from a variety of different suppliers in a full range of colours. [6] Another class of QDs are epitaxial quantum dots that are synthesised using epitaxial crystal growth where thin crystal layers are formed on top of a thick substrate. [7, 8] CQDs are, in many cases, the favoured class of QD because of the low cost further solution processing capabilities, and the resulting crystal being better quality for optical applications. [8] By altering the conditions of the colloidal synthesis, alternative CQD structures can be obtained, including nanorods [9], dumbbells [10], nanoplatelets [11], and even tetrapods. [12]

QDs are also attractive for use in lasers due to their high density of states, lower gain temperature dependence, high quantum yield and great photostability. [13] Achieving the population inversion required for lasing proved more complex in CQDs than originally thought with stimulated emission only being reported for the first time in 2000. Since this demonstration, research into CQD lasers has increased dramatically due to the potentially superior laser performance with lower thresholds and low-cost solution processability. CQD lasers have a huge scope for future applications in photonic circuits, ultrathin and flexible displays, and sensing. [14] Until recently, using CQDs as gain material for lasers has involved separate fabrication of the lasing cavity using expensive top down methods, such as lithography, and the resulting cavity is often difficult to manipulate. Fabricating lasers on a microscopic scale with few defects is also challenging when using a top-down approach. A recent development in the field of CQD lasers has been the bottom-up fabrication of spherical supraparticles (SPs) through an emulsion technique where the SP acts as both the lasing medium and the cavity to demonstrate whispering gallery mode (WGM) lasing which is extremely promising for sensing applications. [1]

QD nanocrystals are comprised of hundreds to hundreds of thousands of atoms that display a mixture of solid-state and atomic properties due to their mesoscopic scale and are often referred to as artificial atoms. Due to the quantum confinement effect, the wavelength of light emitted and absorbed from CQDs depends on the radius of the crystal. [15] Confined structures are classified by dimensionality. In the case of CQDs, electrons have no degrees of freedom, or experience confinement in three dimensions, therefore CQDs are classed as 0-dimensional structures. This means the motion of the electron in the CQD is localised within the nanocrystal, resulting in the breakdown of continuous energy bands of a bulk semiconductor into discrete, quantised energy levels. [7, 15]

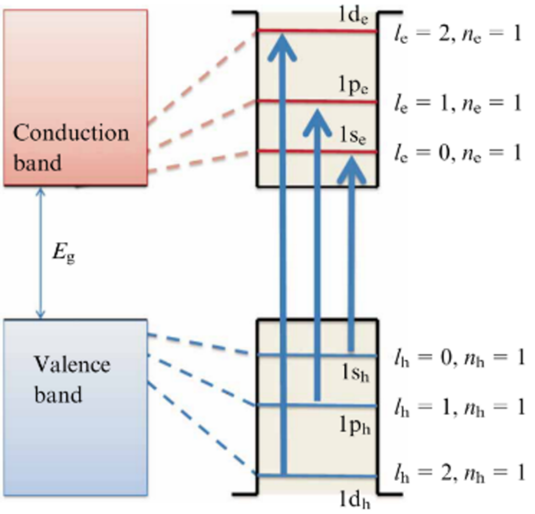

Figure 1.1: Electronic structure of a bulk semiconductor (left) and the electronic structure of QDs with electronic transitions between the electron and hole states that can be calculated using equation 1.2. Reproduced with permission from [6].

This phenomenon is known as the quantum confinement effect (QCE) and explains why the optical properties of QDs depend on the size of the crystal. When an electron is excited from the ground state to an excited state, a positively charged 'hole' is formed in the state that the electron had previously occupied. In nanocrystals, the electron and hole are physically close enough to each other to experience coulombic attraction and can be therefore treated together – known as an exciton. The Bohr radius of an exciton is determined by the coulomb interaction between the electron and hole that make up the exciton. [2, 15] QCE is exhibited in nanocrystals because at this size, the crystal is comparable to the de Broglie wavelength of the electron and hole wavefunctions and the Bohr radius of the excitons. Calculating the spacing and value of the energy levels in a QD cube can be done using the particle in a box model giving the equation:

$$E(n_x, n_y, n_z) = \frac{\pi^2 \hbar^2}{2m_e} \left(\frac{n_x^2}{d_x^2} + \frac{n_y^2}{d_y^2} + \frac{n_z^2}{d_z^2} \right) \tag{1.1}$$

where m_e is the effective mass of an electron and n_x, n_y and n_z are the integer quantum numbers specifying the quantized levels in three dimensions. Adapting and simplifying this equation for spherical dots by using spherical polar coordinates and solving the radial Schrödinger equation generates equation 1.2 below, showing that electron energy levels are proportional to $\frac{1}{R^2}$, which demonstrates the relationship between the energy levels and the radius of the CQD nanocrystal. C_{nl} is a constant and these values for the bound states in a spherical QD can be found within literature. [7] Quantum numbers n and l of the electronic states in QDs are shown in Figure 1.1, along with corresponding allowed transitions. [7, 15, 16]

$$E_{nl} = \frac{\hbar^2}{2m_e} \frac{C_{nl}^2 \pi^2}{R^2} \tag{1.2}$$

For absorption spectra, the particle in a box model can also be used to obtain an expression for the absorption edge which is the energy difference between the first confined states of the electron and hole, corresponding to the transition with the shortest arrow in Fig. 1.1:

$$\hbar\omega \approx E_g + \frac{\pi^2 \hbar^2}{\mu d_{CQD}^2} - E_{ex} \tag{1.3}$$

where μ is the exciton reduced mass, d_{CQD} is the diameter of the CQD, E_g is the bandgap of the bulk material and E_{ex} is the exciton binding energy. This equation also demonstrates the relationship between the energy of the absorption edge and the CQD size. [7] It is also important to note that the fluorescence of CQDs can also be tuned by altering the crystal diameter. Fluorescence in CQDs mostly comes from the lowest transition, however there is a Stokes shift, as shown in Fig. 1.2. This Stokes shift arises from the energy difference between bright and dark excitons, arising from the excitonic fine structure of the lowest transition and spin selection rules. [17]

The electronic properties of CQDs can be improved by coating the surface with a layer of an inorganic semiconductor that has a wider bandgap which can passivate the CQD surface and prevents electrons or holes being trapped in the orbitals of otherwise unsaturated surface bonds. Surface passivation increases quantum yields because when electrons and holes are less likely to be trapped at the surface, the probability of radiative decay occurring increases. The shell also acts as a physical barrier which makes the CQD less prone to changes in the surrounding environment and surface chemistry. CdSe/ZnS and CdSe/CdS CQDs are among the most popular of these core/shell structures and have reached quantum yields of 50% and 85% respectively. [2]

For optical gain to occur in CQDs, a population inversion needs to be achieved where more electrons are in the excited state than in the ground state. CQDs can be treated

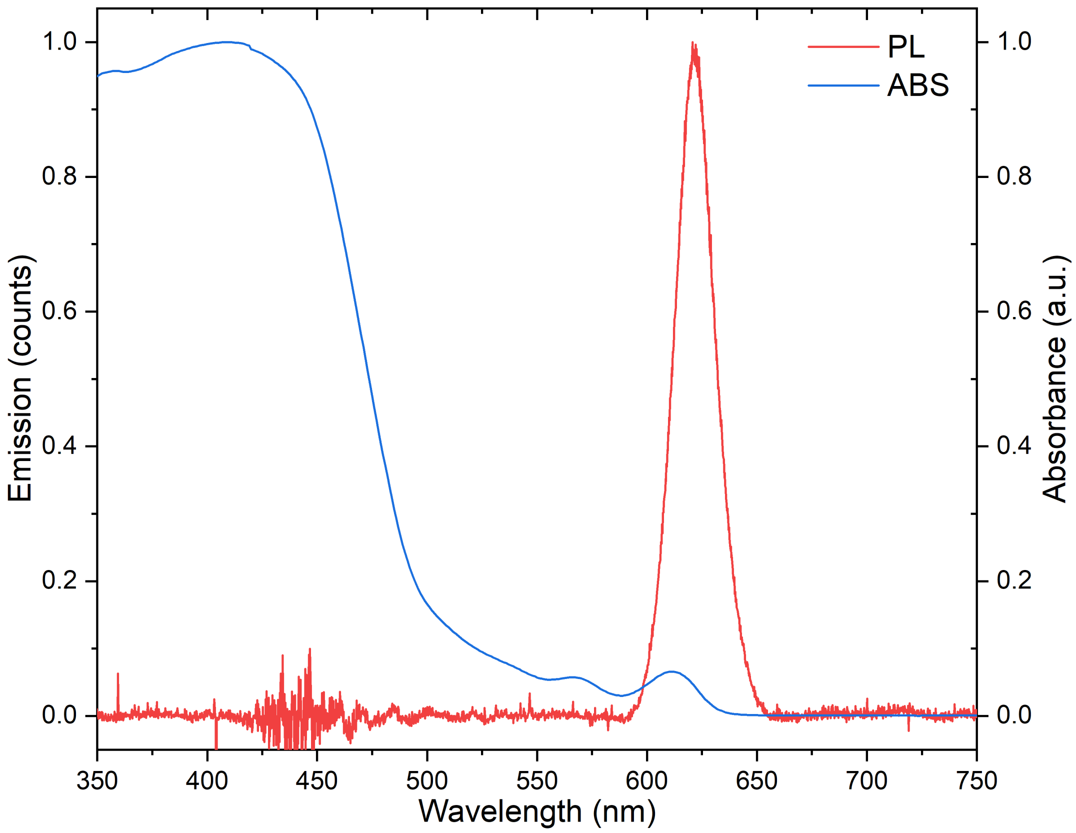

Figure 1.2: Absorbance (blue line) and photoluminescence spectra of the 630 nm CQDs used in this work. The noise between approximately 425−450 nm is an artefact from removing the PL peak of the pump laser from the spectrum.

as a two-level system where both electrons from the ground state must be excited, therefore optical gain in CQDs originates from dots containing a pair of excitons, also referred to as a biexciton. [15] One of the factors that has hindered the development of CQD lasers is the increased rate of Auger Recombination (AR) in CQDs. AR is a non-radiative decay process where an exciton recombines and the energy released is absorbed by an electron or hole in the other exciton instead of being released as a photon. This process is present in bulk semiconductors, however the problem is exacerbated in CQDs as a result of the proximity between excitons in the nanocrystals. [14] The rate of AR is inversely proportional to the volume of CQDs because the rate depends on the strength of the coulombic interaction between the carriers and the degree of spatial overlap between the electron and hole wave functions. At small volumes, several excitons can occupy a volume comparable to or smaller than the volume of the bulk exciton, which leads to the forced overlap of wave functions. [18, 19] Another hindrance in achieving optical gain in CQDs is that the AR rate also rapidly increases with the number of excitons; a problem due to the fact biexcitons are required to achieve net optical gain. Biexcitons in CdSe CQDs were found to have interaction energies in the order of tens and hundreds of meV in comparison to the binding energy of 4.5 meV in bulk CdSe , demonstrating the huge increase in coulombic exciton-exciton interactions induced by quantum confinement. [20] As an overall result of both of these factors, AR occurs on 10-400 ps timescales depending on dot size and design, whereas radiative decay occurs on approximately 20-30 ns timescales. However, the requirement for both AR and optical gain is the presence of a biexciton in the CQD core meaning AR will always be a limiting factor on optical gain lifetimes. [15]

1.3.2 Lasing in Colloidal Quantum Dots

Suppression of AR rates in CQDs was first demonstrated with giant shell CdSe/CdS CQDs in 2009. These core/shell dots achieved biexciton lifetimes of 10 ns compared to as low as 6 ps from core only CdSe dots, demonstrating the importance of the shell when attempting to achieve optical gain. In this study, Garcia-Santamaria *et. al.* used dots with a 3 nm CdSe core with a CdS shell up to 19 monolayers thick. One of the major factors in the demonstrated AR suppression was the reduced spatial overlap of the electron-hole wavefunctions because the hole is confined to the core of the CQD while the excited electron can delocalise and move freely throughout the shell, reducing the ease of exciton recombination. After the shell was deposited on the core, a large photoluminescence (PL) redshift was observed which was also attributed to this delocalisation of the electron and confinement of the hole. This also contributes to an increased absorption cross-section at higher energies where the high-frequency absorption is dominated by the shell. Amplified spontaneous emission measurements also indicated a very large bandwidth of optical gain which is a result of contributions from high order multiexcitons, in some cases as high as $N > 13$ where N is the number of excitons per CQD, further demonstrating the remarkable suppression of AR decay rates.

Garcia-Santamaria *et. al.* noted that the factors of increased volume, reduced electron-hole overlap and exciton-exciton repulsion were insufficient to explain the observed reduction in AR rates hence posited that interfacial effects of the CdSe/CdS CQDs also play an important part in this suppression in a similar way to epitaxial QDs. [21]

A later study confirmed the importance of the core/shell interface in the suppression of AR rates in CdSe/CdS core/shell CQDs and built on the evidence of the factors contributing to AR suppression. Using fluorescence line narrowing studies, the presence and growth of the alloyed CdSeS layer can be detected and monitored. An alloyed layer was formed between 2 and 9 monolayers of shell thickness as a bridge between the core and shell layers of the CQDs, and increased biexciton lifetimes were observed as the shell thickness exceeded 9 monolayers. A band alignment diagram was constructed and showed that there is a large valence band offset between the core and shell along with a small confinement potential in the conduction band. This, together with the small electron effective mass, causes the delocalisation of the electron wavefunction into the shell as shell size increases. Therefore, as the shell size increases, the electron becomes more delocalised, redshifting the emission band and causing the absorption to become

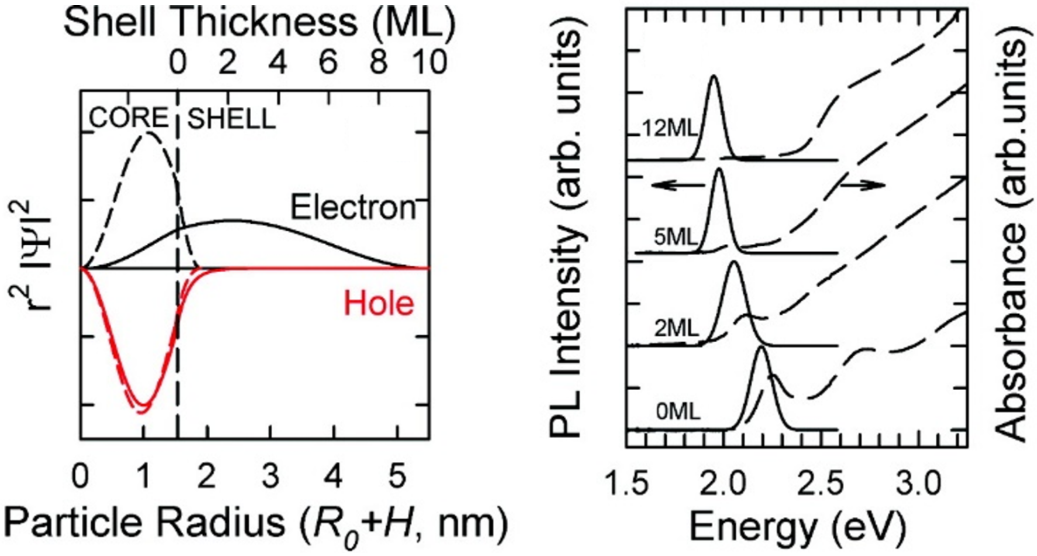

Figure 1.3: (a) Probability distribution of the electron (red) and hole (black) for CdSe/CdS CQDs with thin (dashed) and thick (solid) CdS shells. (b) Absorption (dashed) and photoluminescence (solid) spectra of CdSe/CdS CQDs with increasing shell thickness. Reproduced with permission from [18].

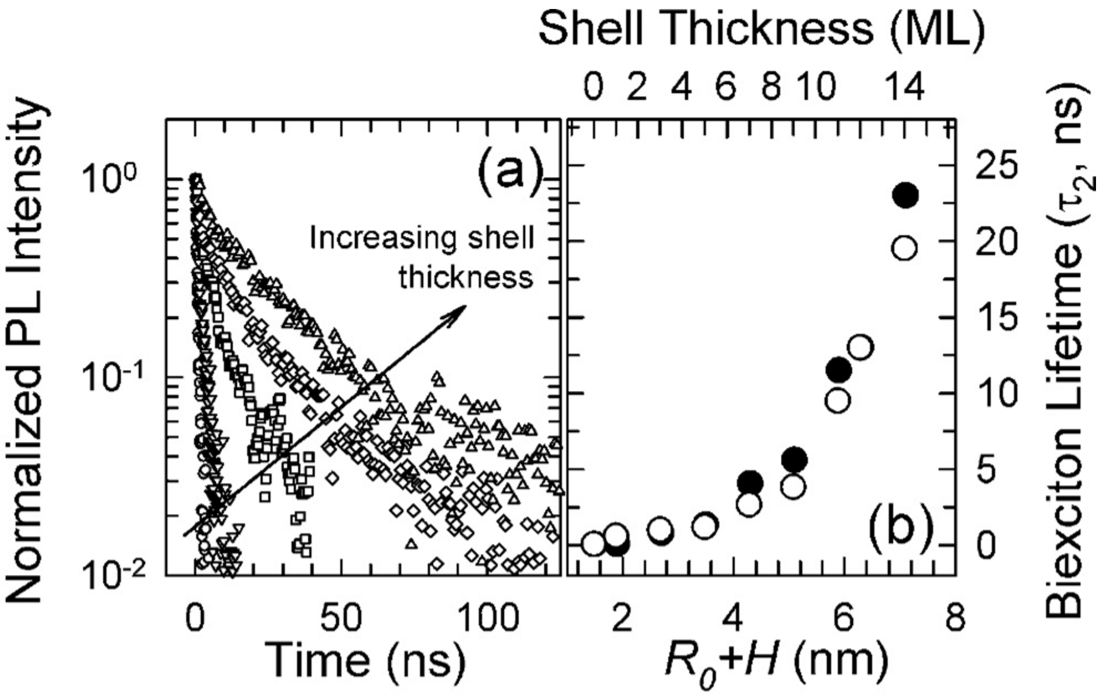

Figure 1.4: Left: Biexciton recombination dynamics of CQDs with increasing shell thickness. Right: Biexciton lifetimes as a function of total CQD radius for two equivalent samples. Reproduced with permission from [18].

dominated by the shell. Overall, there is an increase in the Stokes shift between the PL and absorption spectra and a decrease in the electron-hole wavefunction overlap, illustrated in Figure 1.3a As the CdS shells grew to approximately 9 monolayers thick, a reduction in the AR rate of three orders of magnitude was observed. Figure 1.3b also demonstrates the decreased overlap between the absorbance of the QDs and PL emission with increasing shell thickness. The thickness of the alloyed layer was shown to remain constant as the shell exceeded 9 monolayers yet there was still an increase in the biexciton lifetime, shown in Figure 1.4, which will have been a result of the reduction of the electron-hole wavefunction overlap. These results are direct evidence that an alloyed interface between the core and shell is an important factor in the reduction of AR rates in CQD structures. [18] Synthetic methods have also been developed to control the alloying of the core/shell interface in CdSe/CdS dots. Fast shell growth yielded an abrupt interface and deposition of the alloy layer onto the core before the growth of the rest of the shell resulted in a smooth interface. CQDs with the alloyed structure showed a significant AR rate suppression without impacting the photoluminescence energy and quantum yield. The comparative study between the CQD structures with an abrupt and smooth alloyed interface between the core and shell gives direct empirical evidence of the importance of the interface when developing CQDs capable of lasing. [22]

1.4 Whispering Gallery Mode Resonators

1.4.1 Background

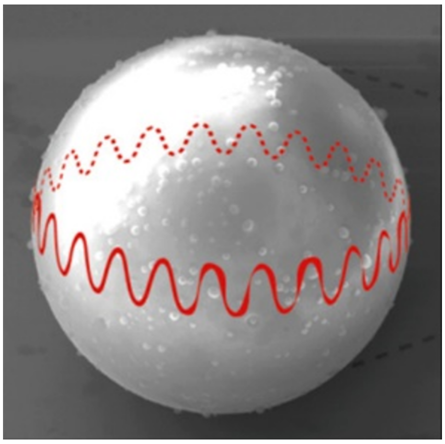

Figure 1.5: Schematic of a spherical WGM resonator displaying the propagation of a wave of light around the equator of the resonator. Reproduced with permission from [23]

The understanding of the principle of whispering gallery modes can be traced back to the beginning of the 20th century and has since been adapted for use in modern optical cavities. WGMs are generated when light at a specific wavelength cycles around a cavity equator via total internal reflection due to the different refractive indices of the cavity and the surrounding environment. [24] The higher the contrast between refractive indices, the smaller the cavity can be without losing confinement. Total internal reflection occurs when a ray of light has an angle of incidence that is larger than the critical angle, defined as $\theta_c = arcsin(\frac{N_s}{N_m})$, where N_m is the refractive index of the cavity and N_s is the refractive index of the surrounding medium. Light that satisfies this condition will propagate around the equator of the cavity, glancing off the surface of the sphere. After one round trip, the light is in phase with itself and forms resonant WGMs. [25] A WGM can be described by its polarisation and mode numbers n, m and l. The polarisation state consists of the transverse electric (TE) and magnetic (TM) modes and the mode numbers n, m and l are integers that describe the number of maxima in the radial, equatorial and polar components of the mode. [25–27] For WGM microresonators, such as the resonators used in this research and that pictured in Figure 1.5, the mode size is very small, as light can cycle millions of times around the edge of the cavity through total internal reflection. Light interacts with the surrounding environment through the evanescent field of WGMs (also called evanescent waves) which decay exponentially from the cavity surface, therefore any change in the environment close to the surface can affect the mode properties and leads to changes in the emission spectrum, such as frequency shifting and linewidth broadening. When the mode size and volume is small, there is a high energy density of the WGM within the cavity due to an inversely proportional relationship between the two properties. A high energy density inside the sphere indicates a strong interaction with the gain medium and is beneficial for producing WGM lasers. [26–28] The resonant wavelength of a WGM resonator is affected by a change to either the cavity radius or the refractive index of the surroundings, and can be described using the following basic approximation. [26, 29, 30]

$$\frac{\Delta\lambda}{\lambda} = \frac{\Delta R}{R} + \frac{\Delta N_s}{N_s} \tag{1.4}$$

Hence to be able to use WGM resonators as sensors, the addition of a target analyte to the cavity must alter the radius or the refractive index of the surrounding environment. Another property of WGM resonators which can indicate their suitability as sensors is the quality factor, or Q factor. Q factor is a measure of the photon storage ability of a microsphere, with a larger Q factor corresponding to a longer photon lifetime in the cavity and a better cavity for optical gain. Q factor can be calculated from the full-width-half-maximum (fwhm) of the resonant peak below lasing threshold and can be estimated using the following equation

$$Q = \frac{\lambda}{\delta\lambda} \tag{1.5}$$

where λ is the centre wavelength of the resonant mode and $\delta\lambda$ is the fwhm of the resonant mode. [28] WGM resonators made of certain materials can have minimal losses when light is reflected around the surface and they can reach very high Q factors of up to 10^{11}, however a Q factor as high as this is not always desirable for sensing applications. [25, 31] WGM microcavities are also promising as lasers due to the low threshold exhibited in the various cavity geometries that have been produced. WGM resonators that contain a gain medium and exhibit lasing are referred to as active WGM resonators. This gain medium can be coated on [32, 33], embedded in [34, 35] or used to create the resonator, [1, 36, 37] with both organic and inorganic gain media widely used. Quantum dots are a popular choice of gain medium due to their wide availability, controllable emission, ease of excitation and the high refractive index of CQDs; the refractive index of CdSe/ZnS QDs that will be used in this research is approximately 1.7–1.8 for a solid-state film of CQDs. [38] Using CQDs as gain media for active WGM lasers means the only requirement for excitation is that the pump wavelength must be shorter than the band gap and threshold fluences as low as 0.5 mJ cm^{-2} have been demonstrated. [39,40] Characteristic behaviour of WGMs in active resonators is the rapid increase in mode intensity, high signal to noise ratios, and Q factors above lasing threshold. [25, 41]

1.4.2 Synthesis and Structure

WGM resonators with a wide range of different geometries have been produced, including microring, microdisk, bubbles, droplets and goblets. Many different materials have been used to create these resonators, with polystyrene and silica microspheres being particularly popular for biological sensing. [28, 39, 42] WGM lasers made from the emulsion-templated self-assembly of CQDs are a relatively new development, with the first example published in 2018. [1] Emulsions have been studied extensively and have been used for a huge range of industrial and household applications for decades. An emulsion is defined as a mixture of two immiscible liquids that often require the presence of an emulsifier to form and stabilise the mixture of liquids. An emulsifier is an ampiphilic molecule, or polymer, that lowers the interfacial tension to create stable emulsions. There are three main types of emulsions that can form: water-in-oil (W/O), oil-in-water (O/W), and complex emulsions such as water-in-oil-in-water (W/O/W) and oil-in-water-in-oil (O/W/O). Most emulsions do not form spontaneously and require an, usually mechanical, energy input to disperse one phase in the other. Formation of an emulsion depends on four main factors; the method of emulsification, temperature, im-

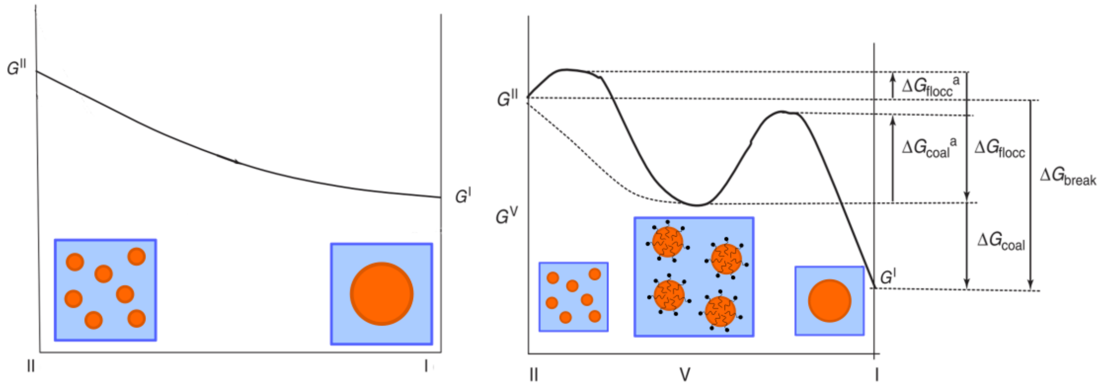

Figure 1.6: Free energy profiles of an emulsion without (left) and with (right) the presence of a surfactant. G^{II} is an emulsified system, G^{I} is two separate phases before mixing and G^{V} is a kinetically stable emulsion, all of which are figuratively represented below the energy profiles. ΔG_{coal} and ΔG_{flocc} is the Gibbs energy of emulsion breakdown through droplet coalescence and flocculation respectively. Adapted from [47].

miscibility of solvents, and presence of surfactants. [43] Surfactants are most often used as an emulsifier as they lower the interfacial tension between the two phases, reducing the energy required to form smaller droplets. [44] In some cases, solid particles can also act as surfactants and arrange themselves at the interface between droplets and the continuous phase to create a Pickering emulsion. [45, 46] Figure 1.6 is a schematic showing the free energy profiles of an emulsion with and without a surfactant and acts as a visual demonstration of the thermodynamic stability the presence of a surfactant brings to an emulsion. On the left, the free energy profile shows that the route to emulsion breakdown, for example through droplet coalescence, without a surfactant is a continuous line demonstrating the natural instability of emulsions. Surfactant molecules, when present, are able to stabilise emulsions through the lowering of interfacial tension because the hydrophobic tails remain in the solvent while the hydrophilic head groups stay in the main phase, shown on the right of Figure 1.6, and an energy barrier is created meaning energy input is required to cause the emulsion to break down. [47] Emulsions are not thermodynamically stable due to the large interfacial area of droplets within a continuous phase, however emulsions can be considered stable if they are resistant to physical processes such as flocculation, sedimentation, and coalescence over a significant length of time. [45] For the production of supraparticle lasers detailed in

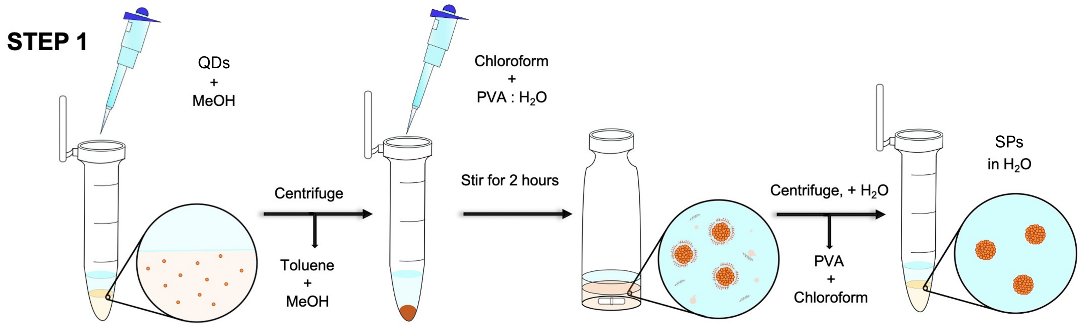

Figure 1.7: The emulsion method used to assemble supraparticles assembled entirely from CQDs.

2018, CQDs are dissolved in an organic solvent that is immiscible in water, such as cyclohexane or chloroform, then emulsified with a solution of water and surfactants, such as sodium dodecyl sulphate (SDS) and poly(vinyl alcohol) (PVA). The emulsion is stirred at a temperature high enough to evaporate the solvent, reducing the droplet size of the oil phase to confine the QDs and forming solid, spherical supraparticles (SPs). SPs in this work refers to micron scale spherical structures consisting entirely of nanometre sized CQDs. For larger supraparticles to grow, the temperature must be such that the evaporation rate of the solvent is slow enough so the concentration increase inside the droplets allows the QDs to assemble in the minimum energy configuration. [1]

Fabrication of self-assembled supraparticles has been studied for at least two decades, however producing self-assembled lasers using this emulsion method was first demonstrated in 2018. [1] As shown in Figure 1.7, the emulsion assembly method begins with CQDs dissolved in chloroform (or any other suitable hydrophobic organic solvent) to create the oil phase which is then dispersed within a solution of poly(vinyl alcohol) (PVA) in water - the water phase. The resulting emulsion is then stirred as the solvent evaporates which forces CQDs within the oil phase closer together until they self-assemble into spherical structures consisting entirely of CQDs referred to as Supraparticles (SPs). The potential of microlasers produced using this emulsion method has also inspired efforts to understand the underlying interactions present within these emulsions to be able to tailor the resulting supraparticles for specific applications. In situ X-ray scattering studies have shed light on the crystallisation mechanism of such SPs. During nucleation and early growth of the supracrystals, CQDs and ligands behave as traditional hard spheres in a liquid phase, then during the latter stages before permanent assembly, there is an instantaneous transition from a liquid to a crystal phase. The crystals are then compressed by the shrinking emulsion droplet as the solvent evaporates and the ligands on the surface of the individual CQDs are pushed close enough together to experience van der Waals attraction which aids in the crystallisation process. [48, 49] Measured interparticle distances in fully assembled SPs indicate that oleate ligands on CQDs slightly interlock during the process, therefore the latter stages of SP assembly is governed by balancing attractive van der Waals forces and steric repulsion between the ligands on the surface of the CQDs. Nucleation of SPs within droplets also occur at much lower volume fractions than predicted using the traditional hard sphere model, which is attributed to the contribution of the attractive van der Waals forces between the ligands to the system. [50, 51]

For the crystal structure of SPs, these studies found that the preferred structure is a majority face-centred cubic crystal structure, however some hexagonal close packed structure was also present at nucleation. This is due to the free energy of these two crystal structures being very similar and both can stabilise the crystal nuclei within the emulsion droplets. [48, 51] Examples of these packing structures are shown in Figure 1.8. The ability to control the structure and properties of SPs produced using this emulsion method is also incredibly desirable, and there is a myriad of different factors that can have an effect on the resulting SPs. The surfactant, solvent choice, drying rate, and emulsion formation and are considered the variables with the most impact on the structure, mechanical and optical stability of SPs. [52, 53] Droplet formation has been achieved using many different methods, such as stirring, placing single droplets on a supderhy-

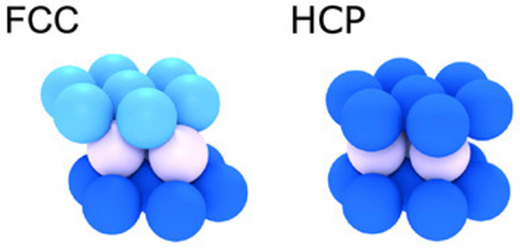

Figure 1.8: Illustration of face centred cubic and hexagonal close packing crystal structures of CQDs within supracrystals. Reproduced with permission from [48].

drophobic surface, spray drying, and, possibly the most popular method, microfluidics. It is also possible to design the self-assembly of nanoparticles to occur spontaneously by controlling the different interactions between the nanoparticles and the surrounding environment. [54] Surfactant choice is important, as it impacts the interfacial tension between droplets and the continuous phase, which can in turn alter the pressure with the emulsion droplets as described by the LaPlace pressure equation $\Delta p_L = 2\gamma/r$ where γ is the interfacial tension of the droplet and r is the droplet radius. Altering the pressure within emulsion droplets affects the attractive forces between the nanoparticles contained within, resulting in surfactant-dependent SP structures. [55, 56] One such example is the ability to control the formation of crystalline ordered, core/shell and Janus SPs by altering the length of hydrophilic tails in the surfactants used to affect the interfacial tension and from that alter the LaPlace pressure within the emulsion droplet and affect the attractive forces between the NPs. [55] Lowering the interfacial tension by increasing the surfactant concentration was found to increase the crystallinity and size of CQD SPs, however this was not found to alter the crystal structure of the SPs. This was attributed to an emulsion with a lower interfacial tension between the two phases producing a more flexible interface which can accommodate growing crystals, resulting in the larger and higher quality crystals observed. [48, 51, 56] Using multiple surfactants can also produce high control over the results of the emulsion assembly. Using ionic surfactants produced smaller SPs as the electrostatic repulsion between the surfactant head groups results in the molecules being able to pack over a tighter curvature producing smaller droplets and therefore smaller SPs. This phenomenon is called the hydrophilic-lipophilic balance (HLB) balance where higher electrostatic repulsion between head groups means the surfactant has a higher HLB. High ratios of ionic surfactants paired with a nonionic hydrophobic surfactant produced porous SP structures as this combination was able to stabilise W/O/W emulsions. These are illustrated in Fig. 1.9, along with the effects of the stirring speed, or shear rate, during emulsion formation. [57] Overall, blending these surfactants introduces electrostatic and steric barriers to droplet coalescence and emulsion breakdown which in turn leads to improved SP homogeneity. [56, 57] Using no surfactant has also been demonstrated,

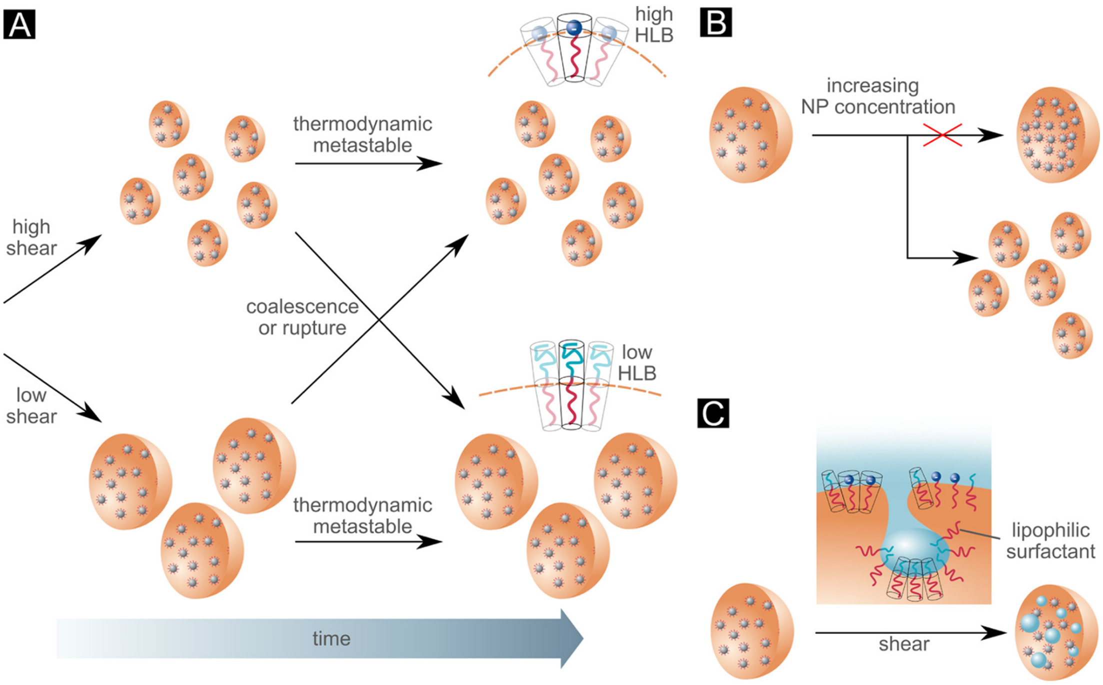

Figure 1.9: Illustration of the effect that shear rate (A), CQD concentration (B), and surfactant ratios (C) has on the structure of SPs produced using the emulsion method. Reproduced from [57] with permission.

with emulsion formation possible by tailoring the solvent choices for both the oil and water phase. The main example within literature used DMF for the water phase, and hexane for the oil phase. In this case, resulting SPs had a Wurzite hexagonal close packed crystal structure. [58,59] Evaporation rate is one of the main factors to control during emulsion self-assembly, which can be achieved through temperature moderation or choosing solvents with a desirable boiling point. Controlling the evaporation also sets the rate of change of volume fraction of CQDs within emulsion droplets which is important for controlling crystallisation of SPs. Decreasing the rate of change of volume fraction increases the ability of CQDs to rearrange and find the minimum energy structure, allowing for more ordered and higher quality SP crystals. [48,51] Temperature and solvent choice affects SP assembly because van der Waals forces which, as established earlier, play a significant role in the crystallisation process are temperature dependent and also affected by the ligand-solvent interactions within the emulsion. [60] Using a solvent with a high boiling point to reduce the evaporation rate which allows CQDs more time to be able to arrange into the lowest energy configuration produces ordered and highly crystalline SPs. In addition, a solvent with a lower interfacial tension compared to water, such as chloroform, can mimic the effects of increased surfactant concentration and produces favourable SPs. [51] Low boiling point solvents, and therefore a higher evaporation rate, have been found to produce the smallest and lowest quality SPs, even though the mechanism of crystallisation was found to remain the same. [48, 51] On the other hand, other studies have concluded that a higher temperature, and therefore an increased evaporation rate, can produce more ordered SPs as the increased thermal energy allows CQDs to move more and also increases the van der Waals attraction between the ligands on the surface of the CQDs. This compensates for the loss of configurational entropy that occurs when producing ordered fcc crystal structures. [61] Finally, polydispersity of the CQDs has also been found to affect the structure of assembled SPs, with polydispersity as low as 15% beginning to introduce unfavourable amorphous structures into SPs. These differing conclusions demonstrate the difficulty in understanding the complex interrelation between different physiochemical effects that alter the structure and properties of the produced SPs.

Spherical CdSe/CdS CQD SPs recently demonstrated WGM lasing, shown in Figure 1.10. [1] WGMs had previously been observed in SPs [36], however lasing from microspheres made purely of CQDs had not been demonstrated until this publication. The SPs in this work were synthesised using the emulsion technique described earlier and final microspheres had average diameters of 10.2 µm. Figure 1.10a demonstrates typical photoluminescence (PL) emission spectra for a WGM laser taken at different pump laser fluences, with the spectra in red and orange showing the laser operating above threshold and the spectra in blue and green showing the laser operating below threshold. Below threshold, the general PL emission is broad and has a low intensity, whereas above threshold three sharp and intense modes appear, which indicates lasing. WGM peaks were exhibited in the microspheres made possible due to the high refractive indices of QDs relative to air. To estimate the pump fluence at which these WGM lasers begin operating in the laser regime, the average emission peak area is plotted against the pump fluence to get the laser transfer function, shown in Figure

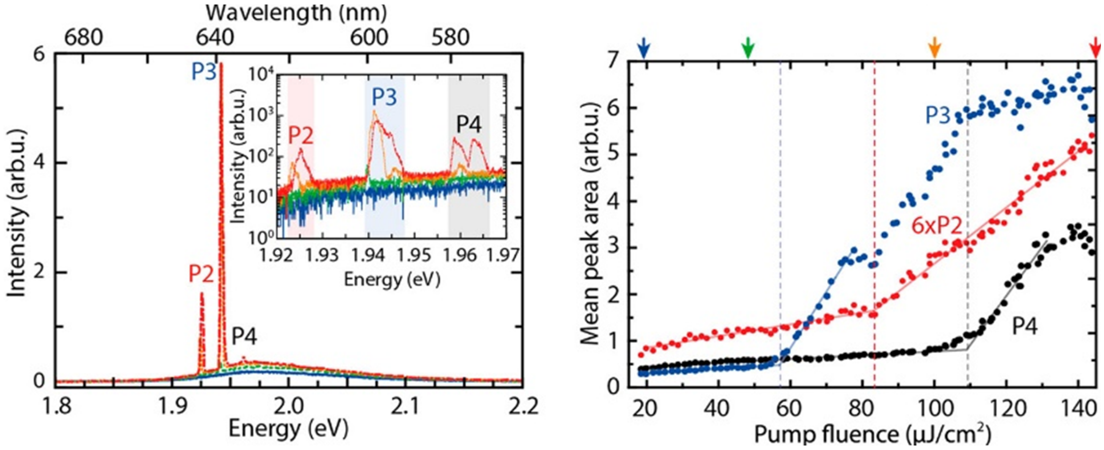

Figure 1.10: Left: Emission from a single SP at different pump fluences with picosecond scale pulse duration: 18 µJ cm^{-2}(blue), 48 µJ cm^{-2} (green), 100 µJ cm^{-2}(orange) and 145 µJ cm^{-2} (red) at low spectral resolution. Left inset: High spectral resolution spectra which shows the substructure of the lasing peaks. Right: Analysis of the peak areas of the lasing peaks to determine lasing thresholds. The coloured arrows correspond to the pump fluences the spectra in (left) were taken at. Reproduced with permission from [1]

1.10b. There are two clear regions of differing gradients below and above threshold which can be fit to straight lines, the intersection of which is the estimate for the laser threshold of the WGM laser. Lasing was observed at a low threshold of 58 µJ cm^{-2} (340 fs pulses) and the SPs were shown to maintain their properties without stability of degradation issues over weeks of experiments. Lasing from the shell was also observed in SPs consisting of thick shell CdSe/ZnS QDs along with multimode lasing from SPs with two more modes observed when pumped at fluences of 83 µJ cm^{-2} and 110 µJ cm^{-2}. Different coloured lasing from the shell and the core of thick shell QDs has also been demonstrated with the ability to switch between colours also exhibited, albeit using a different microring cavity geometry. [62]

More recently, this knowledge of emulsions has been used in nanotechnology to produce microscopic three-dimensional assemblies of a wide variety of different nanoparticles, polymers, and proteins. For example, the emulsion method can be used with many different materials such as polystyrene [63–66], proteins such as BSA, pectin and cellulose [67], latex [68], gold nanoparticles [55,69], PMMA [70], and silica. [71] On top of these materials, emulsion self-assembly has been used with many different types of

CQD, however not all of the microspheres have been able to act as lasers. [50, 60, 72] Self-assembled microsphere lasers consisting of blends of different colours of CQDs has since been demonstrated. Green and red CQD blends have been used to improve the quality factor and red laser emission intensity. This is due to the reduced density of red CQDs due to the presence of the green CQDs and these could also act as donors for the red CQDs to contribute to the improves optical properties. [73] Blends of red and yellow CQDs have also been used to produce microspheres lasers which could lase in the red and yellow regimes both separately and simultaneously to produce orange lasing. [40] Blending red, green and blue CQDs together has also been demonstrated to reduce inter-CQD energy transfer losses and enhance the emission intensity [74], and to produce white light emission [23, 59] that could be used to improve the colours of backlight liquid crystal displays. [58] The emulsion method has also been adapted to produce CQD microspheres in-situ with silica precursors to produce SPs embedded within a silica matrix. Such lasers achieved lasing with Q factors of up to 3500 which were also stable to continuous pumping for up to 40 minutes. [37]

1.4.3 Applications in Biosensing

Biosensing is an increasingly important area of research as we try to improve on the speed and accuracy of diagnoses for a wide range of diseases, such as cardiovascular diseases and cancer. In particlar, the COVID-19 pandemic demonstrates the demand for highly sensitive and rapid benchtop sensing to be able to track and control the spread of the disease. Thrombin is an anticoagulant protein which is a popular target in the treatment and detection of cardiovascular diseases and blood clots. [75–77] Quantum dots and Whispering Gallery Mode resonators have been studied for around two decades for their biosensing capabilities [78–80], and biosensing has yet to be demonstrated for CQD supraparticle lasers. Basic requirements for biosensors include the detection time, high sensitivity, high specificity and selectivity, and high signal to noise ratio. [25] WGM lasers can meet all of the above criteria favourably: quick signal response allows for real-time analyte detection, are highly sensitive due to the evanescent field at the cavity surface [26], can be made highly selective with suitable surface functionalisation, and finally high signal to noise ratios can be achieved using WGM lasers operating above threshold. [25] WGM lasers are often spherical or ring cavities made of high refractive index material that can ‘capture’ and contain light which then propagates along the equator of the cavity through total internal reflection and have been studied for decades. [24] After light cycles around the cavity, it undergoes constructive interference with itself and creates resonant modes that extend outside of the cavity as an evanescent field decaying exponentially from the cavity surface. [26,28] Molecules binding to the surface of a WGM resonator are polarised by the evanescent field which can alter the local refractive index and increase the effective cavity diameter, resulting in alterations to the resonant modes observed as wavelength shifting, intensity changes, and line broadening. [26, 27, 34] Therefore, consideration must be given to the surface functionalisation of the biosensor because the target analyte must be within the penetration depth of the evanescent field for the molecule to be polarised and induce the wavelength shift. [81] The observed shift in wavelength also depends on the number of molecules within the field and their polarisability. The sensitivity of this evanescent field makes WGM resonators incredibly promising for biosensing applications [26], however the short tail of the evanescent field also hinders the ability to achieve the optimum sensitivity WGM biosensors are capable of. [82] WGM lasers are an even better option for sensing due to the increased signal to noise ratio and faster response to analyte binding when operating above threshold in the lasing regime. [27,31]

There are several cavity properties that can be altered to improve the sensitivity and limit of detection (LoD) of WGM sensors. [28, 83] The limit of detection is defined as the lowest concentration of target analyte a sensor can reliably detect. [24,84] Here, the main factors which will be discussed are the cavity diameter and the Quality factor, which are both linked. The quality factor, or Q factor, describes the lifetime of a photon travelling around the cavity, or the ability of the cavity to store light, and has a significant impact on the threshold of WGM lasers. [26,27,31,41,85] Q factors are mainly limited by scattering from surface defects, contamination, radiative losses, and material absorption. [25, 28] The diameter of WGM resonators can also have a profound impact on its optical properties, namely by smaller diameter microcavities having an extended evanescent field for a given mode outside of the cavity and therefore an increased evanescent field intensity near the cavity surface. This both increases the sensitivity of a WGM biosensor and increases the losses from the cavity, resulting in an inevitable trade-off between cavity quality and sensitivity. [27, 81, 86, 87] However, because the WGM lasers used in this work are on the micron scale with diameters between 3 and 20 microns, this trade off means that it is not necessary to have unachievably high Q cavities to be able to demonstrate biosensing. Lower Q factors also provide the added benefit of producing fewer lasing modes, making wavelength shifts easier to track even though the modes that do lase have higher thresholds. [31] Finally, particularly when discussing microfluidic sensors which require samples to be pumped through channels containing WGM sensors, the sensing efficiency could also be controlled by altering the rate at which a sample is pumped through the channels, called the sample flow rate. [82] One of the most common detection mechanisms is tracking the shift in lasing wavelength over time as target analytes bind to the functionalised cavity surface. This is normally observed as a redshift [88–91] as the effective cavity radius is increased by the layer of analyte molecules on the cavity surface which increases the wavelength of the resonant mode, shown in Figure 1.11. [81,85] In addition to this, the layer of analyte increases the

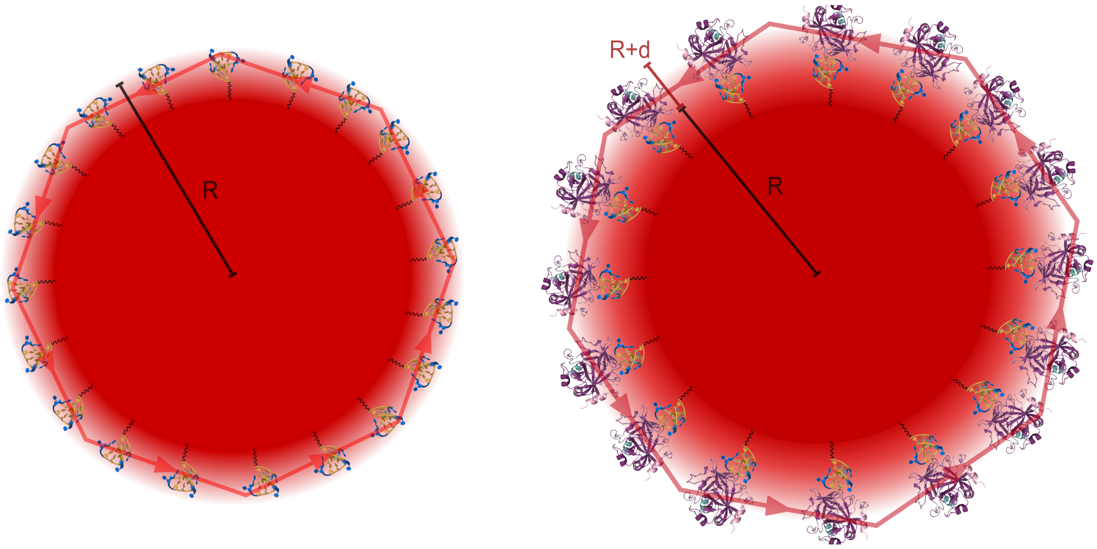

Figure 1.11: Left: SP laser with DNA aptamer TBA-15 coated onto the surface. Right: TBA-SP after Thrombin addition which increases the diameter of the SP and the effective refractive index of the mode, resulting in an observed redshift.

effective refractive index (n_{eff}) of the mode in turn increasing the optical path length, which can be approximated using $n_{eff}2\pi R$, and contributing to the observed redshift. The magnitude of the wavelength shift observed for WGM sensors has also been found to inversely proportional to the cavity radius and the surface density of the analyte bound to the cavity surface, which of course is linked to the coverage of the detection molecules attached to the surface. [26, 92] Within literature, many of the wavelength shifts seen with WGM biosensors are often on the order of picometers requiring complex light coupling and a high resolution spectrometer to observe. [91, 93, 94]

Using WGM lasers for sensing is often favoured over fluorescent sensors due to the increased signal-to-noise ratio when operating in the stimulated emission regime. [27, 31, 83] Francois & Himmelhaus produced Nile red doped polystyrene microspheres and reported an eightfold increase in signal-to-noise ratio above threshold. These microspheres had a diameter of 15 µm and were fixed to a glass substrate with polyelectrolyte then subsequently attached to a PDMS microfluidic cell to be used for the detection of bovine serum albumin (BSA) in PBS buffer. This study also found that the speed of data acquisition and the detection limit also improved dramatically above the stimulated emission threshold. [31, 95] Developing label-free WGM laser biosensors does come with issues due to non-specific binding of molecules to the laser surface meaning false positives can be an issue when testing complex biological samples. Reynolds *et. al.* tackled this issue by using two Nile red doped polystyrene microspheres with differing surface chemistry and emission wavelengths. The reference resonator detected the signal contribution from non-specific binding and environmental fluctuations while the sensing resonator, functionalised with biotin, sensed the presence of Neutravidin in undiluted human serum. [96] Silica WGM microspheres have been used as part of a fibre ring laser cavity for Thrombin detection by using dithiol modified Thrombin binding aptamer (TBA-15). First, the silica spheres were modified with thiol groups to allow the aptamers to bind to the microsphere using a $Na_2CO_3/NaHCO_3$ coupling buffer. Binding of Thrombin was detected through wavelength shifts and broadening of the resonant peak, which could be plotted against each other. Specificity was demonstrated by testing the spheres in a solution of BSA and testing bare microspheres in a solution of Thrombin. These data demonstrated the high specificity of the sensors, showing that aptamer functionalised WGM microspheres can be effective for sensing. However, these WGM microspheres were used as part of a laser cavity rather than as single solid-state lasers. [93] A similar method of using an aptamer functionalised WGM microsphere laser within a single closed cavity containing sample solution has also been used to detect mercury ions down to 50 nM concentrations through an aptamer displacement mechanism at the microsphere surface. [97] To further enhance the limits of detection for WGM microlasers, gold nanorods have been attached to the surface of WGM microlasers to create optoplasmonic sensors capable of being able to detect and measure enzyme reaction kinetics and single molecules. [98] For example, Yu *et. al.* demonstrated single DNA strand sensing in solution by attaching a single gold nanorod on the interior wall of a WGM microbubble cavity. The WGM microbubble laser also formed part of the microfluidic setup with samples as small as 10 pL passed through the optoplasmonic cavity itself and the sensor could detect single DNA molecules within 80 seconds. [82]

Microfluidic chips with WGM laser biosensors integrated have also begun to be trialled with a few different approaches to chip design. Guan *et. al.* used a quartz micropillar array to trap the dye-doped polystyrene microspheres onto the surface of the chip. The PS microspheres were functionalised with antibodies for Influenza A and were also incubated with a blocking reagent to stop non-specific binding to the sensor surface. The sensing chip was left open to allow sample to flow through the micropillars with an evaporation driven process and further modification of the chip surface to alter the sample flow pattern was able to improve the sensing performance. Overall, this setup demonstrated high specificity and could detect Flu A at µg/L concentrations in a 3 µL sample within 15 minutes. [100] A slightly different chip design was used by Alvarez Freile *et. al.* using dye doped polystyrene microspheres. A chip containing six closed channels was used, with each channel containing 1000 16 x 12 µm wells, each containing one laser microsphere functionalised to sense for Epithelial Growth Factor Receptor (EGFR). Wavelength shifts were detected with analyte concentrations as low as 0.5 nM within 20 minutes. [101] Figure 1.12 shows another microfluidic chip design

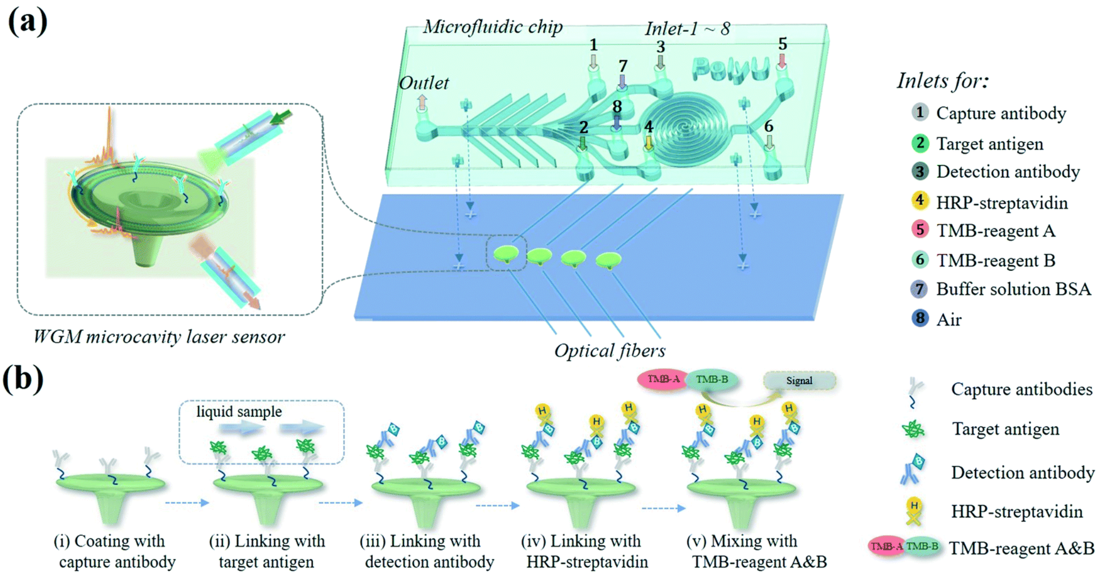

Figure 1.12: (a) Schematic of the microfluidic chip design used in the study carried out by Ouyang *et. al.*. The chip contains the WGM microdisk lasers on a substrate with optical fibres embedded within to collect the signal. The PDMS microlfuidic chip contained a spiral mixer to mix two of the reagents and eight different inlets for injecting reagents for surface functionalisation and cleaning of the microdisks, the sensing solution, and an outlet for the solutions to be collected. (b) The reaction scheme for the surface functionalisation carried out in-situ to prepare the microdisk lasers for ELISA. Reproduced with permission from [99]

used by Ouyang *et. al.* with multiple inlets to be able to carry out in-situ surface functionalisation of the WGM microdisk lasers and subsequent biosensing experiments all on the same chip. The microdisk lasers were fabricated using 3D µ-printed resin and coated with Rhodamine 6G dye. Using a popular biochemical sensing method, enzyme-linked immunosorbent assay (ELISA), on-chip sensing of the popular biomarker vascular endothelial growth factor (VEGF) was achieved with a limit of detection of 17.8 fg/mL which is an order of magnitude more sensitive than current commercial ELISA kits. This was achieved with a pump laser energy of 44.83 nJ/mm^2 at 532 nm with a pulse duration of 10 ns and a 10 Hz repetition rate, demonstrating the huge scope of this technology for early disease diagnosis using cheap and simple fabrication methods. Sensing of VEGF was detected through a reduction in the WGM laser signal intensity as the concentration of VEGF in solution increased, a slightly different method to the wavelength shift detection methods used in the previous two studies mentioned. [99] Cognetti *et. al.* were able to go further with these microfluidic sensor designs and were able to fabricate a tissue chip with integrated antibody-functionalised ring resonators. They were able to incubate small human cell cultures on top of the chip and use the ring resonators to sense for specific cell secretions in real time. [102] Wang *et. al.* were able to use self-propelled liquid crystal (LC) WGM microlasers functionalised with antibodies to sense for specific protein exosome biomarkers within a simple three channel microfluidic chip. Self-propelled motion of the microlasers was induced through using surfactants above the critical micelle concentration which produces a surface energy gradient at the LC surface, producing internal convection within the droplet, which then produces motion through the Marangoni effect. The method required pre-treatment of samples to label the target analytes with Nile red (NR) dye, as the detection mechanism was based on the NR labelled biomarkers binding to the surface of the microlasers and, due to the spectral overlap of the microlaser emission and the absorption of the NR dye, as more of the target analyte bound to the laser surface, red laser emission was detected with the emission intensity proportional to the number of NR-labelled target analytes bound to the laser surface. Detection of protein biomarkers associated with cancerous tumour cells within complex media was achieved with a sensitivity of approximately 1.1×10^4 particles/µL. [103] Suo *et. al.* fabricated aptamer functionalised polystyrene microsphere lasers which could discriminate between exosomes secreted from different cells to aid with cancer diagnosis. This group were also able to study these microlaser probes on the blood plasma of four breast cancer patients and were able to estimate the number of cancer exosomes present in the blood of the patient. To further enhance the study, five different aptamer functionalised microspheres were used to screen for multiple proteins present on the surface of exosomes secreted by tumour cells. Using this method, the blood from the breast cancer patients could be distinguished from a healthy sample, and due to being able to measure the ratio of the different biomarkers present on the surface of the exosomes within the plasma samples, the type of tumour present could even be speculated. [104]

Using spheres fabricated from biologically incompatible materials has not been a barrier to achieving WGM lasing inside cells for cell tagging and tracking experiments.

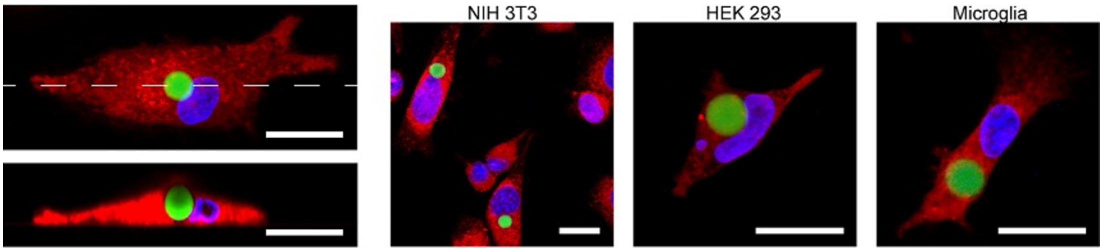

Figure 1.13: Confocal laser scanning microscopy images of the cell types tested where red is the cytoplasm, blue is the nucleus and green is the microsphere. Left: A macrophage where the top is the maximum intensity projection and bottom is the cross section along the dashed line. Right: Maximum intensity projection images for the three other cell types tested: NIH 3T3 fibroblasts, Human Embryonic Kidney 293 and primary mouse microglia. Scale bars are 20 µm. Reproduced with permission from [105]

Schubert *et. al.* demonstrated intracellular lasing using polystyrene divinylbenzene (PS-DVB) microspheres doped with Firefli Green fluorescent dye. These spheres were able to act as WGM lasers because the refractive index of PS-DVB is 1.60 compared to the refractive index inside of a cell which is approximately 1.375. Microspheres were found to be internalised by all four of the cell types tested, even cells which do not have a particular capacity for endocytosis. Confocal laser scanning microscopy showed the microlasers were fully contained within cells, as can be seen in Figure 1.13. One of the smaller microlasers measured had a diameter of 13 µm, a lasing threshold of 5 nJ cm^{-2} and a Q factor calculated to be near 10,000 even below threshold. Optical pumping was carried out using a pump source with a 10 Hz repetition rate and a pulse duration of 5 ns. Cells were found to remain viable and mobile over the course of the 19-hour experiment with damage only being visible after several thousand continuous pump pulses well above threshold energy. The study also experimented using different microlasers within different cells for cell tracking and found that the dominant lasing wavelength and the difference between the two visible TE peaks could be used to identify and track specific cells as these characteristics were unique to each different laser. [105] Fikouras *et. al.* realised non-obstructive intracellular microdisk lasers using GaInP/AlGaInP quantum wells. The AlGaInP microdisk resonators had a very high refractive index of 3.6 which allowed lasing to be achieved in resonators with diameters as small as 750 nm. Lasing was demonstrated using a 473 nm wavelength pump source with 1.5 ns pulse duations and threshold was measured to be 30 µJ cm^{-2} with Q factors of approximately 3000. These lasers were also found to be internalised by a range of cell types with high uptake efficiencies even in very small cells such as T cells. [106]

Other biosensing methods using CQDs and WGM resonators have been widely studied within the literature, as shown below in Table 1.1. For CQDs, these are often used alongside gold NPs and fluorescent dyes for FRET sensing which relied on fluorescence quenching as the target analytes binds to the surface of QDs, replacing and releasing the dye molecules into solution. This sensing mechanism has been used for a myriad of different biomoleulces with a range of different surface functionalisation schemes. [39, 107–114] CQDs are also very popular for electrochemiluminescence biosensors. [115–119] Gold nanorods can also be attached to the surface of a WGM laser to enable plasmonic sensing. [98] Using WGM cavities for biosensing often requires coating in fluorescent dyes, polymers or proteins. [31, 87, 94, 96] For example, Humar et. al. used glass beads coated in fluorescent protein to monitor cell division by tracking wavelength shifts from the changing refractive index of the surrounding medium. [86] Biotin, aptamer, and antibody coated WGM biosensors for specific sensing have also been demonstrated using different materials too. [90,91,96,120,121] On-chip sensing has already been achieved with WGM microlasers integrated onto optofluidic sensing chips. [99,122] In the study conducted by Ouyang et. al., the chip was designed to make it possible to integrate multiple WGM lasers to achieve multiplexed sensing. These demonstrations show the effectiveness and promise CQDs and WGM lasers have for biosensing, hence it makes sense to combine the two to trial biosensing with CQD SP lasers.

Table 1.1: A summary of the different types of biosensors in literature referenced in Section 1.4.3. PS = Polystyrene, TBA = Thrombin Binding Aptamer, PBS = Phosphate-buffered Saline, and PS-DVB = Polystyrene Divinyl Benzene, EGFR = Endothelial Growth Factor Receptor, VEGF = Vascular Endothelial Growth Factor, FBS = Fetal Bovine Serum, 5CB LC = 4'-Phenyl-4-biphenylcarbonitrile Liquid Crystal, PEG = Polyethylene glycol, ECL = Electrochemiluminescence.

Target Analyte	Recognition Element	Sample Matrix	Limit of Detection	Gain Medium	Sensor Material	Detection Method	Ref.
Thrombin	TBA	DI Water	1 µg/mL	n/a	Silica glass	Wavelength shift	[80]
Streptavidin	Biotin	Citrate buffer	1 aM	n/a	Silica microbubble	Wavelength shift	[82]
BSA	n/a	PBS	n.d.a.	Nile red	PS	Wavelength shift	[31]
MS2 virus	Antibody	PBS	0.2 ng/cm^2	n/a	Silica glass	Wavelength shift	[83]
Neutravidin	Biotin	Serum	~25 nM	Nile red	PS	Wavelength shift	[96]
Thrombin	TBA	Serum	~0.3 mg/mL	n/a	Silica glass	Frequency shift	[90]
Lysozyme protein	n/a	PBS/air	0.38 ng	Firefli Fluorescent Red dye	PS-DVB	Wavelength shift	[95]
Hg^{2+} ions	cDNA	Tris-$MgCl_2$ buffer	~5 nM	n/a	Silica glass	Wavelength shift	[97]
Influenza A	Antibody	PBS	20 µg/mL	Nile red	PS	Wavelength shift	[100]
EGFR	Protein G	PBS	0.5 nM	Coumarin 6	PS	Wavelength shift	[101]

Continued on next page

Table 1.1: A summary of the different types of biosensors in literature referenced in Section 1.4.3. PS = Polystyrene, TBA = Thrombin Binding Aptamer, PBS = Phosphate-buffered Saline, and PS-DVB = Polystyrene Divinyl Benzene, EGFR = Endothelial Growth Factor Receptor, VEGF = Vascular Endothelial Growth Factor, FBS = Fetal Bovine Serum, 5CB LC = 4'-Phenyl-4-biphenylcarbonitrile Liquid Crystal, PEG = Polyethylene glycol, ECL = Electrochemiluminescence.

Target Analyte	Recognition Element	Sample Matrix	Limit of Detection	Gain Medium	Sensor Material	Detection Method	Ref.
VEGF	Antibody	PBS	17.8 fg/mL	Rh6G	SU-8 resin	Laser peak intensity	[99]
C-reactive protein	Antibody	Serum	3.1 ng/mL	n/a	Silica nitride	Wavelength shift	[102]
Exosomes	Antibody	FBS	1.1 $\times 10^4$ particles/µL	Coumarin 6 /Nile red	5CB LC	Wavelength shift	[103]
Exosomes	MUC1 Aptamer	PBS	40 particles /resonator	Nile red	PS	Wavelength shift	[104]
Adenosine /Cocaine	Aptamer	Tris acetate buffer	50 µM /120 µM	n/a	QDs/AuNPs	Fluorescence Intensity	[107]
Thrombin	TBA	PBS	∼10 nM	n/a	QDs	FRET	[108]
Thrombin	TBA	Buffer	∼ 1 µM	n/a	QDs	FRET	[109]
Methamphetamine	Antibody	PBS	6 µg/L	n/a	CdS QDs	FRET	[112]
Thrombin	TBA	Tris-HCl buffer	0.38 nmol/L	n/a	CdS QDs /AuNPs	FRET	[113]

Continued on next page

Table 1.1: A summary of the different types of biosensors in literature referenced in Section 1.4.3. PS = Polystyrene, TBA = Thrombin Binding Aptamer, PBS = Phosphate-buffered Saline, and PS-DVB = Polystyrene Divinyl Benzene, EGFR = Endothelial Growth Factor Receptor, VEGF = Vascular Endothelial Growth Factor, FBS = Fetal Bovine Serum, 5CB LC = 4'-Phenyl-4-biphenylcarbonitrile Liquid Crystal, PEG = Polyethylene glycol, ECL = Electrochemiluminescence.

Target Analyte	Recognition Element	Sample Matrix	Limit of Detection	Gain Medium	Sensor Material	Detection Method	Ref.
Thrombin	TBA	diluted serum	1 nM	n/a	QDs	FRET	[114]
Thrombin	TBA	PBS	3.8 pM	n/a	nanoporous PEG	FRET	[77]
Thrombin	TBA	TAE buffer	1 nM	n/a	PbS QDs	PL quenching	[79]
Thrombin	TBA	PBS	~3 µg/mL	n/a	CdSe QDs /ITO electrode	ECL	[115]
Thrombin	TBA	PBS	2.72 nM	n/a	CdSe/ZnS CQDs /Au electrode	ECL	[116]
ATP/ cocaine	Aptamer	Buffer	30 nM /50 nM	n/a	CdS PbS CQDs /Au electrode	ECL	[119]

1.5 Surface Functionalisation of CQDs

Surface functionalisation is imperative for being able to utilise CQDs and SPs for biological applications. This is because CQDs on their own are often cytotoxic which is generally attributed to the release of heavy metal ions used in QDs, such as Cd and Se, into the surrounding environment. Therefore, if CQDs are used *in vivo*, this leaching can alter the morphological and biochemical properties of cells, leading to loss of functionality, chromosome damage and eventually cell death. [123] Cytotoxicity can be mitigated by using CQDs that have ligand shells and even just by coating QDs in an inorganic shell, such as ZnS. [124] Tailoring CQD structure, composition, and surface can further reduce cytotoxicity, and some meta-analyses of literature studies have indicated that toxicity is closely linked to the surface chemistry of CQDs. [118,125] Surface functionalisation can also be used to tailor the optoelectronic properties of CQDs, as even a single molecule binding to the CQD surface can cause distinct changes to the electronic structure. [118, 126, 127] The reason why ligands can have such a large effect on these properties of CQDs is due to surface trap states that exist in the electronic structure of CQDs. These states arise from 'dangling' bonds at free surface atoms in the QD crystal which creates energy states within the band gap that quench luminescence due to non-radiative combination. As ligands bind to these surface atoms, the energies of these states are shifted outside of the band gap and reduces this quenching effect. [128,129] Ligand length and denticity have been shown to impact the quantum yield (QY) and PL quenching in QDs. [130,131] On top of these optoelectronic benefits, ligand exchange can also be carried out to make CQDs water-soluble and to introduce moieties that can be used for further functionalisation. [132,133] For colloidal synthesis of CQDs, long bulky hydrophobic ligands are required to aid dispersion in organic solvents and stability in solution. [134] For this work, the hydrophobicity of CQDs is necessary for the emulsion technique as CQDs need to be soluble in organic solvents which are immiscible in water. However, for biological applications, the SPs produced need to be water soluble for both post-fabrication surface functionalisation and biosensing tests.

1.5.1 Ligand Exchange

Surface functionalisation is often a process requiring several steps, starting with obtaining the required functional groups that can then be used in further reactions to generate specific surface functionality for the desired application. [137] As a result of colloidal synthesis, CQDs have a shell of ligands bound to their surface which affects the solubility of the crystals, along with other physical and optical properties. Often, these ligands are hydrophobic organic molecules, such as oleic acid or oleylamine, therefore they need to be replaced with hydrophilic molecules suitable for use within biological matrices along with functional groups that are able to undergo further reactions for suitable surface functionalisation. Use of bulky ligands that cannot pack as efficiently, such as oleic acid, have been shown to improve the colloidal stability of CQDs as the space between ligand chains allows solvents to intercalate between them. This is also the case with smaller ligands, such as 3'-mercaptopropionic acid (MPA). [126, 128] The space between ligands may also result in the attachment of small, common ligands like

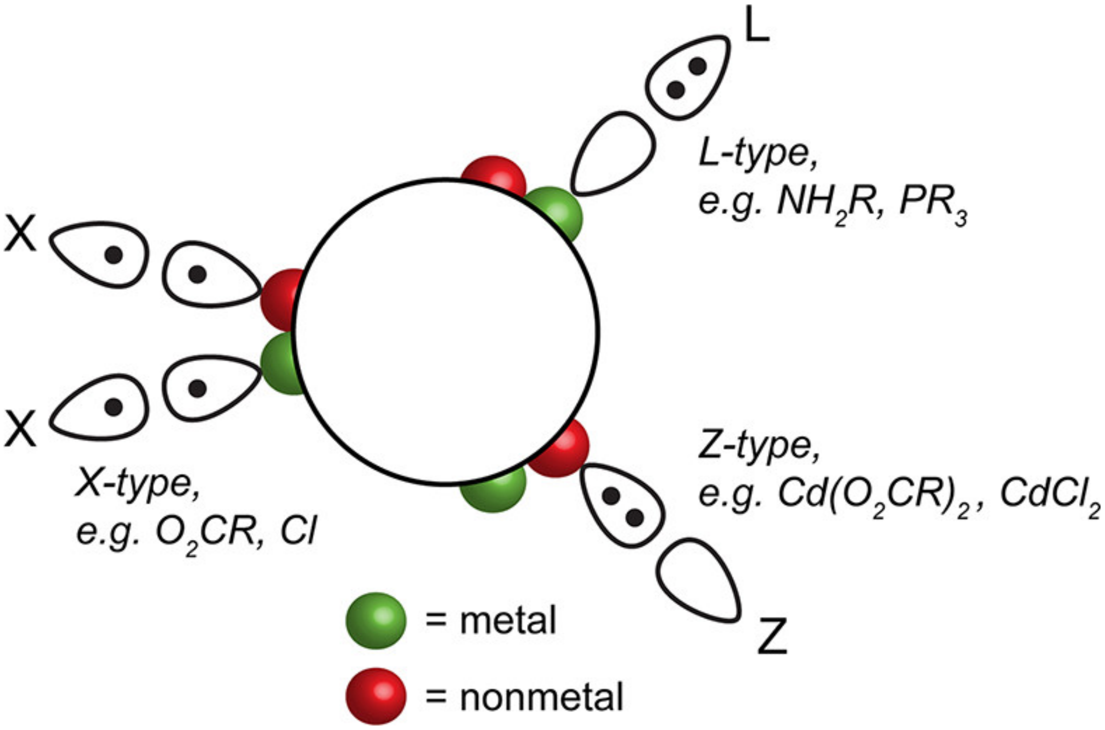

Figure 1.14: Schematic demonstrating the three different types of ligand coordination to CQD surfaces. Reproduced from [135] with permission

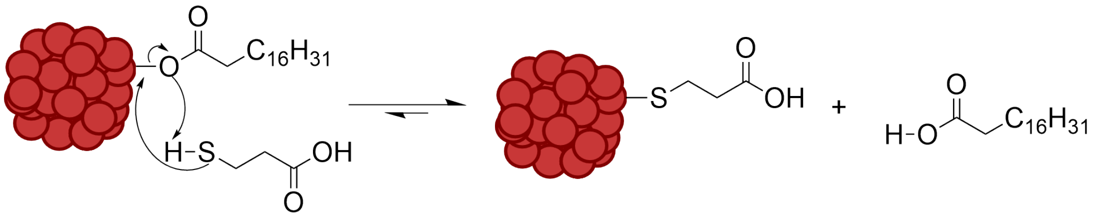

Figure 1.15: Reaction mechanism for ligand exchange of oleic acid with MPA at the surface of CQDs within SPs. Adapted from [136]

OH^- and Cl^- to passivate the remaining free metal ions at the CQD surface which could aid solubility. [128] Direct ligand exchange where the new hydrophilic ligands have a higher affinity for the CQD surface and can replace the hydrophobic ligands is a popular surface modification method for CQDs. Ligand exchange on the surface of CQDs has been widely studied over the last two decades due to the importance the ligand shell has on CQD properties and for biological applications. Some comparisons have been made with self-assembled monolayers (SAMs) on gold films to aid understanding of the ligand system on CQDs which, while a good place to start, does not paint the full picture. For example, CQDs have a large, spherical surface allowing ligands more space to pack, resulting in higher ligand densities compared to SAMs. [128] For surface ligand exchange to occur, a large excess of the replacement ligand is required. Ligands can be categorised into three different types characterised by the number of electrons donated by the binding group of the ligand to the CQD, as shown in Fig 1.14. [135,138] Popular functional groups for ligand exchange include thiols, amines and carboxylic acids, with thiols typically classed as X-type ligands as they often appear deprotonated in solution. [139] As these ligands are negatively charged in solution, they can bind to the positively charged surface metal ions [128, 140], and thiol ligands are further stabilised by the formation of disulfide bonds with surface sulphur atoms present in ZnS shells and can become part of the crystal itself. [141–143] Using thiol ligands does require consideration of the functionalisation methods used after ligand exchange because at low pH, thiols can be protonated and removed from the CQD surface. [144] Multidentate ligands, such as bidentate thiols and oligomeric phosphines and even polymers can also be used for functionalisation of QDs and have been shown to enhance stability and quantum yields. [145] Ligand choice is incredibly important when functionalising a QD surface because the quantum yield is significantly affected by surface states. [144]

The reaction mechanism for the exchange between oleic acid and MPA is shown above in Fig 1.15. The exchange occurs at a 1:1 stoichiometry and occurs through an associative mechanism. [136] Oleic acid and thiol exchange is spontaneous because of the stronger binding thiols have with the CQD surface in comparison. [136, 144] The thermodynamics of ligand exchange is a very complex and varied picture of binding interactions, enthalpic and entropic contributions from ligand-ligand and ligand-solvent interactions. [146] Elimelech *et. al.* conducted a thorough study of the thermodynamics of this class of reaction by using isothermal titration calorimetry to measure the enthalpy and equilibrium constant of an exchange between oleic acid and a series of alkylthiols on the surface of CdSe CQDs. [136] Enthalpy measurements showed that

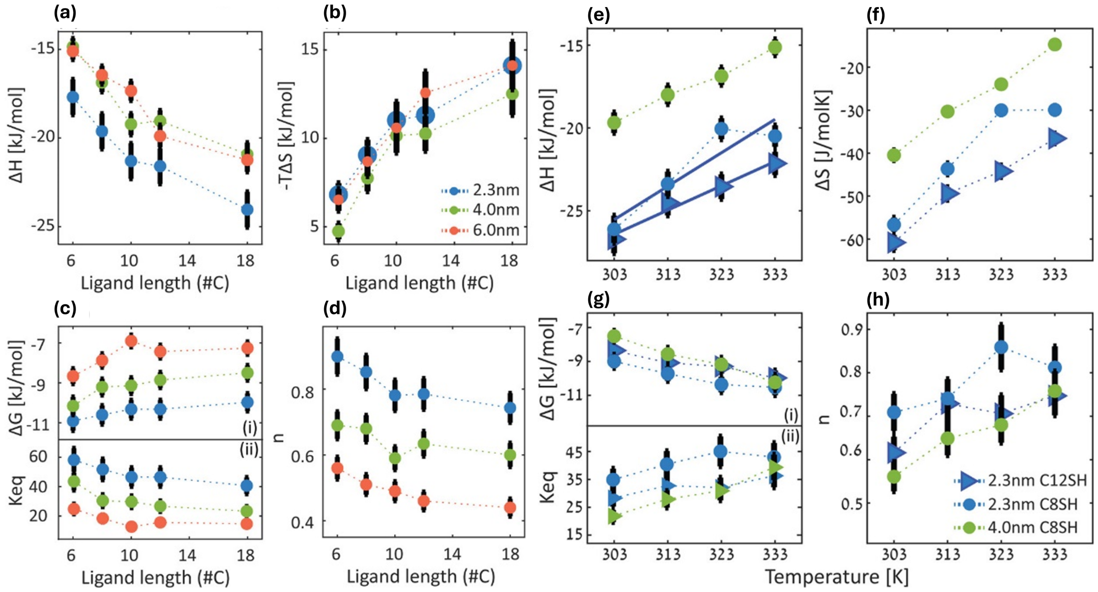

Figure 1.16: (a) CdSe CQDs ligand length dependence of the (a) enthalpy, (b) entropy, (c) (i) Gibbs free energy, (ii) equilibrium constant and (d) the reaction stoichiometry, n with different CQD diameters: d = 2.3 nm (blue), d = 4.0 nm (green) and d = 6.0 nm (orange). Temperature dependence of the (e) enthalpy, (f) entropy, (g) (i) Gibbs free energy and (h) n for ligand exchange between oleate and C12–SH (blue triangle with CQD d = 2.3 nm) and C8–SH (d = 2.3 nm, blue circle; d = 4.0 nm, green circle). Reproduced with permission from [136]

ligand exchange becomes more exothermic with increasing alkyl chain length which is compensated by the loss of entropy due to ligand packing on the surface. Called the enthalpy-entropy compensation effect, this is the result of longer alkyl chains forming stronger van der Waals interactions, increasing the enthalpy, while also restricting chain movement, reducing entropy, when the ligands are packed onto the QD surface, creating a near-constant Gibbs free energy for these reactions. These data are highlighted above in Figure 1.16a-d. This study also found that the smaller the QD, the higher the Gibbs energy because of the increased curvature and higher surface reactivity. As temperature increased, a significant increase in both enthalpy and entropy was observed as a result of different heat capacities of the reagents and different packing densities of the ligand shell respectively. The equilibrium constant, K_{eq}, was also found to increase as the temperature increased (Figure 1.16e-h), meaning that replacing the oleate is still favoured at higher temperatures, demonstrating a non-Le Chatelier's dependency of K_{eq} because ligand exchange is exothermic. Overall, this study concluded that replacement of oleic acid ligands is possible with alkylthiols due to the increased van der Waals forces from better packing and increased entropy of the alkylthiol-QD system compared to that of the oleic acid-QD system. This is because the oleic acid chains contain a double bond which deforms the chain and makes ligand packing less efficient on the QD surface. Presence of a double bond in oleic acid also results in a lack of rotation of the alkyl chain which, unfavourably, reduces the entropy of the system. A further study by this group studied ligand exchange between oleic acid and both linear and branched alkylthiols. This study found that the exchange becomes less exothermic and has a reduced loss of entropy for branched alkylthiols, attributed to the increased steric hindrance from ligand packing on the QD surface due to the presence of a single methyl group on the carbon backbone. On top of this, the position of the branching group on the carbon backbone and the length of the chain was also significant due to the importance of ligand packing on the thermodynamic viability of the exchange. [147] Some simulation studies have suggested that the loss of conformational entropy has a higher contribution to the thermodynamic picture of exchange than changes in the amount of van der Waals' forces present between ligands. [146–148] Overall, studies have found that exchange rate increases as the ligand chain length decreases, temperature increases and QD size decreases. [136,145,147] When designing a ligand exchange, solvent choice also requires consideration as some, such as THF, can coordinate to CQD surfaces and replace the desired ligands. [126] Ligand exchange is a widely used method for the first step of biofunctionalisation procedures, but it is also possible to use this method to improve optical characteristics. For example, the surface ligands of CQDs within SPs were replaced with a bidentate ligand diaminooctane, a ligand with two binding sites per molecule, to be able to pack CQDs more tightly within SPs. This significantly improved the optical characteristics of these SPs, which also demonstrated lasing *in vitro* and *in vivo*. [149] It is possible that MPA, the ligand used within this work, could act as a bidentate ligand however it is likely that the ligand chain is too small to be able to do this due to repulsion between CQDs.

Ligand exchange is often just the first step in the surface functionalisation of QDs as it is often used to make QDs water soluble and to introduce moieties to the surface that can undergo further chemical reactions. Achieving surface functionalisation for specific biological applications usually involves conjugation with biomolecules and recognition elements key to enabling QDs to recognise and target specific biomolecules. Covalent and non-covalent binding of biomolecules are the two main strategies utilised to functionalise a QD surface for biological applications. [118]

1.5.2 EDC/NHS Coupling

EDC/NHS coupling is a popular method for the conjugation of biomolecules to the surface of biosensors. *N*-(3-Dimethylaminopropyl)-*N'*-ethyl carbodiimide (EDC) and *N*-Hydroxysuccinimide (NHS) are used to couple between molecules containing carboxylic acid and amine groups with high reaction rates without the insertion of crosslinking or spacer groups. [118]. The reaction mechanism for the coupling is shown in Fig 1.17. In the first step, the carboxylic acid group on the SP surface courtesy of the MPA ligands is activated by EDC to decrease the nucleophilicity of the carboxyl carbon. This allows NHS to attack this more electron deficient carbon and complete the activation of the carboxylic acid. The biomolecule containing the primary amine is

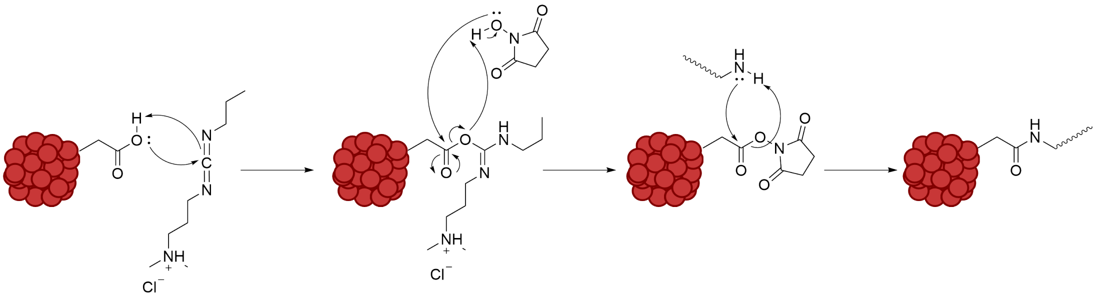

Figure 1.17: Reaction mechanism for the EDC/NHS coupling of DNA aptamer TBA-15 to the surface of SPs. In the first step, EDC activated the carboxylic acid at the SP surface. The second step shows the dispacement of EDC by NHS, followed by the third step of TBA addition to the SP surface and displacement of NHS to covalently couple the TBA to the SP surface, shown in the final step. Adapted from [150]

added to the solution and can then suitably attack the carboxyl carbon to covalently attach to the SP surface. [150] Due to the popularity of this reaction the optimal coupling conditions have been studied comprehensively, however the conclusion is not unanimous. A general estimate would be that the optimal conditions are the addition of NHS/EDC at a 2:1 ratio, the use of a buffer solution, and a pH of between 7 - 8.5. The lower the pH, the longer the reaction time and no reaction will occur at all if the pH is 3.5 and below. The activation step can take anywhere from 5 minutes up to 2 hours and coupling can take from 15 minutes up to 24 hours. [108, 150–152] Alongside this, full consideration must be given to the molecule being attached to the SP surface because if there are any primary amine groups available, coupling may take place at these sites as well as those desired. For the aptamer used in this work, TBA, the DNA chain is made up of guanine and thymine bases. Of these bases, guanine has one primary amine group attached to its aromatic ring, and one of the guanine bases is relatively accessible, however the mechanism of aptamer binding to thrombin does not involve that particular guanine therefore if EDC/NHS coupling occurs here it may not have an impact on the biosensing functionality of these SPs. [150,153,154] More detail on the structure of TBA is in Section 1.5.4. Arnold *et. al.* used EDC/NHS coupling to functionalise silica WGM microspheres with anti-MS2 antibodies to detect single MS2 virus. The technique used with these WGM microspheres was able to discriminate between specific binding of MS2 and non-specific binding of a different virus, Phix174 by washing with PBS buffer after addition of the viruses and monitoring the shift in the resonance wavelength. [83] Suo *et. al.* used EDC/NHS coupling to attach DNA aptamers to the surface of polystyrene microlasers to sense for specific cancer exosomes, which can be incredibly valuable for early detection of the disease in addition to uses for cancer therapy. [104] EDC/NHS coupling can also be used for surface functionalisation of QDs. Masteri-Farahani & Mosleh functionalised CdS CQDs with anti-methamphetamine antibodies to produce a turn-on fluorescence sensor for methamphetamine detection. For this functionalisation process, MAA capped CQDs were synthesised using a one-pot colloidal synthesis. EDC and NHS were then used to activate the carboxylic acid moieties on the CQD surface to couple antibodies to the surface. [112] Another strategy for attaching biomolecules to a QD surface is to exploit the avidin-biotin interaction. The avidin-biotin interaction has a high affinity, is highly selective and stable over a wide pH range. [155] Streptavidin is an analogue of avidin that is preferentially used instead of avidin in functionalisation procedures because it does not contain carbohydrates, is not charged and is a highly stable reagent that reduces non-specific binding which can affect sensor efficacy. [156] Streptavidin modified QDs are commercially available along with protein biotinylation kits, making this interaction remarkably easy to use for attaching functional groups and molecules to surfaces. Iyer *et. al.* attached three different enzymes, hen egg white lysozyme, alkaline phosphatase and acetylcholinesterase, by first biotinylating the enzyme then incubating the enzymes with streptavidin-modified QDs to generate quantum dot-enzyme bioconjugates. All three enzymes retained full catalytic activity after conjugation while the optical stability of the QDs also remained, demonstrating the suitability of biotin-avidin interactions for modifying a QD surface. [155]

1.5.3 Other Methods

There are other methods for surface functionalisation of QDs and WGM biosensors that are as widespread as the ones detailed above. One example of a covalent surface functionalisation technique is the use of click chemistry. Click chemistry describes a set of highly selective reactions that can be carried out in mild, aqueous conditions with high yields and reaction rates, first coined by Sharpless *et. al.* in 2001. [157,158] Some examples of click chemistry reactions include: the Diels-Alder ring formation, succinimidyl ester-amine coupling, thiol-ene, and Michael addition. [158–160] Functionalisation of QDs using click chemistry or functionalisation with clickable moieties for cell tagging and imaging has been demonstrated. Chen *et. al.* modified a CdSe/CdS QD surface with a norbornene ligand that can undergo click reactions with tetrazine due to norbornene being a highly strained bridged cycloalkene. This click reaction was used to attach PEG chains to the surface to make the QDs water soluble and further functionalisation of the dots with functional groups that could be attached to the other terminus of the PEG could be achieved. Azide functionalised QDs were synthesised using this approach and used in the labelling and imaging of 4T1 cancer cells. Cells were treated with a dibenzocyclooctyne (DBCO) bearing unnatural sugar that can be expressed on cell membranes through metabolic pathways within cells. When these pre-treated cells were incubated with the N_3-QDs, an azide-alkyne click reaction occurred between the QDs and the DBCO to attach the QDs to the cell surface for fluorescent labelling. [160] Mao *et. al.* exploited the same azide-alkyne click reaction to fabricate glucose detectors using DBCO modified glucose oxidase (GOx) and azide modified-CdTe:Zn^{2+} to create a GOx-QD complex. These complexes were used for rapid blood glucose detection and determination of blood glucose concentration within range of commercially available analysers. These QD-GOx complexes detected glucose based on the production of H_2O_2, from the GOx-catalysed oxidation of glucose, which quenches QD fluorescence. [161] Picard-Lafond and Morin synthesised carbon nanoparticles (NPs) using a bottom-up synthesis that leaves residual alkyne moieties on the surface. Photoinitiated thiol-yne click chemistry was used to attach a fluorescent pyrene ligand to the surface of carbon NPs to make the particles fluorescent for imaging as no photoluminescence was observed from the NPs before pyrene functionalisation. [162] These are but a few examples demonstrating the versatility and ease of click chemistry. However, for click chemistry to be used in biological applications, samples often require pre-treatment to attach clickable moieties to the target therefore quick, *in vivo*, detection would not be possible. These click reactions listed above would also result in the insertion of bulky spacer groups in addition to thiol-ene click chemistry between thiols and C=C double bonds requiring a copper catalyst or photoinitiation for the reaction to proceed, making this method unsuitable for use with QDs and where consideration of the size of the molecules immobilised on a surface is required. [159] In particular, alkylthiol coated QDs have been found to be unstable upon exposure to light as this can initiate the formation of disulfide bonds between ligands and cause ligand dissociation and maleimide groups required for the thiol-ene reaction are prone to hydrolysis in alkaline aqueous conditions which is unsuitable for biological applications. [163, 164] That being said, click chemistry is still a useful method to use for attaching functional molecules and biorecognition elements, such as GOx, to the surface of QDs for further use.

Other options include coating SPs in silica or polymer containing the required functional groups before further functionalisation. [140] Silica coating has been a successful SP functionalisation route within this group and further functionalisation was achieved through the attachment of a photocleavable ligand using EDC/NHS coupling. [88, 89] PEG, PVA, and PVP are possible polymers that could be used for surface modification of SPs as variations of these polymers with moieties suitable for further functionalisation are often commercially available. [124,132,165] Well-known biointeractions such as the biotin-avidin interaction can also be exploited for conjugation with the SP surface and has been used to attach enzymes and other biomolecules to QD surfaces or even as the method of attaching analyte to the QD for biosensing capabilities. [107,155,166] This interaction is well studied and has a high affinity, is highly selective and stable over a wide pH range which is favourable for the application of biosensors within human samples. [155] This method, however, does still involve introducing bulky molecules to the surface which could prove an issue for biosensing with WGM lasers. [118] Another option often used in literature is taking advantage of non-specific adsorption of large molecules to a QD surface, made possible due to the large surface area of QDs. Unfortunately, this interaction is weak and may be detrimental to the stability of SPs in different solutions. [118]

Overall, there are many cases of the avidin-biotin interaction being exploited to produce aptamer modified QDs for protein detection. However, QD-aptamer sensors are often used in conjunction with other particles, for example with fluorescence quenchers to make Fluorescence Resonance Energy Transfer (FRET) sensors [77,107,109,111] or molecularly imprinted polymers for a double recognition sensing method. [167] Whispering gallery mode resonators have also been modified with aptamers for sensing applications, however these are often made of silica or glass [168] and there has been no literature published at time of writing that involves the surface modification of self-assembled QD microsphere lasers with aptamers and subsequent testing of such sensors.

1.5.4 DNA Aptamers

Aptamers are engineered specific DNA and RNA sequences that can have high affinity and selectivity towards chosen target analytes. They are often preferred over antibodies for sensing applications due to their small size, ease of production, stability and easy modification. [90] These biomolecules owe their high selectivity to their 3D structure and binding mechanism, often described as a 'lock and key' mechanism. [24] Aptamers are also incredibly versatile and can be tailored to detect certain genes [24], proteins [76], and even metal ions. [97] Aptamers are discovered using a slow and expensive process called SELEX (Systematic Evolution of Ligands by Exponential Enrichment) which would be the main drawback of designing and manufacturing biosensors for biomolecules which do not have an already discovered and commercially available aptamer sequence. [24,169] The 15-base Thrombin Binding Aptamer (TBA) was among the first aptamers to be discovered in 1992 and is one of the most studied within research. [169,170] The structure of TBA-15 is shown below in Figure 5.2 and is described as a chair-like G-quadruplex structure because of its shape and two quartets of guanine (G) bases in the DNA chain. [75] This structure is also the reason TBA-15 is relatively stable in solution as the type of hydrogen bonds between bases and the π-π stacking of the aromatic rings in the guanine bases mean the structure is more resistant to degradation. [169] There is also a central cation between the guanine quartets - usually potassium - which also enhances the structural stability of TBA-15. [170] A popular target analyte for aptamer-modified biosensors is the protein Thrombin. Thrombin is involved in many pathological diseases, such as thrombosis and athero-

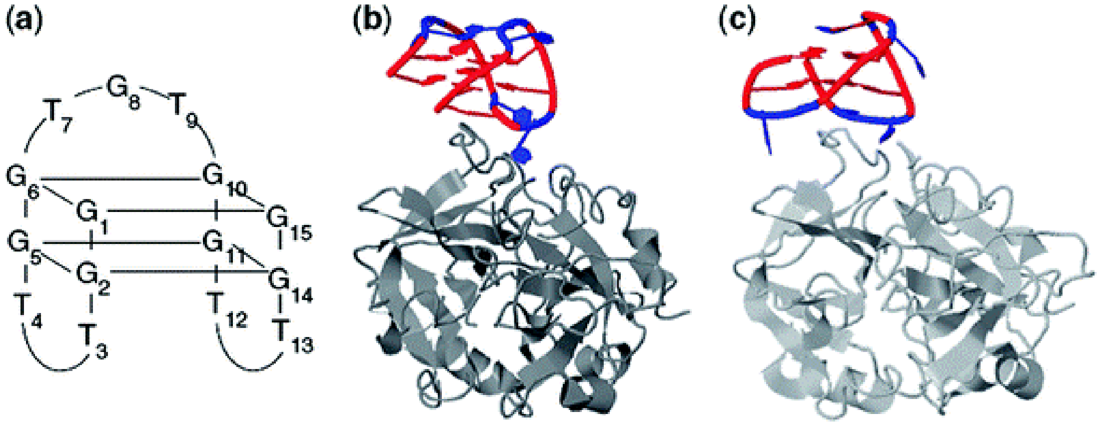

Figure 1.18: (a) Diagram of the quadruplex structure of TBA-15 and the interaction between TBA-15 and Thrombin exosite I according to (b) X-ray crystallography and (c) NMR spectroscopy studies. Reproduced with permission from [154].

sclerosis and functions as a coagulation factor; its presence in blood can indicate the presence of a blood clot. Thrombin protein has two different binding sites, generally referred to as exosite I and exosite II. Studies have shown that thrombin generally binds to TBA-15 through exosite I, shown in Figure 1.18, by the TT and TGT loops acting like pincers around the section of exosite I that protrudes slightly. [75]. Current methods of Thrombin detection are limited by the lack of antibodies available and can be time-consuming. [90,168] For the post-synthesis modification of QDs with aptamers, four different strategies can be used: self-assembly between DNA and QDs, biospecific interactions, covalent interactions and nucleic acid hybridisation. For example, the biospecific interaction between avidin and biotin can be used to attach aptamers to a QD surface. [117] One of the first pieces of literature detailing the use of aptamer functionalised QDs for Thrombin sensing was by Choi *et. al.* in 2006. In this case, aptamer modified near IR emitting PbS QDs were produced in a one-step synthesis and were used to successfully detect Thrombin. Detection was via PL quenching and had a detection limit of approximately 1 nM. However, this binding was found to be irreversible which is an important factor to consider when trying to develop facile and reusable Thrombin sensing devices. [79] Ligand exchange has also been used to attach aptamers to a QD surface. CdS and PbS QDs capped with organic thiol ligands were synthesised and ligand exchange carried out with two different thiol-modified aptamers to produce aptamer modified QDs. These conjugates were used for the detection of ATP and cocaine with detection limits measured to be 30 nM and 50 nM respectively, showing the promise of aptamer-based sensing. [119] Click chemistry has also been used to covalently bind aptamers to the surface of different types of QDs, NPs, and materials for biosensing applications. [158] Azide click reactions have been used to attach aptamers to the surface of metal-organic frameworks (MOFs) for drug delivery [171], and in the functionalisation of silica NPs for Thrombin detection. [172] Thiol-ene click chemistry has also been used to produce aptamer functionalised NPs for BSA protein sensing [173] and the functionalisation of different colloidal NPs for cell tagging [174]. EDC/NHS coupling is another method that has been used to covalently bind aptamers to the surface of QDs with Li *et. al.* using this technique to produce an aptamer-modified electrode as part of an electrochemiluminescence biosensor for the detection of Thrombin. [115]

1.6 Conclusion

In summary, this introduction has outlined the main motivations behind the research undertaken in this work and taken a brief tour of the basic scientific concepts required to understand the main points and conclusions of the thesis. The key takeaways of this chapter are how the the QCE results in CQDs being able to be used as an optical gain material, the basic principles of how WGM lasing works, and the thermodynamics behind ligand exchange at the surface of CQDs. This chapter also looked at the current state of the art technology within the literature, particularly with surface functionalisation techniques and the integration of WGM laser biosensors in microfluidic chips. The rest of this thesis will begin with the materials and methods used in this work, followed by a study to determine whether the emulsion used to fabricate SPs has an effect, if any, on the stability of SPs towards surface modification with the protein Neutravidin. Carrying on from this is the main results chapter which details the successful attempt to functionalise the surface of SPs with a Thrombin Binding Aptamer (TBA-15) to be able to create laser biosensors. Finally, a very simple proof of concept study was carried out to test whether SPs functionalised with TBA-15 could be used as biosensors for the protein Thrombin.

References

[1] F. Montanarella, D. Urbonas, L. Chadwick, P. G. Moerman, P. J. Baesjou, R. F. Mahrt, A. van Blaaderen, T. Stöferle, and D. Vanmaekelbergh, "Lasing Supraparticles Self-Assembled from Nanocrystals," *ACS Nano*, vol. 12, no. 12, pp. 12788–12794, 2018.

[2] J. Y. Kim, O. Voznyy, D. Zhitomirsky, and E. H. Sargent, "25th anniversary article: Colloidal quantum dot materials and devices: A quarter-century of advances," *Advanced Materials*, vol. 25, no. 36, pp. 4986–5010, 2013.

[3] A. I. Ekimov and A. A. Onushchenko, "Quantum Size Effect in Three-Dimensional Microscopic Semiconductor Crystals," *JETP Letters*, vol. 34, no. 6, pp. 345–349, 1981.

[4] R. Rossetti, S. Nakahara, and L. E. Brus, "Quantum size effects in the redox potentials, resonance Raman spectra, and electronic spectra of CdS crystallites in aqueous solution," *The Journal of Chemical Physics*, vol. 79, no. 2, pp. 1086–1088, 1983.

[5] C. B. Murray, D. J. Norris, and M. G. Bawendi, "Synthesis and characterization of nearly monodisperse CdE (E = sulfur, selenium, tellurium) semiconductor nanocrystallites," *Journal of the American Chemical Society*, vol. 115, no. 19, pp. 8706–8715, 1993.

[6] S. B. Brichkin and V. F. Razumov, "Colloidal quantum dots: synthesis, properties and applications," *Russian Chemical Reviews*, vol. 85, no. 12, pp. 1297–1312, 2016.

[7] Mark Fox, *Optical Properties of Solids*. New York: Oxford University Press, second ed., 2010.

[8] M. Bayer, “Bridging Two Worlds: Colloidal versus Epitaxial Quantum Dots,” *Annalen der Physik*, vol. 531, no. 6, p. 1900039, 2019.

[9] S. Real, O. Espíndola, M. P. Zelaya, O. Marin, D. Comedi, and M. Tirado, “Single-step Zno nanorod bunches formation on p-type Si-conductive substrates by electrophoretic deposition,” *Surfaces and Interfaces*, vol. 23, no. January, pp. 1–11, 2021.

[10] M. Makkar, G. Prakash, and R. Viswanatha, “Crystal Facet Engineering of CoPt Quantum Dots for Diverse Colloidal Heterostructures,” *Journal of Physical Chemistry Letters*, vol. 11, no. 16, pp. 6742–6748, 2020.

[11] B. Guzelturk, Y. Kelestemur, M. Olutas, S. Delikanli, and H. V. Demir, “Amplified Spontaneous Emission and Lasing in Colloidal Nanoplatelets,” *ACS Nano*, vol. 8, no. 7, pp. 6599–6605, 2014.

[12] M. J. Enright, F. Y. Dou, S. Wu, E. J. Rabe, M. Monahan, M. R. Friedfeld, C. W. Schlenker, and B. M. Cossairt, “Seeded Growth of Nanoscale Semiconductor Tetrapods: Generality and the Role of Cation Exchange,” *Chemistry of Materials*, vol. 32, no. 11, pp. 4774–4784, 2020.

[13] I. Moreels, G. Rainò, R. Gomes, Z. Hens, T. Stöferle, and R. F. Mahrt, “Nearly Temperature-Independent Threshold for Amplified Spontaneous Emission in Colloidal CdSe/CdS Quantum Dot-in-Rods,” *Advanced Materials*, vol. 24, pp. OP231–OP235, 9 2012.

[14] Y. Wang and H. Sun, “Advances and prospects of lasers developed from colloidal semiconductor nanostructures,” *Progress in Quantum Electronics*, vol. 60, no. 5, pp. 1–29, 2018.

[15] V. I. Klimov, “Nanocrystal Quantum Dots: From Fundamental Photophysics to Multicolour Lasing,” *Los Alamos Science*, vol. 28, pp. 214–220, 2003.

[16] L. J. Mclellan, *Colloidal quantum dot and hybrid lasers.* PhD thesis, University of Strathclyde, 2018.

[17] P. C. Sercel and A. L. Efros, “Band-Edge Exciton in CdSe and Other II–VI and III–V Compound Semiconductor Nanocrystals – Revisited,” *Nano Letters*, vol. 18, no. 7, pp. 4061–4068, 2018.

[18] F. García-Santamaría, S. Brovelli, R. Viswanatha, J. A. Hollingsworth, H. Htoon, S. A. Crooker, and V. I. Klimov, “Breakdown of volume scaling in auger recombination in CdSe/CdS heteronanocrystals: The role of the core-shell interface,” *Nano Letters*, vol. 11, no. 2, pp. 687–693, 2011.

[19] M. Achermann, J. A. Hollingsworth, and V. I. Klimov, “Multiexcitons confined within a subexcitonic volume: Spectroscopic and dynamical signatures of neutral and charged biexcitons in ultrasmall semiconductor nanocrystals,” *Physical Review B - Condensed Matter and Materials Physics*, vol. 68, no. 24, 2003.

[20] M. V. Kovalenko, L. Manna, A. Cabot, Z. Hens, D. V. Talapin, C. R. Kagan, V. I. Klimov, A. L. Rogach, P. Reiss, D. J. Milliron, P. Guyot-Sionnnest, G. Konstantatos, W. J. Parak, T. Hyeon, B. A. Korgel, C. B. Murray, and W. Heiss, “Prospects of nanoscience with nanocrystals,” *ACS Nano*, vol. 9, no. 2, pp. 1012–1057, 2015.

[21] F. García-Santamaría, Y. Chen, J. Vela, R. D. Schaller, J. A. Hollingsworth, and V. I. Klimov, “Suppressed auger recombination in ”Giant” nanocrystals boosts optical gain performance,” *Nano Letters*, vol. 9, no. 10, pp. 3482–3488, 2009.

[22] W. K. Bae, L. A. Padilha, Y. S. Park, H. McDaniel, I. Robel, J. M. Pietryga, and V. I. Klimov, “Controlled alloying of the core-shell interface in CdSe/CdS quantum dots for suppression of auger recombination,” *ACS Nano*, vol. 7, no. 4, pp. 3411–3419, 2013.

[23] F. Montanarella, T. Altantzis, D. Zanaga, F. T. Rabouw, S. Bals, P. Baesjou, D. Vanmaekelbergh, and A. van Blaaderen, “Composite Supraparticles with Tunable Light Emission,” *ACS Nano*, vol. 11, no. 9, pp. 9136–9142, 2017.

[24] M. Loyez, M. Adolphson, J. Liao, and L. Yang, "From Whispering Gallery Mode Resonators to Biochemical Sensors," *ACS Sensors*, vol. 8, no. 7, pp. 2440–2470, 2023.

[25] G. C. Righini and S. Soria, "Biosensing by WGM microspherical resonators," *Sensors (Switzerland)*, vol. 16, no. 6, p. 905, 2016.

[26] L. Cai, J. Pan, Y. Zhao, J. Wang, and S. Xiao, "Whispering Gallery Mode Optical Microresonators: Structures and Sensing Applications," *Physica Status Solidi (A) Applications and Materials Science*, vol. 217, no. 6, pp. 1–18, 2020.

[27] J. Ward and O. Benson, "WGM microresonators: sensing, lasing and fundamental optics with microspheres," *Laser & Photonics Reviews*, vol. 5, no. 4, pp. 553–570, 2011.

[28] J. Su, "Label-Free biological and chemical sensing using whispering gallery mode optical resonators: Past, present, and future," *Sensors (Switzerland)*, vol. 17, no. 3, pp. 1–18, 2017.

[29] A. Chiasera, Y. Dumeige, P. Féron, M. Ferrari, Y. Jestin, G. Nunzi Conti, S. Pelli, S. Soria, and G. Righini, "Spherical whispering-gallery-mode microresonators," *Laser & Photonics Reviews*, vol. 4, no. 3, pp. 457–482, 2010.

[30] I. Teraoka, S. Arnold, and F. Vollmer, "Perturbation approach to resonance shifts of whispering-gallery modes in a dielectric microsphere as a probe of a surrounding medium," *Journal of the Optical Society of America B*, vol. 20, no. 9, p. 1937, 2003.

[31] A. Francois and M. Himmelhaus, "Whispering gallery mode biosensor operated in the stimulated emission regime," *Applied Physics Letters*, vol. 94, no. 3, pp. 1–4, 2009.

[32] K. Gardner, Y. Zhi, L. Tan, S. Lane, Y.-F. Xiao, and A. Meldrum, "Whispering gallery mode structure in polymer-coated lasing microspheres," *Journal of the Optical Society of America B*, vol. 34, no. 10, p. 2140, 2017.

[33] A. V. Veluthandath and P. B. Bisht, “Radiative rate modification in CdSe quantum dot-coated microcavity,” *Journal of Applied Physics*, vol. 118, no. 23, p. 233102, 2015.

[34] H. T. Beier, G. L. Coté, and K. E. Meissner, “Modeling whispering gallery modes in quantum dot embedded polystyrene microspheres,” *Journal of the Optical Society of America B*, vol. 27, no. 3, p. 536, 2010.

[35] A. F. Monte, D. Rabelo, and P. C. Morais, “Optical properties of CdS nanoparticles embedded in polymeric microspheres,” *Journal of Alloys and Compounds*, vol. 495, no. 2, pp. 436–438, 2010.

[36] D. Vanmaekelbergh, L. K. Van Vugt, H. E. Bakker, F. T. Rabouw, B. D. Nijs, R. J. Van Dijk-Moes, M. A. Van Huis, P. J. Baesjou, and A. Van Blaaderen, “Shape-dependent multiexciton emission and whispering gallery modes in supraparticles of CdSe/multishell quantum dots,” *ACS Nano*, vol. 9, no. 4, pp. 3942–3950, 2015.

[37] H. Chang, Y. Zhong, H. Dong, Z. Wang, W. Xie, A. Pan, and L. Zhang, “Ultrastable low-cost colloidal quantum dot microlasers of operative temperature up to 450 K,” *Light: Science & Applications*, vol. 10, no. 1, p. 60, 2021.

[38] A. Aubret, A. Pillonnet, J. Houel, C. Dujardin, and F. Kulzer, “CdSe/ZnS quantum dots as sensors for the local refractive index,” *Nanoscale*, vol. 8, no. 4, pp. 2317–2325, 2016.

[39] Y. Wang, V. D. Ta, K. S. Leck, B. H. I. Tan, Z. Wang, T. He, C. D. Ohl, H. V. Demir, and H. Sun, “Robust Whispering-Gallery-Mode Microbubble Lasers from Colloidal Quantum Dots,” *Nano Letters*, vol. 17, no. 4, pp. 2640–2646, 2017.

[40] P. U. Alves, N. Laurand, and M. D. Dawson, “Multicolor laser oscillation in a single self-assembled colloidal quantum dot microsphere,” in *2020 IEEE Photonics Conference (IPC)*, pp. 1–2, IEEE, 2020.

[41] T. Reynolds, N. Riesen, A. Meldrum, X. Fan, J. M. M. Hall, T. M. Monro, and A. François, "Fluorescent and lasing whispering gallery mode microresonators for sensing applications," *Laser & Photonics Reviews*, vol. 11, no. 2, p. 1600265, 2017.

[42] Y. Du, C.-L. Zou, C. Zhang, K. Wang, C. Qiao, J. Yao, and Y. S. Zhao, "Tuneable red, green, and blue single-mode lasing in heterogeneously coupled organic spherical microcavities," *Light: Science & Applications*, vol. 9, no. 1, p. 151, 2020.

[43] S. Akbari and A. H. Nour, "Emulsion types, stability mechanisms and rheology: A review," *International Journal of Innovative Research and Scientific Studies*, vol. 1, no. 1, pp. 11–17, 2018.

[44] T. F. Tadros, "Emulsion Science and Technology: A General Introduction," in *Emulsion Science and Technology* (T. F. Tadros, ed.), ch. 1, pp. 1–56, John WIley & Sons, 2009.

[45] R. J. Lopetinsky, J. H. Masliyah, and Z. Xu, "Solids-Stabilized Emulsions: A Review," in *Colloidal Particles at Liquid Interfaces*, vol. 9780521848, pp. 186–224, Cambridge University Press, 2006.

[46] V. N. Manoharan, "Colloidal spheres confined by liquid droplets: Geometry, physics, and physical chemistry," *Solid State Communications*, vol. 139, no. 11-12, pp. 557–561, 2006.

[47] T. F. Tadros, "Emulsion Formation, Stability, and Rheology," in *Emulsion Formation and Stability* (T. F. Tadros, ed.), ch. 1, pp. 1–75, John Wiley & Sons, first ed., 2013.

[48] E. Marino, T. E. Kodger, G. H. Wegdam, and P. Schall, "Revealing Driving Forces in Quantum Dot Supercrystal Assembly," *Advanced Materials*, vol. 30, no. 43, 2018.

[49] E. Marino, R. A. LaCour, T. C. Moore, S. W. van Dongen, A. W. Keller, D. An, S. Yang, D. J. Rosen, G. Gouget, E. H. R. Tsai, C. R. Kagan, T. E. Kodger, S. C.

Glotzer, and C. B. Murray, “Crystallization of binary nanocrystal superlattices and the relevance of short-range attraction,” *Nature Synthesis*, vol. 3, no. 1, pp. 111–122, 2023.

[50] F. Montanarella, J. J. Geuchies, T. Dasgupta, P. T. Prins, C. van Overbeek, R. Dattani, P. Baesjou, M. Dijkstra, A. V. Petukhov, A. van Blaaderen, and D. Vanmaekelbergh, “Crystallization of Nanocrystals in Spherical Confinement Probed by in Situ X-ray Scattering,” *Nano Letters*, vol. 18, no. 6, pp. 3675–3681, 2018.

[51] E. Marino, A. W. Keller, D. An, S. van Dongen, T. E. Kodger, K. E. MacArthur, M. Heggen, C. R. Kagan, C. B. Murray, and P. Schall, “Favoring the Growth of High-Quality, Three-Dimensional Supercrystals of Nanocrystals,” *The Journal of Physical Chemistry C*, vol. 124, no. 20, pp. 11256–11264, 2020.

[52] T. Brugarolas, F. Tu, and D. Lee, “Directed assembly of particles using microfluidic droplets and bubbles,” *Soft Matter*, vol. 9, no. 38, p. 9046, 2013.

[53] S. Wintzheimer, T. Granath, M. Oppmann, T. Kister, T. Thai, T. Kraus, N. Vogel, and K. Mandel, “Supraparticles: Functionality from Uniform Structural Motifs,” *ACS Nano*, vol. 12, no. 6, pp. 5093–5120, 2018.

[54] K. Hou, J. Han, and Z. Tang, “Formation of Supraparticles and Their Application in Catalysis,” *ACS Materials Letters*, vol. 2, no. 1, pp. 95–106, 2020.

[55] T. Kister, M. Mravlak, T. Schilling, and T. Kraus, “Pressure-controlled formation of crystalline, Janus, and core–shell supraparticles,” *Nanoscale*, vol. 8, no. 27, pp. 13377–13384, 2016.

[56] C. Wu, Q. Fan, and Y. Yin, “Emulsion-confined self-assembly of colloidal nanoparticles into 3D superstructures,” *Cell Reports Physical Science*, vol. 3, no. 12, p. 101162, 2022.

[57] A. Plunkett, C. Eldridge, G. A. Schneider, and B. Domènech, "Controlling the Large-Scale Fabrication of Supraparticles," *The Journal of Physical Chemistry B*, vol. 124, no. 49, pp. 11263–11272, 2020.

[58] W. Chen, L. Wang, R. Liu, H. Shen, J. Du, and F. Fan, "Self-Assembled and Wavelength-Tunable Quantum Dot Whispering-Gallery-Mode Lasers for Backlight Displays," *Nano Letters*, vol. 23, no. 2, pp. 437–443, 2023.

[59] W.-g. Chen, R.-x. Liu, and F.-j. Fan, "Flexible colloidal quantum dot lasers enabled by self-assembly," *Chinese Journal of Chemical Physics*, vol. 36, no. 6, pp. 679–684, 2023.

[60] D. Luo, C. Yan, and T. Wang, "Interparticle Forces Underlying Nanoparticle Self-Assemblies," *Small*, vol. 11, no. 45, pp. 5984–6008, 2015.

[61] D. Luo, X. Qin, Q. Song, X. Qiao, Z. Zhang, Z. Xue, C. Liu, G. Mo, and T. Wang, "Ordered Superparticles with an Enhanced Photoelectric Effect by Sub-Nanometer Interparticle Distance," *Advanced Functional Materials*, vol. 27, no. 44, p. 1701982, 2017.

[62] B. Le Feber, F. Prins, E. De Leo, F. T. Rabouw, and D. J. Norris, "Colloidal-Quantum-Dot Ring Lasers with Active Color Control," *Nano Letters*, vol. 18, no. 2, pp. 1028–1034, 2018.

[63] N. Vogel, S. Utech, G. T. England, T. Shirman, K. R. Phillips, N. Koay, I. B. Burgess, M. Kolle, D. A. Weitz, and J. Aizenberg, "Color from hierarchy: Diverse optical properties of micron-sized spherical colloidal assemblies," *Proceedings of the National Academy of Sciences*, vol. 112, no. 35, pp. 10845–10850, 2015.

[64] J. Wang, E. Kang, U. Sultan, B. Merle, A. Inayat, B. Graczykowski, G. Fytas, and N. Vogel, "Influence of Surfactant-Mediated Interparticle Contacts on the Mechanical Stability of Supraparticles," *The Journal of Physical Chemistry C*, vol. 125, no. 42, pp. 23445–23456, 2021.

[65] H. Hwang, Y. C. Cho, S. Lee, T. M. Choi, S. H. Kim, and G. W. Lee, “Real-Time Monitoring of Colloidal Crystallization in Electrostatically-Levitated Drops,” *Small*, vol. 16, no. 11, 2020.

[66] W. Liu, M. Kappl, W. Steffen, and H. J. Butt, “Controlling supraparticle shape and structure by tuning colloidal interactions,” *Journal of Colloid and Interface Science*, vol. 607, pp. 1661–1670, 2022.

[67] V. D. Ta, S. Caixeiro, F. M. Fernandes, and R. Sapienza, “Microsphere Solid-State Biolasers,” *Advanced Optical Materials*, vol. 5, no. 8, p. 1601022, 2017.

[68] O. D. Velev, A. M. Lenhoff, and E. W. Kaler, “A Class of Microstructured Particles Through Colloidal Crystallization,” *Science*, vol. 287, no. 5461, pp. 2240–2243, 2000.

[69] J. Lacava, P. Born, and T. Kraus, “Nanoparticle Clusters with Lennard-Jones Geometries,” *Nano Letters*, vol. 12, no. 6, pp. 3279–3282, 2012.

[70] Y. Chen, Z. Yao, S. Tang, H. Tong, T. Yanagishima, H. Tanaka, and P. Tan, “Morphology selection kinetics of crystallization in a sphere,” *Nature Physics*, vol. 17, no. 1, pp. 121–127, 2021.

[71] J. Wang, J. Schwenger, A. Ströbel, P. Feldner, P. Herre, S. Romeis, W. Peukert, B. Merle, and N. Vogel, “Mechanics of colloidal supraparticles under compression,” *Science Advances*, vol. 7, no. 42, pp. 954–967, 2021.

[72] B. de Nijs, S. Dussi, F. Smallenburg, J. D. Meeldijk, D. J. Groenendijk, L. Filion, A. Imhof, A. van Blaaderen, and M. Dijkstra, “Entropy-driven formation of large icosahedral colloidal clusters by spherical confinement,” *Nature Materials*, vol. 14, no. 1, pp. 56–60, 2015.

[73] P. U. Alves, D. Jevtics, M. J. Strain, M. D. Dawson, and N. Laurand, “Enhancing self-assembled colloidal quantum dot microsphere lasers,” in *2021 IEEE Photonics Conference (IPC)*, pp. 1–2, IEEE, 2021.

[74] P. U. Alves, D. Jevtics, M. J. Strain, M. D. Dawson, and N. Laurand, "Enhancing the luminescence efficiency of colloidal quantum dots in compound supraparticles," in *2023 IEEE Photonics Conference (IPC)*, pp. 1–2, IEEE, 2023.

[75] A. Pica, I. Russo Krauss, A. Merlino, S. Nagatoishi, N. Sugimoto, and F. Sica, "Dissecting the contribution of thrombin exosite I in the recognition of thrombin binding aptamer," *FEBS Journal*, vol. 280, no. 24, pp. 6581–6588, 2013.

[76] X. Cao, Y. Luo, X. Liu, C. Shang, J. Lu, G. Song, and C. Deng, "Aptamer-thrombin loaded magnetic microspheres for bio-specific extraction and precise detection of hirudin," *Talanta*, vol. 267, no. August 2023, p. 125244, 2024.

[77] C. Wang, C. Y. Lim, E. Choi, Y. Park, and J. Park, "Highly sensitive user friendly thrombin detection using emission light guidance from quantum dots-aptamer beacons in 3-dimensional photonic crystal," *Sensors and Actuators B: Chemical*, vol. 223, pp. 372–378, 2016.

[78] W. C. Chan and S. Nie, "Quantum dot bioconjugates for ultrasensitive nonisotopic detection," *Science*, vol. 281, no. 5385, pp. 2016–2018, 1998.

[79] J. H. Choi, K. H. Chen, and M. S. Strano, "Aptamer-capped nanocrystal quantum dots: A new method for label-free protein detection," *Journal of the American Chemical Society*, vol. 128, no. 49, pp. 15584–15585, 2006.

[80] H. Zhu, J. D. Suter, I. M. White, and X. Fan, "Aptamer based microsphere biosensor for thrombin detection," *Sensors*, vol. 6, pp. 785–795, 8 2006.

[81] F. Vollmer and D. Yu, "Single-Molecule Sensing," in *Optical Whispering Gallery Modes for Biosensing: From Physical Principles to Applications* (B. S. F. I. U. Gerstman, ed.), Biological and Medical Physics, Biomedical Engineering, ch. 5, pp. 233–298, Cham: Springer International Publishing, 1 ed., 2020.

[82] X.-C. Yu, S.-J. Tang, W. Liu, Y. Xu, Q. Gong, Y.-L. Chen, and Y.-F. Xiao, "Single-molecule optofluidic microsensor with interface whispering gal-

lery modes," *Proceedings of the National Academy of Sciences*, vol. 119, no. 6, p. e2108678119, 2022.

[83] S. Arnold, R. Ramjit, D. Keng, V. Kolchenko, and I. Teraoka, "MicroParticle photophysics illuminates viral bio-sensing," *Faraday Discuss.*, vol. 137, pp. 65–83, 2008.

[84] N. Bhalla, P. Jolly, N. Formisano, and P. Estrela, "Introduction to biosensors," *Essays in Biochemistry*, vol. 60, pp. 1–8, 6 2016.

[85] S. Yang, Y. Wang, and H. Sun, "Advances and Prospects for Whispering Gallery Mode Microcavities," *Advanced Optical Materials*, vol. 3, no. 9, pp. 1136–1162, 2015.

[86] M. Humar and S. H. Yun, "Whispering-gallery-mode emission from biological luminescent protein microcavity assemblies," *Optica*, vol. 4, p. 222, 2 2017.

[87] O. Gaathon, J. Culic-Viskota, M. Mihnev, I. Teraoka, and S. Arnold, "Enhancing sensitivity of a whispering gallery mode biosensor by subwavelength confinement," *Applied Physics Letters*, vol. 89, no. 22, p. 223901, 2006.

[88] C. J. Eling, N. Laurand, N.-K. Gunasekar, P. R. Edwards, and R. W. Martin, "Silica Coated Colloidal Semiconductor Quantum Dot Supracrystal Microlasers," in *2022 IEEE Photonics Conference (IPC)*, pp. 1–2, IEEE, 2022.

[89] C. J. Eling, N. Bruce, N.-K. Gunasekar, P. U. Alves, P. R. Edwards, R. W. Martin, and N. Laurand, "Biotinylated Photocleavable Semiconductor Colloidal Quantum Dot Supraparticle Microlaser," *ACS Applied Nano Materials*, vol. 7, no. 8, pp. 9159–9166, 2024.

[90] L. Pasquardini, S. Berneschi, A. Barucci, F. Cosi, R. Dallapiccola, M. Insinna, L. Lunelli, G. N. Conti, C. Pederzolli, S. Salvadori, and S. Soria, "Whispering gallery mode aptasensors for detection of blood proteins," *Journal of Biophotonics*, vol. 6, no. 2, pp. 178–187, 2013.

[91] L. Echeveria, S. Gilmore, S. Harrison, K. Heinz, A. Chang, G. Nunz-COnti, F. Cosi, P. Singh, and T. C. Bond, “Versatile bio-organism detection using microspheres for future biodegradation and bioremediation studies,” in *Laser Resonators, Microresonators, and Beam Control XXII* (A. M. Armani, A. V. Kudryashov, A. H. Paxton, and V. S. Ilchenko, eds.), vol. 11266, p. 50, SPIE, 3 2020.

[92] S. Arnold, S. I. Shopova, and S. Holler, “Whispering gallery mode bio-sensor for label-free detection of single molecules: thermo-optic vs reactive mechanism,” *Optics Express*, vol. 18, p. 281, 1 2010.

[93] G. Nunzi Conti, F. Baldini, S. Berneschi, D. Farnesi, A. Giannetti, S. Soria, C. Trono, L. Lunelli, L. Pasquardini, and C. Pederzolli, “Whispering gallery mode microresonators: results on aptasensors and on a new sensing approach,” in *Laser Resonators, Microresonators, and Beam Control XV* (A. V. Kudryashov, A. H. Paxton, V. S. Ilchenko, L. Aschke, and K. Washio, eds.), vol. 8600, p. 86001O, SPIE, 2013.

[94] C. E. Soteropulos, K. M. Zurick, M. T. Bernards, and H. K. Hunt, “Tailoring the protein adsorption properties of whispering gallery mode optical biosensors,” *Langmuir*, vol. 28, no. 44, pp. 15743–15750, 2012.

[95] A. Capocefalo, S. Gentilini, L. Barolo, P. Baiocco, C. Conti, and N. Ghofraniha, “Biosensing with free space whispering gallery mode microlasers,” *Photonics Research*, vol. 11, no. 5, p. 732, 2023.

[96] T. Reynolds, A. François, N. Riesen, M. E. Turvey, S. J. Nicholls, P. Hoffmann, and T. M. Monro, “Using whispering gallery mode micro lasers for biosensing within undiluted serum,” in *SPIE BioPhotonics Australasia* (M. R. Hutchinson and E. M. Goldys, eds.), vol. 10013, p. 100132X, SPIE, 2016.

[97] F. Wu, Y. Wu, Z. Niu, and F. Vollmer, “Integrating a DNA Strand Displacement Reaction with a Whispering Gallery Mode Sensor for Label-Free Mercury (II) Ion Detection,” *Sensors*, vol. 16, no. 8, p. 1197, 2016.

[98] M. C. Houghton, S. V. Kashanian, T. L. Derrien, K. Masuda, and F. Vollmer, "Whispering-Gallery Mode Optoplasmonic Microcavities: From Advanced Single-Molecule Sensors and Microlasers to Applications in Synthetic Biology," *ACS Photonics*, vol. 11, no. 3, pp. 892–903, 2024.

[99] X. Ouyang, T. Liu, Y. Zhang, J. He, Z. He, A. P. Zhang, and H. Y. Tam, "Ultrasensitive optofluidic enzyme-linked immunosorbent assay by on-chip integrated polymer whispering-gallery-mode microlaser sensors," *Lab on a Chip*, vol. 20, no. 14, pp. 2438–2446, 2020.

[100] B. Guan, T.-W. Kok, N. Riesen, D. Lancaster, K. Suu, and C. Priest, "Microsphere-Enabled Micropillar Array for Whispering Gallery Mode Virus Detection," *ACS Applied Materials & Interfaces*, vol. 16, no. 9, pp. 12042–12051, 2024.

[101] J. Álvarez Freile, G. Choukrani, K. Zimmermann, E. Bremer, and L. Dähne, "Whispering Gallery Modes-based biosensors for real-time monitoring and binding characterization of antibody-based cancer immunotherapeutics," *Sensors and Actuators B: Chemical*, vol. 346, p. 130512, 2021.

[102] J. S. Cognetti, M. T. Moen, M. G. Brewer, M. R. Bryan, J. D. Tice, J. L. McGrath, and B. L. Miller, "A photonic biosensor-integrated tissue chip platform for real-time sensing of lung epithelial inflammatory markers," *Lab on a Chip*, vol. 23, no. 2, pp. 239–250, 2023.

[103] Z. Wang, G. Fang, Z. Gao, Y. Liao, C. Gong, M. Kim, G.-E. Chang, S. Feng, T. Xu, T. Liu, and Y.-C. Chen, "Autonomous Microlasers for Profiling Extracellular Vesicles from Cancer Spheroids," *Nano Letters*, vol. 23, no. 7, pp. 2502–2510, 2023.

[104] M. Suo, Y. Fu, S. Wang, S. Lin, J. Zhang, C. Wu, H. Yin, P. Wang, W. Zhang, and X.-H. Wang, "Miniaturized Laser Probe for Exosome-Based Cancer Liquid Biopsy," *Analytical Chemistry*, vol. 96, no. 5, pp. 1965–1976, 2024.

[105] M. Schubert, A. Steude, P. Liehm, N. M. Kronenberg, M. Karl, E. C. Campbell, S. J. Powis, and M. C. Gather, "Lasing within Live Cells Containing Intracellular Optical Microresonators for Barcode-Type Cell Tagging and Tracking," *Nano Letters*, vol. 15, no. 8, pp. 5647–5652, 2015.

[106] A. H. Fikouras, M. Schubert, M. Karl, J. D. Kumar, S. J. Powis, A. Di Falco, and M. C. Gather, "Non-obstructive intracellular nanolasers," *Nature Communications*, vol. 9, no. 1, pp. 1–7, 2018.

[107] J. Liu, H. L. Jung, and Y. Lu, "Quantum dot encoding of aptamer-linked nanostructures for one-pot simultaneous detection of multiple analytes," *Analytical Chemistry*, vol. 79, no. 11, pp. 4120–4125, 2007.

[108] Y. H. Lao, C. W. Chi, S. M. Friedrich, K. Peck, T. H. Wang, K. W. Leong, and L. C. Chen, "Signal-on Protein Detection via Dye Translocation between Aptamer and Quantum Dot," *ACS Applied Materials and Interfaces*, vol. 8, no. 19, pp. 12048–12055, 2016.

[109] M. Levy, S. F. Cater, and A. D. Ellington, "Quantum-Dot Aptamer Beacons for the Detection of Proteins," *ChemBioChem*, vol. 6, no. 12, pp. 2163–2166, 2005.

[110] C. S. Martins, A. P. Lagrow, and J. A. Prior, "Quantum Dots for Cancer-Related miRNA Monitoring," *ACS Sensors*, vol. 7, no. 5, pp. 1269–1299, 2022.

[111] S. Wu, N. Duan, X. Ma, Y. Xia, H. Wang, Z. Wang, and Q. Zhang, "Multiplexed fluorescence resonance energy transfer aptasensor between upconversion nanoparticles and graphene oxide for the simultaneous determination of mycotoxins," *Analytical Chemistry*, vol. 84, no. 14, pp. 6263–6270, 2012.

[112] M. Masteri-Farahani and N. Mosleh, "Modified CdS quantum dots as selective turn-on fluorescent nanosensor for detection and determination of methamphetamine," *Journal of Materials Science: Materials in Electronics*, vol. 30, no. 24, pp. 21170–21176, 2019.

[113] P. Li, C. Luo, X. Chen, and C. Huang, "An off-on fluorescence aptasensor for trace thrombin detection based on FRET between CdS QDs and AuNPs," *RSC Advances*, vol. 12, no. 55, pp. 35763–35769, 2022.

[114] C. W. Chi, Y. H. Lao, Y. S. Li, and L. C. Chen, "A quantum dot-aptamer beacon using a DNA intercalating dye as the FRET reporter: Application to label-free thrombin detection," *Biosensors and Bioelectronics*, vol. 26, no. 7, pp. 3346–3352, 2011.

[115] Y. Li, L. Liu, X. Fang, J. Bao, M. Han, and Z. Dai, "Electrochemiluminescence biosensor based on CdSe quantum dots for the detection of thrombin," *Electrochimica Acta*, vol. 65, pp. 1–6, 2012.

[116] H. Huang and J. J. Zhu, "DNA aptamer-based QDs electrochemiluminescence biosensor for the detection of thrombin," *Biosensors and Bioelectronics*, vol. 25, no. 4, pp. 927–930, 2009.

[117] L. Wen, L. Qiu, Y. Wu, X. Hu, and X. Zhang, "Aptamer-modified semiconductor quantum dots for biosensing applications," *Sensors (Switzerland)*, vol. 17, no. 8, 2017.

[118] I. V. Martynenko, A. P. Litvin, F. Purcell-Milton, A. V. Baranov, A. V. Fedorov, and Y. K. Gun'Ko, "Application of semiconductor quantum dots in bioimaging and biosensing," *Journal of Materials Chemistry B*, vol. 5, no. 33, pp. 6701–6727, 2017.

[119] H. Zhang, B. Jiang, Y. Xiang, Y. Zhang, Y. Chai, and R. Yuan, "Aptamer/quantum dot-based simultaneous electrochemical detection of multiple small molecules," *Analytica Chimica Acta*, vol. 688, no. 2, pp. 99–103, 2011.

[120] F. Vollmer, S. Arnold, and D. Keng, "Single virus detection from the reactive shift of a whispering-gallery mode," *Proceedings of the National Academy of Sciences*, vol. 105, no. 52, pp. 20701–20704, 2008.

[121] Z. Wang, Y. Zhang, X. Gong, Z. Yuan, S. Feng, T. Xu, T. Liu, and Y. C. Chen, "Bio-electrostatic sensitive droplet lasers for molecular detection," *Nanoscale Advances*, vol. 2, no. 7, pp. 2713–2719, 2020.

[122] M. Charlebois, A. Paquet, L. S. Verret, K. Boissinot, M. Boissinot, M. G. Bergeron, and C. N. Allen, "Toward Automatic Label-Free Whispering Gallery Modes Biodetection with a Quantum Dot-Coated Microsphere Population," *Nanoscale Research Letters*, vol. 5, no. 3, pp. 524–532, 2010.

[123] G. Xu, G. Lin, S. Lin, N. Wu, Y. Deng, G. Feng, Q. Chen, J. Qu, D. Chen, S. Chen, H. Niu, S. Mei, K.-T. Yong, and X. Wang, "The Reproductive Toxicity of CdSe/ZnS Quantum Dots on the in vivo Ovarian Function and in vitro Fertilization," *Scientific Reports*, vol. 6, no. 1, p. 37677, 2016.

[124] A. Sabah, S. Tasleem, M. Murtaza, M. Nazir, and F. Rashid, "Effect of Polymer Capping on Photonic Multi-Core–Shell Quantum Dots CdSe/CdS/ZnS: Impact of Sunlight and Antibacterial Activity," *The Journal of Physical Chemistry C*, vol. 124, no. 16, pp. 9009–9020, 2020.

[125] A. Nagy, A. Steinbrück, J. Gao, N. Doggett, J. A. Hollingsworth, and R. Iyer, "Comprehensive analysis of the effects of CdSe quantum dot size, surface charge, and functionalization on primary human lung cells," *ACS Nano*, vol. 6, no. 6, pp. 4748–4762, 2012.

[126] J. J. Calvin, A. S. Brewer, and A. P. Alivisatos, "The role of organic ligand shell structures in colloidal nanocrystal synthesis," *Nature Synthesis*, vol. 1, no. 2, pp. 127–137, 2022.

[127] M. Liu, Z.-Y. Chen, X.-H. He, X.-Y. Liu, H.-L. Hu, H. Tian, Y. Liu, and F.-L. Jiang, "Thermodynamics of Ligand Exchange with Aromatic Ligands on the Surface of CdSe Quantum Dots," *Chemistry of Materials*, vol. 35, no. 5, pp. 1868–1876, 2023.

[128] M. A. Boles, D. Ling, T. Hyeon, and D. V. Talapin, "The surface science of nanocrystals," *Nature Materials*, vol. 15, no. 2, pp. 141–153, 2016.

[129] J. Owen, "The coordination chemistry of nanocrystal surfaces," *Science*, vol. 347, no. 6222, pp. 615–616, 2015.

[130] S. A. Rahman, N. Ariffin, N. A. Yusof, J. Abdullah, F. Mohammad, Z. A. Zubir, and N. M. A. N. A. Aziz, "Thiolate-capped CdSe/ZnS core-shell quantum dots for the sensitive detection of glucose," *Sensors (Switzerland)*, vol. 17, no. 7, pp. 1–12, 2017.

[131] M. Miropoltsev, K. D. Wegner, I. Häusler, V. D. Hodoroaba, and U. Resch-Genger, "Influence of Hydrophilic Thiol Ligands of Varying Denticity on the Luminescence Properties and Colloidal Stability of Quaternary Semiconductor Nanocrystals," *Journal of Physical Chemistry C*, vol. 126, no. 47, pp. 20101–20113, 2022.

[132] A. B. Greytak, S. L. Abiodun, J. M. Burrell, E. N. Cook, N. P. Jayaweera, M. M. Islam, and A. E. Shaker, "Thermodynamics of nanocrystal–ligand binding through isothermal titration calorimetry," *Chemical Communications*, vol. 58, no. 94, pp. 13037–13058, 2022.

[133] N. Singh, S. Prajapati, Prateek, and R. K. Gupta, "Investigation of Ag doping and ligand engineering on green synthesized CdS quantum dots for tuning their optical properties," *Nanofabrication*, vol. 7, pp. 89–103, 2022.

[134] G. Von White, F. S. Mohammed, and C. L. Kitchens, "Small-Angle Neutron Scattering Investigation of Gold Nanoparticle Clustering and Ligand Structure Under Antisolvent Conditions," *The Journal of Physical Chemistry C*, vol. 115, no. 38, pp. 18397–18405, 2011.

[135] D. P. Nenon, K. Pressler, J. Kang, B. A. Koscher, J. H. Olshansky, W. T. Osowiecki, M. A. Koc, L.-W. Wang, and A. P. Alivisatos, "Design Principles for Trap-Free CsPbX3 Nanocrystals: Enumerating and Eliminating Surface Halide Vacancies with Softer Lewis Bases," *Journal of the American Chemical Society*, vol. 140, no. 50, pp. 17760–17772, 2018.

[136] O. Elimelech, O. Aviv, M. Oded, and U. Banin, “A Tale of Tails: Thermodynamics of CdSe Nanocrystal Surface Ligand Exchange,” *Nano Letters*, vol. 20, no. 9, pp. 6396–6403, 2020.

[137] C. Yi, Y. Pan, and Y. Fang, “Surface Engineering of Carbon Nanodots (C-Dots) for Biomedical Applications,” in *Novel Nanomaterials for Biomedical, Environmental and Energy Applications*, pp. 137–188, Elsevier, 2019.

[138] X. Zhou, Z. Pang, W. Cao, Z. Cao, J. Zhu, Y. Qi, X. Peng, and X. Kong, “Diffusion NMR for Measuring Dynamic Ligand Exchange on Colloidal Nanocrystals,” *Analytical Chemistry*, vol. 95, no. 2, pp. 792–801, 2022.

[139] J. De Roo, “The Surface Chemistry of Colloidal Nanocrystals Capped by Organic Ligands,” *Chemistry of Materials*, vol. 35, no. 10, pp. 3781–3792, 2023.

[140] Y. Huang, T. A. Cohen, B. M. Sperry, H. Larson, H. A. Nguyen, M. K. Homer, F. Y. Dou, L. M. Jacoby, B. M. Cossairt, D. R. Gamelin, and C. K. Luscombe, “Organic building blocks at inorganic nanomaterial interfaces,” *Materials Horizons*, vol. 9, pp. 61–87, 1 2022.

[141] A. S. Karakoti, R. Shukla, R. Shanker, and S. Singh, “Surface functionalization of quantum dots for biological applications,” *Advances in Colloid and Interface Science*, vol. 215, pp. 28–45, 2015.

[142] N. T. Vo, H. D. Ngo, N. P. Do Thi, K. P. Nguyen Thi, A. P. Duong, and V. Lam, “Stability Investigation of Ligand-Exchanged CdSe/ZnS-Y (Y = 3-Mercaptopropionic Acid or Mercaptosuccinic Acid) through Zeta Potential Measurements,” *Journal of Nanomaterials*, vol. 2016, pp. 1–8, 2016.

[143] J. Choi, W. Choi, and D. Y. Jeon, “Ligand-Exchange-Ready CuInS2/ZnS Quantum Dots via Surface-Ligand Composition Control for Film-Type Display Devices,” *ACS Applied Nano Materials*, vol. 2, no. 9, pp. 5504–5511, 2019.

[144] Y. Zhang and A. Clapp, “Overview of Stabilizing Ligands for Biocompatible Quantum Dot Nanocrystals,” *Sensors*, vol. 11, no. 12, pp. 11036–11055, 2011.

[145] J. Aldana, N. Lavelle, Y. Wang, and X. Peng, “Size-dependent dissociation pH of thiolate ligands from cadmium chalcogenide nanocrystals,” *Journal of the American Chemical Society*, vol. 127, no. 8, pp. 2496–2504, 2005.

[146] J. J. Calvin, A. Ben-Moshe, E. B. Curling, A. S. Brewer, A. B. Sedlak, T. M. Kaufman, and A. P. Alivisatos, “Thermodynamics of the Adsorption of Cadmium Oleate to Cadmium Sulfide Quantum Dots and Implications of a Dynamic Ligand Shell,” *The Journal of Physical Chemistry C*, vol. 126, no. 30, pp. 12958–12971, 2022.

[147] O. Elimelech, O. Aviv, M. Oded, X. Peng, D. Harries, and U. Banin, “Entropy of Branching Out: Linear versus Branched Alkylthiols Ligands on CdSe Nanocrystals,” *ACS Nano*, vol. 16, no. 3, pp. 4308–4321, 2022.

[148] A. S. Brewer, J. J. Calvin, and A. P. Alivisatos, “Impact of Uniform Facets on the Thermodynamics of Ligand Exchanges on Colloidal Quantum Dots,” *The Journal of Physical Chemistry C*, vol. 127, no. 21, pp. 10270–10281, 2023.

[149] K. H. Kim, P. H. Dannenberg, H. Yan, S. Cho, and S. H. Yun, “Compact Quantum-Dot Microbeads with Sub-Nanometer Emission Linewidth,” *Advanced Functional Materials*, vol. 31, p. 2103413, 11 2021.

[150] Marcel J. E. Fischer, “Amine Coupling Through EDC/NHS: A Practical Approach,” in *Surface Plasmon Resonance: Methods and Protocols* (N. J. Mol and M. J. E. Fischer, eds.), vol. 627 of *Methods in Molecular Biology*, ch. Amine Coup, pp. 55–73, New Jersey: Humana Totowa, 1 ed., 2010.

[151] L. Zhu, H. Hao, C. Ding, H. Gan, S. Jiang, G. Zhang, J. Bi, S. Yan, and H. Hou, “A novel photoelectrochemical aptamer sensor based on cdte quantum dots enhancement and exonuclease I-assisted signal amplification for Listeria monocytogenes detection,” *Foods*, vol. 10, no. 12, pp. 11–13, 2021.

[152] Q. Zhang, R.-X. Li, X. Chen, X.-X. He, A.-L. Han, G.-Z. Fang, J.-F. Liu, and S. Wang, “Study of Efficiency of Coupling Peptides with Gold Nanoparticles,” *Chinese Journal of Analytical Chemistry*, vol. 45, pp. 662–667, 5 2017.

[153] J. Zhou, Y. Yang, and C.-y. Zhang, “Toward Biocompatible Semiconductor Quantum Dots: From Biosynthesis and Bioconjugation to Biomedical Application,” *Chemical Reviews*, vol. 115, no. 21, pp. 11669–11717, 2015.

[154] B. Cai, X. Yang, L. Sun, X. Fan, L. Li, H. Jin, Y. Wu, Z. Guan, L. Zhang, L. Zhang, and Z. Yang, “Stability and bioactivity of thrombin binding aptamers modified with D-/L-isothymidine in the loop regions,” *Organic & Biomolecular Chemistry*, vol. 12, no. 44, pp. 8866–8876, 2014.

[155] A. Iyer, A. Chandra, and R. Swaminathan, “Hydrolytic enzymes conjugated to quantum dots mostly retain whole catalytic activity,” *Biochimica et Biophysica Acta - General Subjects*, vol. 1840, no. 9, pp. 2935–2943, 2014.

[156] C. R. Taylor, S. R. Shi, N. J. Barr, and N. Wu, “Techniques of Immunohistochemistry: Principles, Pitfalls and Standardization,” in *Diagnostic Immunohistochemistry: Second Edition*, pp. 1–42, Elsevier, 2006.

[157] H. C. Kolb, M. G. Finn, and K. B. Sharpless, “Click Chemistry: Diverse Chemical Function from a Few Good Reactions,” *Angewandte Chemie International Edition*, vol. 40, no. 11, pp. 2004–2021, 2001.

[158] L. Taiariol, C. Chaix, C. Farre, and E. Moreau, “Click and Bioorthogonal Chemistry: The Future of Active Targeting of Nanoparticles for Nanomedicines?,” *Chemical Reviews*, vol. 122, no. 1, pp. 340–384, 2022.

[159] R. K. Iha, K. L. Wooley, A. M. Nyström, D. J. Burke, M. J. Kade, and C. J. Hawker, “Applications of Orthogonal “Click” Chemistries in the Synthesis of Functional Soft Materials,” *Chemical Reviews*, vol. 109, pp. 5620–5686, 11 2009.

[160] Y. Chen, J. M. Cordero, H. Wang, D. Franke, O. B. Achorn, F. S. Freyria, I. Coropceanu, H. Wei, O. Chen, D. J. Mooney, and M. G. Bawendi, “A Ligand System for the Flexible Functionalization of Quantum Dots via Click Chemistry,” *Angewandte Chemie - International Edition*, vol. 57, no. 17, pp. 4652–4656, 2018.

[161] G. Mao, Y. Ma, G. Wu, M. Du, S. Tian, S. Huang, X. Ji, and Z. He, "Novel Method of Clickable Quantum Dot Construction for Bioorthogonal Labeling," *Analytical Chemistry*, vol. 93, no. 2, pp. 777–783, 2021.

[162] A. Picard-Lafond and J. F. Morin, "Low-Temperature Synthesis of Carbon-Rich Nanoparticles with a Clickable Surface for Functionalization," *Langmuir*, vol. 33, no. 22, pp. 5385–5392, 2017.

[163] V. V. Breus, C. D. Heyes, and G. U. Nienhaus, "Quenching of CdSe-ZnS core-shell quantum dot luminescence by water-soluble thiolated ligands," *Journal of Physical Chemistry C*, vol. 111, no. 50, pp. 18589–18594, 2007.

[164] L. Martínez-Jothar, S. Doulkeridou, R. M. Schiffelers, J. Sastre Torano, S. Oliveira, C. F. van Nostrum, and W. E. Hennink, "Insights into maleimide-thiol conjugation chemistry: Conditions for efficient surface functionalization of nanoparticles for receptor targeting," *Journal of Controlled Release*, vol. 282, pp. 101–109, 2018.

[165] E. Giovanelli, E. Muro, G. Sitbon, M. Hanafi, T. Pons, B. Dubertret, and N. Lequeux, "Highly enhanced affinity of multidentate versus bidentate zwitterionic ligands for long-term quantum dot bioimaging," *Langmuir*, vol. 28, no. 43, pp. 15177–15184, 2012.

[166] M. Stanisavljevic, L. Janu, K. Smerkova, S. Krizkova, N. Pizurova, M. Ryvolova, V. Adam, J. Hubalek, and R. Kizek, "Study of streptavidin-modified quantum dots by capillary electrophoresis," *Chromatographia*, vol. 76, no. 7-8, pp. 335–343, 2013.

[167] X. Liu, J. Ren, L. Su, X. Gao, Y. Tang, T. Ma, L. Zhu, and J. Li, "Novel hybrid probe based on double recognition of aptamer-molecularly imprinted polymer grafted on upconversion nanoparticles for enrofloxacin sensing," *Biosensors and Bioelectronics*, vol. 87, pp. 203–208, 2017.

[168] G. Nunzi Conti, S. Berneschi, and S. Soria, "Aptasensors Based on Whispering Gallery Mode Resonators," *Biosensors*, vol. 6, no. 3, p. 28, 2016.

[169] A. Brown, J. Brill, R. Amini, C. Nurmi, and Y. Li, “Development of Better Aptamers: Structured Library Approaches, Selection Methods, and Chemical Modifications,” *Angewandte Chemie*, vol. 136, p. e202318665, 4 2024.

[170] I. Russo Krauss, A. Merlino, A. Randazzo, E. Novellino, L. Mazzarella, and F. Sica, “High-resolution structures of two complexes between thrombin and thrombin-binding aptamer shed light on the role of cations in the aptamer inhibitory activity,” *Nucleic Acids Research*, vol. 40, no. 16, pp. 8119–8128, 2012.

[171] W.-H. Chen, X. Yu, A. Cecconello, Y. S. Sohn, R. Nechushtai, and I. Willner, “Stimuli-responsive nucleic acid-functionalized metal–organic framework nanoparticles using pH- and metal-ion-dependent DNAzymes as locks,” *Chemical Science*, vol. 8, no. 8, pp. 5769–5780, 2017.

[172] Z. Chen, M. Sun, F. Luo, K. Xu, Z. Lin, and L. Zhang, “Stimulus-response click chemistry based aptamer-functionalized mesoporous silica nanoparticles for fluorescence detection of thrombin,” *Talanta*, vol. 178, pp. 563–568, 2018.

[173] E. Shoghi, S. Z. Mirahmadi-Zare, R. Ghasemi, M. Asghari, M. Poorebrahim, and M.-H. Nasr-Esfahani, “Nanosized aptameric cavities imprinted on the surface of magnetic nanoparticles for high-throughput protein recognition,” *Microchimica Acta*, vol. 185, no. 4, p. 241, 2018.

[174] Y. Liu, W. Hou, H. Sun, C. Cui, L. Zhang, Y. Jiang, Y. Wu, Y. Wang, J. Li, B. S. Sumerlin, Q. Liu, and W. Tan, “Thiol–ene click chemistry: a biocompatible way for orthogonal bioconjugation of colloidal nanoparticles,” *Chemical Science*, vol. 8, no. 9, pp. 6182–6187, 2017.

Chapter 2

Materials and Methods

2.1 Introduction

This chapter is a description of all of the chemical materials used in the fabrication of SPs and their surface functionalisation, along with the different methods of fabrication and surface alterations used for this research. The method of optical characterisation of SPs before and after functionalisation and the method for estimating the laser threshold of SPs is also detailed. Finally, the optical setup built for the biosensing tests, along with the method used, is also described.

2.2 Materials

$CdSe_{1-x}S_x/ZnS$ alloyed core/shell quantum dots (CQDs) emitting at 575 nm and 630 nm were purchased from Cytodiagnostics and CD Bioparticles, respectively. These CQDs are designed to have a diameter of 6 nm and the optical properties are tuned by the alloy composition. Poly(vinyl alcohol) (Mw 13,000 - 23,000, 87-89% hydrolysed), sorbitan monolaurate (Span 20), Sodium Dodecyl Sulfate (SDS), Hydroxyethyl cellulose (HEC), 3-mercaptopropionic acid (MPA), Dimethylformamide (DMF), hexane, *N*-Hydroxysuccinimide (NHS), *N*-(3-Dimethyl

aminopropyl)-*N'*-ethyl carbodiimide hydrochloride (EDC), Thrombin, Bovine Serum Albumin (BSA), Polyvinylpyrrolidone (PVP), tetroethyl orthosilicate (TEOS), and Ammonia (2 M in ethanol) were purchased from Sigma Aldrich. Polyoxyethylene (20) sorbitan monolaurate (Tween 20) and Neutravidin were purchased from Fischer Scientific. Thrombin Binding Aptamer with 15 bases (TBA-15) was purchased from Integrated DNA Technologies with the sequence 5'-NH-GGT TGG TGT GGT TGG -3' where NH is a 6-carbon amino linker. Unless specified, all materials were used without purification or drying.

2.3 Synthesis of CQD Supraparticles

2.3.1 Standard Emulsion Method

Procedure was adapted from literature [1, 2] and carried out under ambient conditions. A 20 mg/mL solution of CQDs was prepared in chloroform. 100 µL of this solution was added to 450 µL of a 2.5 w% solution of poly(vinyl alcohol) (PVA) in deionised water and stirred vigorously for up to 6 h. Where SDS was used instead of PVA, the concentration of the solution used was 6 mg/mL. The time required for complete evaporation of the chloroform oil phase was not consistent, therefore constant monitoring of the emulsion was required after the first 2 h of stirring. The reaction mixture was centrifuged at 8,000 rpm for 10 minutes, the supernatant discarded, the resulting pellet was resuspended in DI water, and stored at 4 °C.

2.3.2 Three-surfactant Method

Procedure was adapted from literature [3] and carried out under ambient conditions. A 160 mg/mL solution of CQDs was prepared in cyclohexane for the oil phase. This method requires slower stirring speeds and used a lower volume of CQD phase, therefore a solvent with a higher boiling point that chloroform was required. A higher concentration of CQDs was used to follow the literature procedure. For the water phase, a solution of DI water with 199 mmol Tween 20, 4.65 mmol Span 20, 18.6 mmol SDS, and 25 µmol HEC was prepared. 50 µL of CQD solution was added to 750 µL of water phase and stirred at 230 rpm for 2 h to emulsify. After emulsification, the solution was left stirring at 60 rpm for 20 hours to evaporate the cyclohexane. The mixture was centrifuged at 5,000 rpm for 10 minutes, the supernatant discarded, and the resulting pellet was resuspended in a 20 mmol Tween 20 solution.

2.3.3 Surfactant-free Method

Procedure was adapted from literature [4] and carried out under ambient conditions. A 20 mg/mL solution of CQDs in hexane was prepared. 25 µL of CQD solution was added to 100 µL of DMF and vortexed. The emulsion was left standing for 20 minutes until the hexane had evaporated.

2.3.4 Characterisation

Microsphere size distributions were measured with ImageJ software using images taken from an optical microscope equipped with a Thorlabs^{TM} camera. Before samples were pipetted on slides for imaging, 1 µL of SP solution was diluted in 10 µL water. SEM images were captured using a JEOL JSM-IT100 operated at 20 kV.

2.4 Surface Functionalisation of Supraparticles

2.4.1 Silica Shell Growth

Procedure was adapted from literature. [5,6] Oleic acid coated SPs were redispersed in 250 µL 70:30 ethanol/H_2O mix. 80 µL of the SP solution was mixed with 20 µL of a 10 mg/mL PVP solution and sonicated for 20 minutes. This was repeated twice. The reaction mixture was then centrifuged at 10,000 rpm for 10 minutes, the supernatant discarded, and the SPs redispersed in 300 µL ethanol. 6.6 µL of TEOS was added, the reaction mixture was sonicated for 20 minutes, then 20 µL H_2O and ammonia added and sonicated for 1 h. After sonication, the mixture was centrifuged at 6,000 rpm for 10 minutes, the supernatant was removed and the final silica coated SPs were redispersed in H_2O.

2.4.2 Ligand Exchange with MPA

Procedure was adapted from literature to make it suitable for SPs instead of CQDs alone. [7,8] 200 µL oleic acid-capped SPs were re-dispersed in 500 µL 3:1 H_2O/EtOH mix. Excess MPA (500 µL) was added and the solution was stirred at room temperature overnight. The reaction mixture was centrifuged at 8,000 rpm for 10 minutes and the resulting pellet was washed with ethanol three times to remove unbound MPA. The resulting MPA-SPs were redispersed in water and stored at 4°C.

2.4.3 Neutravidin Functionalisation

Procedure was adapted from literature. [9, 10] 200 µL of MPA-SPs were dissolved in 500 µL DI water and 20 µL of a 5 mg/mL Neutravidin solution was added. The pH of the solution was adjusted to 7-8 using 25 mM NaOH and left to stir at 450 rpm for 1 hour. The reaction mixture was centrifuged at 8,000 rpm for 10 minutes, the supernatant discarded, and the Neutravidin capped-SPs were redispersed in DI water and stored at 4 °C.

2.4.4 DNA Aptamer Functionalisation

Procedure was adapted from literature. [11, 12]. 200 µL of MPA-SPs were activated by the addition of 30 µL of 40 mM EDC and 30 µL of 15 mM NHS with NaOH (10 mM in H_2O) added to increase the pH of the reaction to between 6.5 and 7 before leaving the mixture to stir for 1 h. Then, 20 µL of 10 µm TBA-15 solution was added and the solution was left stirring for 4 h with the pH of the reaction mixture maintained by the addition of 1-2 µL of 10 mM NaOH every 20 minutes.

2.4.5 Characterisation

SP size distributions were measured with ImageJ software using images taken from an optical microscope equipped with a Thorlabs^{TM} camera. SEM images were captured using a JEOL JSM-IT100 operated at 20 kV. Successful surface functionalisation was determined using a Malvern Zeta Potentiometer and Fourier Transform Infrared Spectroscopy (FTIR) using a Nicolet iS5 FTIR Spectrometer.

2.5 Optical Characterisation

2.5.1 Optical Pumping Setup

Single SPs were pumped using a 355 nm, 5 ns pulsed Nd:YAG laser at a 10 Hz repetition rate with a beam spot area of 2.6 $\times 10^{-5}$ cm^2. The beam was focused on the sample using a 10x magnification 0.25 mm × 160 mm microscope objective lens (MO) onto a stage which could be moved in the xyz planes to be able to find single SPs to analyse. To be able to image lasing SPs, the light from the lamp (Tungsten-Halogen) is directed though a 50:50 beamsplitter (BS) to direct the light to a CCD camera (DCC1645C, Thorlabs) and to the sample stage. Light from the pump laser, the SP sample and the lamp is directed to the sample stage and to the optical fibre using a dichroic mirror (DM), a flippable mirror (M3), a long pass filter to filter out remaining pump laser light (LP) and a lens with a focal length of 50 mm (L4). An Avantes AvaSpec-2048-4-DT spectrometer coupled to an optical fibre with a 50 µm diameter core was used to acquire spectral data at a resolution of 0.6 nm between 200-1100 nm. A schematic of this setup can be seen below in Fig 2.1.

2.5.2 Determination of Threshold

10 µL samples of SPs were drop cast on glass slides and left to dry. A variable wheel neutral density attenuator was used to alter the intensity of the pump laser beam and the photoluminescence spectrum of the SP laser was measured at every 10 degrees on the ND filter. The integrated emission intensity of the lasing or PL peak at each beam intensity was measured from the spectra and plotted against the beam fluence. This produced a laser transfer function plot with two distinct sections of data corresponding to PL intensity above and below threshold that can be fitted linearly. Laser threshold could then be estimated at the intersection of the two lines. The error for the laser threshold measurements were calculated using the propagation of error, taking into account errors from the measured beam spot size and pump energies, with Fl being

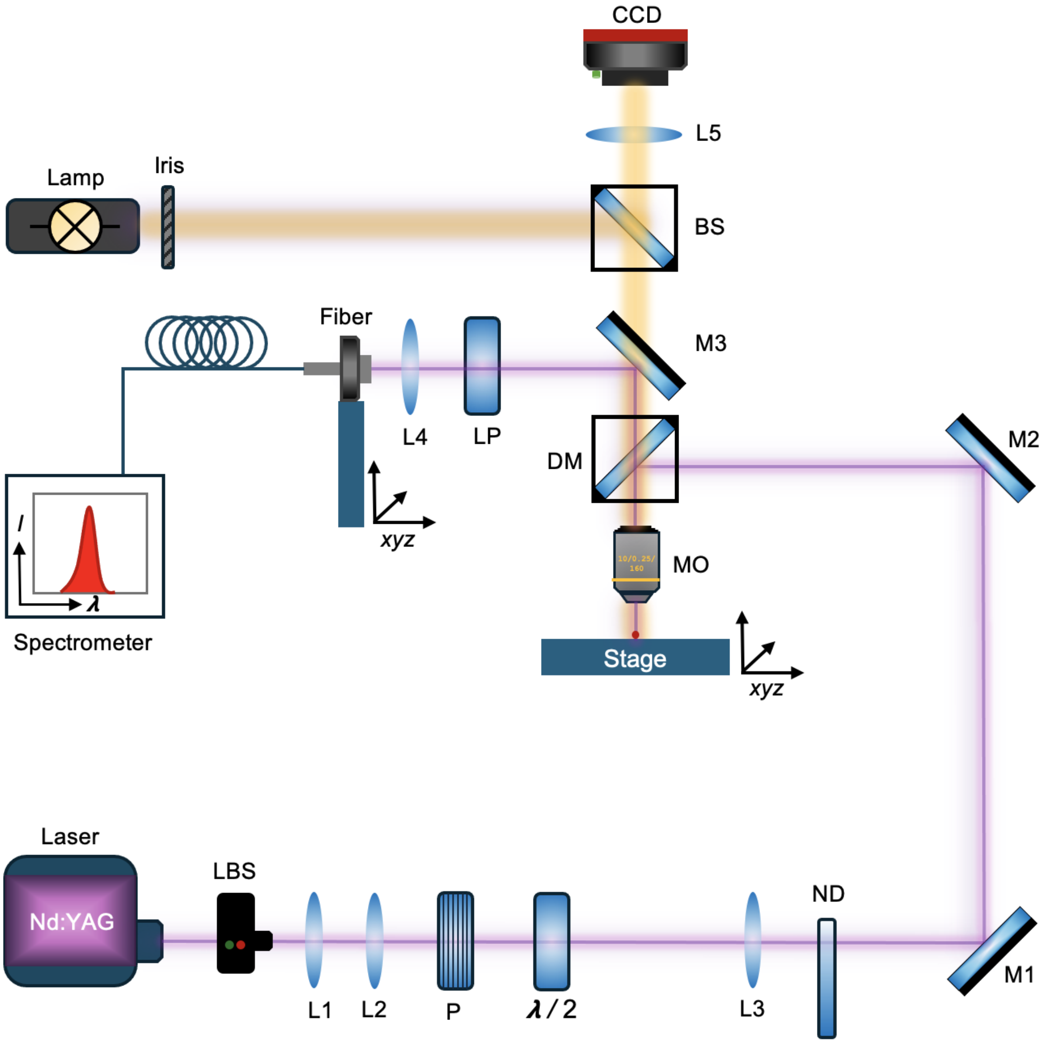

Figure 2.1: Illustration of the optical setup used for optical characterisation of supra-particles. The purple line represents the beam path of the pump laser and the sample stage and the yellow line represents light from the lamp. LBS is the laser beam stop, L1-5 are plano-convex lenses to manipulate and direct the beam from the laser. P is the polariser (GL 10-A, Thorlabs), $\lambda/2$ is the half waveplate, and ND is the neutral density filter used to attenuate the laser energy. M1-3 are the flippable mirrors used to direct the pump laser beam and SP samples. The optical fibre was mounted onto an xyz stage to improve the signal acquisition.

the measured threshold fluence:

$$\delta_{Fl} = Fl\sqrt{\left(\frac{\delta_E}{E}\right)^2 + \left(\frac{\delta_{w0}}{w_0}\right)^2} \tag{2.1}$$

Q factor is used to estimate the quality of the laser cavity which can be calculated using the simple expression: $Q = \frac{\lambda}{\Delta\lambda}$, where λ is the centre wavelength of the resonant mode and $\Delta\lambda$ is the FWHM of the resonant peak. To get a more accurate estimate of cavity quality, the Q-factor is typically calculated for PL emission below threshold.

2.6 Biosensing

2.6.1 Optical Setup

SP samples were prepared as described above and pumped with the same Nd:YAG laser operating at 355 nm with a pulse duration of 5 ns and a 10 kHz repetition rate. The same setup of the LBS, L1-3, polariser and half waveplate prior to the ND filter shown in Fig.2.1 was used in this setup. SP samples were mounted on an horizontal stage and the pump beam was directed onto the sample with a periscope and a dichroic mirror, then focused with a 10x magnification 0.25 mm × 160 mm objective lens. The light from the SP sample was directed through a lens with a focal length of 50 mm and through a long pass filter to filter out any remaining pump laser light. An optical fibre with a 50 µm diameter core coupled to a Avantes AvaSpec-2048-4-DT spectrometer with a spectral resolution of 0.1 nm between 420-655 nm was used to acquire spectral

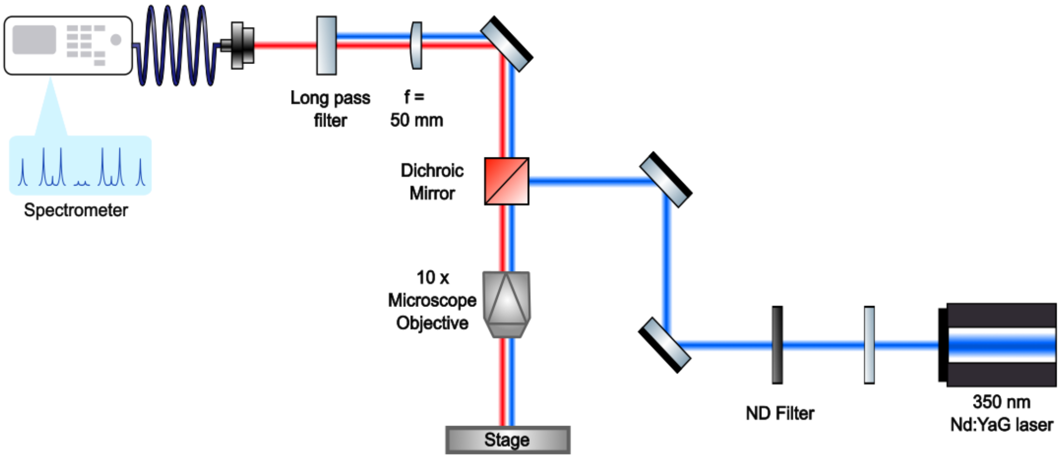

Figure 2.2: Illustration of the optical setup used in this biosensing procedure. The blue line represents the beam path of the pump laser and the red line represents the beam path of the laser signal from the SP sample.

data. An illustration of this optical setup can be seen in Fig. 2.2.

2.6.2 Procedure

Solutions of BSA and Thrombin were prepared in water with concentrations of 1.5, 5, 10, and 15 mg/mL to test the detection limit of the SP lasers. A lasing SP was found on the setup while immersed in water, 50 µL of protein solution was cast onto the sample, and the PL spectrum measured every five minutes until thrombin addition, in which case spectra were often taken every minute for periods of up to 110 minutes. BSA solutions were tested first then the Thrombin solution was added to test the amount of non-specific binding present. After the first sensing attempt, water was added when needed to stop the solutions from drying entirely. The wavelength shift over time was measured from the wavelength shift of the highest intensity lasing peak measured from the PL spectra over time for each concentration of protein.

2.7 Conclusion

In summary, the materials used for the SP fabrication and surface alterations have been detailed and the corresponding methods used to produce SPs with Neutravidin and Thrombin attached to the surface have been described. In addition to this, the optical setups used in the characterisation and biosensing tests of these SPs have been described, along with the methods of optical and chemical characterisation used to obtain the data discussed in the rest of this thesis.

References

[1] F. Montanarella, D. Urbonas, L. Chadwick, P. G. Moerman, P. J. Baesjou, R. F. Mahrt, A. van Blaaderen, T. Stöferle, and D. Vanmaekelbergh, “Lasing Supraparticles Self-Assembled from Nanocrystals,” *ACS Nano*, vol. 12, no. 12, pp. 12788–12794, 2018.

[2] P. U. Alves, N. Laurand, and M. D. Dawson, “Multicolor laser oscillation in a single self-assembled colloidal quantum dot microsphere,” in *2020 IEEE Photonics Conference (IPC)*, pp. 1–2, IEEE, 2020.

[3] A. Plunkett, C. Eldridge, G. A. Schneider, and B. Domènech, “Controlling the Large-Scale Fabrication of Supraparticles,” *The Journal of Physical Chemistry B*, vol. 124, no. 49, pp. 11263–11272, 2020.

[4] W. Chen, L. Wang, R. Liu, H. Shen, J. Du, and F. Fan, “Self-Assembled and Wavelength-Tunable Quantum Dot Whispering-Gallery-Mode Lasers for Backlight Displays,” *Nano Letters*, vol. 23, no. 2, pp. 437–443, 2023.

[5] C. J. Eling, N. Laurand, N.-K. Gunasekar, P. R. Edwards, and R. W. Martin, “Silica Coated Colloidal Semiconductor Quantum Dot Supracrystal Microlasers,” in *2022 IEEE Photonics Conference (IPC)*, pp. 1–2, IEEE, 2022.

[6] M. Fujii, R. Fujii, M. Takada, and H. Sugimoto, “Silicon Quantum Dot Supraparticles for Fluorescence Bioimaging,” *ACS Applied Nano Materials*, vol. 3, no. 6, pp. 6099–6107, 2020.

[7] N. T. Vo, H. D. Ngo, N. P. Do Thi, K. P. Nguyen Thi, A. P. Duong, and V. Lam, “Stability Investigation of Ligand-Exchanged CdSe/ZnS-Y (Y = 3-Mercaptopropionic Acid or Mercaptosuccinic Acid) through Zeta Potential Measurements,” *Journal of Nanomaterials*, vol. 2016, pp. 1–8, 2016.

[8] S. A. Rahman, N. Ariffin, N. A. Yusof, J. Abdullah, F. Mohammad, Z. A. Zubir, and N. M. A. N. A. Aziz, “Thiolate-capped CdSe/ZnS core-shell quantum dots for the sensitive detection of glucose,” *Sensors (Switzerland)*, vol. 17, no. 7, pp. 1–12, 2017.

[9] M. Bäumle, D. Stamou, J.-M. Segura, R. Hovius, and H. Vogel, “Highly Fluorescent Streptavidin-Coated CdSe Nanoparticles: Preparation in Water, Characterization, and Micropatterning,” *Langmuir*, vol. 20, no. 10, pp. 3828–3831, 2004.

[10] M. Stanisavljevic, L. Janu, K. Smerkova, S. Krizkova, N. Pizurova, M. Ryvolova, V. Adam, J. Hubalek, and R. Kizek, “Study of streptavidin-modified quantum dots by capillary electrophoresis,” *Chromatographia*, vol. 76, no. 7-8, pp. 335–343, 2013.

[11] Y. H. Lao, C. W. Chi, S. M. Friedrich, K. Peck, T. H. Wang, K. W. Leong, and L. C. Chen, “Signal-on Protein Detection via Dye Translocation between Aptamer and Quantum Dot,” *ACS Applied Materials and Interfaces*, vol. 8, no. 19, pp. 12048–12055, 2016.

[12] L. Zhu, H. Hao, C. Ding, H. Gan, S. Jiang, G. Zhang, J. Bi, S. Yan, and H. Hou, “A novel photoelectrochemical aptamer sensor based on cdte quantum dots enhancement and exonuclease I-assisted signal amplification for Listeria monocytogenes detection,” *Foods*, vol. 10, no. 12, pp. 11–13, 2021.

Chapter 3

Fabrication of Self-Assembled Lasers

3.1 Overview

Ampiphilic molecules called surfactants have been used to stabilise emulsions for a myriad of applications over a span of decades. Here, we use an emulsion method to fabricate microspheres consisting entirely of colloidal quantum dots (CQDs) to be used as lasers. In summary, CQDs coated in organic ligands are dissolved in organic solvent and emulsified in water containing the surfactant poly(vinyl alcohol) and the organic solvent is left to evaporate which causes CQDs to self-assemble into spherical supraparticles (SPs). The choice of surfactant has a marked effect on the SPs fabricated and in this work two additional methods are trialled using a mixture of three surfactants and no surfactant at all to test whether the physical and optical properties of SPs can be improved upon.

3.2 Emulsion Methods

3.2.1 Standard Emulsion Method

SPs were fabricated according to the emulsion method detailed above and within literature. [1, 2] The emulsion method was carried out with both PVA and SDS surfactants with chloroform used for the oil phase solvent. Chloroform was chosen as the solvent due to its low boiling point and interfacial tension allowing for more high quality crystal structures without increasing the reaction time. [3] Alloyed core/shell $CdSe_{1-x}S_x/ZnS$ quantum dots with an average size of 5.5-6.5 nm emitting at 575 nm and 630 nm were used. These CQDs are coated in oleic acid ligands, a molecule with a long 18-carbon chain with C=C double bond in the centre and a carboxylic acid group at one end which binds to the surface of CQDs. Due to this chemical structure, the CQDs coated in these ligands are insoluble in water which is vital for using this standard emulsion method. The evaporation time of these reactions could still vary from 2-6 h depending on the environmental conditions such as humidity and temperature. Due to the inconsistency in the evaporation time, the emulsion required close monitoring via optical microscopy. Often within literature, microfluidic chips are used for droplet generation to reduce polydispersity of the SPs produced, however this step was simplified by vortexing the reaction mixture to generate the emulsion instead. Figure 3.1a is the size distributions of SPs made with the two different types of quantum dot and two different surfactants, PVA and SDS, which demonstrates the high polydispersity of SPs assembled without using a microfluidic cell for droplet generation. Figure 3.1b is a plot

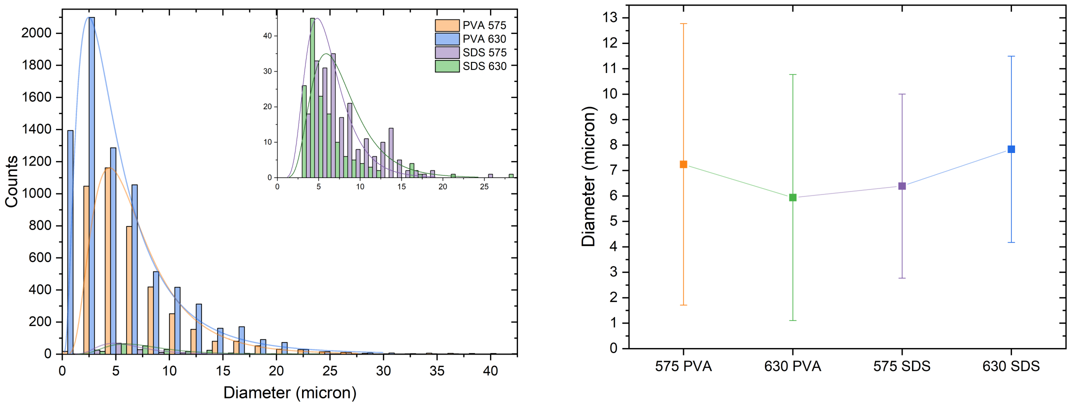

Figure 3.1: (a) Size distributions of SPs produced using the emulsion method with PVA and SDS and with the two different types of CQDs. Inset is a zoomed in portion of the distributions showing SPs produced using SDS. For the distributions, lognormal fits were used. (b) Average diameters of the SP samples shown in (a). Error bars represent the standard deviations and the line between each point is a guide for the eye to show the different in average diameter values more clearly.

of the average diameters of the samples shown in Fig. 3.1a. SP diameters can be an indication of the stability of the emulsion towards breakdown and therefore the quality of SPs produced. In this case, PVA-SPs made with 575 nm and 630 nm CQDs had average diameters of 7.2 ± 5.5 and 5.9 ± 4.8 µm respectively. For SDS-SPs made with 575 nm and 630 nm CQDs the average diameters were found to be 6.4 ± 3.6 and 7.8 ± 3.7 µm respectively. Analysis of variance (ANOVA) statistical analysis was carried out on the size measurements of the SPs and found that the average diameters of the two samples are statistically significant, indicating that the two types of CQDs used affect the size of the resulting SPs. Both types of CQDs used are commercially available and the stated size distributions of the 575 nm and 630 nm CQDs are both 5.5 - 6.5 nm, which means this would not be a factor affecting the SPs produced. Diameters of SPs produced with SDS and PVA can also be compared with ANOVA. The 630 nm PVA and SDS SPs with average diameters of 5.9 ± 4.8 and 7.8 ± 3.7 µm respectively were found to be statistically significant which would be expected due to the importance of surfactant choice on emulsion-templated self assembly. The average diameters of the 575 nm SPs made with PVA and SDS had average diameters of 7.2 ± 5.5 and 6.4 ± 3.6 µm respectively, however these averages were shown to be statistically insignificant using ANOVA. Figure 3.5b demonstrates the similarity in the average diameter values across SP samples. Although these data indicate similarities in the SPs produced, when it came to attempting to alter the surface of the SPs for biosensing applications, SDS-SPs were not found to be stable towards further solution processing hence the focus moving forwards remained on SPs produced using PVA as the surfactant (for full information see Chapter 4). This could be due to van der Waals' forces between the hydrophobic chains of the PVA and the oleic acid ligands contributing to higher stability towards dissolution of the SPs back into CQDs. [4]

3.2.2 Other Emulsion Methods

Two other emulsion methods were trialled with the standard method to test whether it was possible to improve on the SPs produced using the standard emulsion method. The first synthesis trialled was the 3-surfactant (3S) method detailed within literature.

[5] In summary, this method uses a 160 mg/mL CQD solution in cyclohexane as the oil phase due to its higher boiling point than chloroform, which is a favourable factor for emulsion templated self-assembly. [3] For the water phase, a solution with a mixture of SDS, polyoxyethylene (20) sobitan monolaurate (Tween 20), sorbitan monolaurate (Span 20), and a thickener, Hydroxyethyl cellulose (HEC), was made to be able to control the hydrophilic-lipophilic balance (HLB) of the emulsion and therefore the resulting SPs. The ratio of oil/water phase of the emulsion in this method was 1:15. The HLB value of the surfactants solution with the concentrations used in this work was calculated to be 18.5. In comparison, the HLB of SDS alone is 40 [5], as it is an ionic surfactant, and the HLB of PVA is 18. [6] This implied the 3S synthesis would produce similar SPs to those produced using the standard emulsion method. Emulsification was carried out by stirring at a low rpm for 2 hours due to the viscosity of the water phase and the evaporation phase required stirring at only 60 rpm for 18 hours due to the higher boiling point of cyclohexane (80 °C) compared to chloroform (61 °C). The other emulsion method that was trialled was a surfactant-frexle (SF) synthesis found in the literature. [7] In this method, the oil phase consisted of a 20 mg/mL solution of CQDs in hexane and the water phase was dimethylformamide (DMF) and the oil/water phase ratio was 1:4. The emulsification was carried out by vortexing for

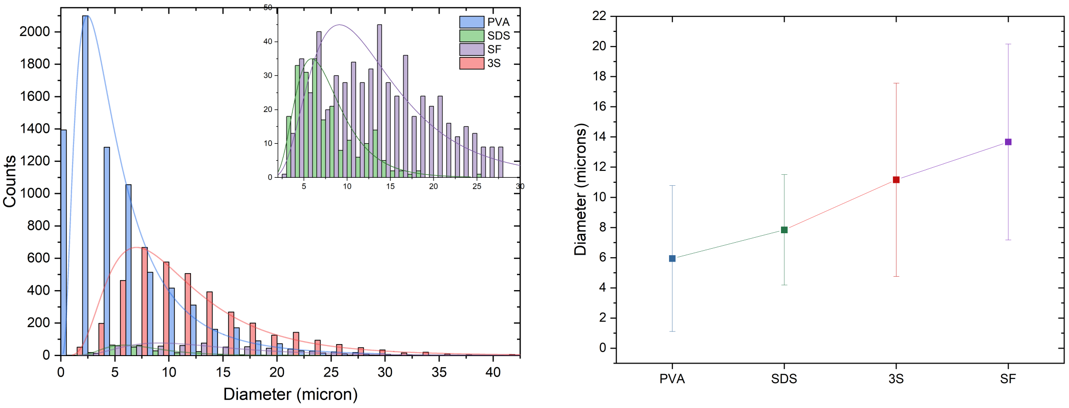

Figure 3.2: (a) Size distributions of SPs produced using the emulsion method with PVA and SDS, the three-surfactant, and the surfactant-free method. Inset is a zoomed in portion of the distributions showing SPs produced using SDS and the SF method. (b) Average diameters of the SP samples shown in (a).

approximately 30-60s and the evaporation stage was complete within 20 minutes due to the small scale on which this synthesis had to be carried out. Scaling up the assembly was attempted, however the best results were produced using the small scale with a total emulsion volume of 125 µL. In comparison, the PVA and 3S methods had total emulsion volumes of 550 µL and 800 µL respectively. The reason this emulsion can work without surfactants is due to the interfacial tension between DMF and hexane which is 21.7 mN/m. [8]

Figure 3.2 shows the size distributions and average diameters of SPs produced using the three different emulsion methods along with an SDS-SP sample. In all of these samples, the 630 nm emitting CQDs were used. The average diameters of 3S-SPs and SF-SPs were larger than the two samples produced using the standard method at 11.2 ± 6.4 µm and 13.7 ± 6.5 µm respectively. ANOVA also demonstrated that average diameters of all the SP samples, PVA-, SDS-, 3S-, and SF-SPs, were statistically different from each other. The larger average diameters demonstrated in the 3S-SP sample may be due to the solution of CQDs used being 8x higher in concentration than that used in the standard one-emulsion method, however the literature detailing the 3S method suggests that CQD concentration does not impact the size of SPs produced using this method. [5] Larger SPs produced could also be due to the emulsification process. As detailed above, emulsification of the 3S synthesis is done over a longer period and lower stirring speeds, or shear rate, which would produce larger emulsion droplets compared to the other methods where droplet formation is achieved by vortexing the mixture which has a higher shear rate. [9, 10] SF-SPs also demonstrate a much larger average SP size which could be due to the lack of surfactant making the emulsion less stable to droplet coalescence, which can be seen in the SEM images in Figure 3.3 where there are a lot more amorphous and large structures in the sample produced. The size distribution shown in Figure 3.2a also shows a much lower yield of SPs from the SF method and, as mentioned earlier, this will be mainly due to the reaction requiring a smaller scale to be successful. This method was also found not to be consistently repeatable, with two samples prepared at the same time producing one batch of suitable SPs and the other consisting entirely of amorphous structures and could not be used. Figure

3.3 shows SEM images of the wider sample and single SPs assembled using the PVA, 3S, and SF methods. Figures 3.3e shows the amorphous and large structures produced in the SF method, which is much more noticeable than those that are produced in the other two samples, indicating the possibility that the lack of surfactant reduces the emulsion stability towards droplet coalescence. However, in the images of the single SPs, the SF-SP pictured in Figure 3.3f has a much smoother surface than the PVA-

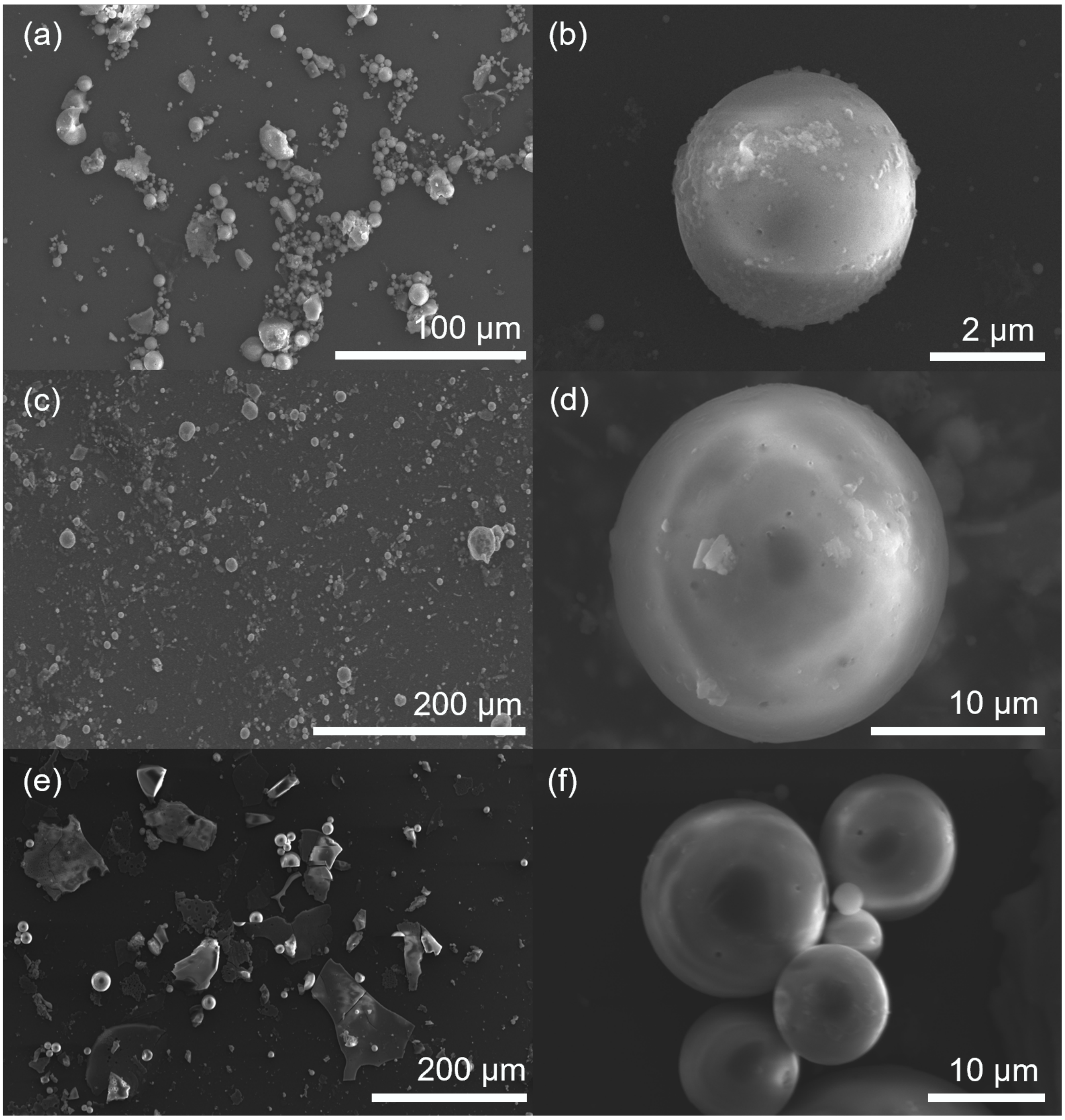

Figure 3.3: SEM images of whole samples and single SPs made using the different emulsion methods. (a) and (b) are PVA-SPs, (c) and (d) are 3S-SPs, and (e) and (f) are SF-SPs.

and 3S-SPs above in 3.3b and d respectively. This could be due to the way the surfactants present in the emulsion would arrange themselves at the droplet interface to lower the interfacial tension. As the solvent continues to evaporate in the emulsion, the hydrophobic chains of the surfactant would stay within the CQDs in the assembling SPs, therefore resulting in surfactants being packed within CQDs with the hydrophilic sections of the surfactants at the SP surface. [4, 11] Surfactants being on the surface has an impact when attempting to alter the surface of the SPs which is detailed further in Chapter 4.

3.3 Optical Measurements

As described in Chapter 1, due to the high refractive index of the CQDs compared to the surrounding environment, light can be captured and contained within the SPs through total internal reflection where the light cycles around the cavity equator and can interfere constructively to produce whispering gallery modes (WGM). In this case, a single SP contains both the cavity and the gain medium to produce lasing through these whispering gallery modes. The lasing ability of these SPs is therefore tightly linked to the quality of the SPs, as this determines the cavity quality of the lasers. Surface smoothness therefore also plays an important role in being able to achieve lasing. SPs were pumped with a 350 nm Nd:YaG laser with a ND filter used to control the incident fluence, a setup schematic is shown in Figure 2.1. Figure 3.4a shows the photoluminescence (PL) spectra of single SPs pumped above and below threshold and 3.4b is the laser transfer function (LTF) plots of the emission intensity integrated under the laser peak against the pump fluence, used to estimate the threshold of the SP lasers. Average thresholds of all of the SPs tested were found to be 20.1 ± 13.9, 9.2 ± 3.5, and 18.5 ± 12.3 mJ/cm^2 for PVA-, 3S-, and SF-SPs respectively. It should be noted that the pump spot size is 2.6 $\times 10^{-5}$ cm^2 therefore only SPs with diameters of at least 28.5 µm will interact with all of the incident pump energy, which is only the case for two 3S-SPs with measured diameters of 29.6 and 36.6 µm. This size mismatch means that not all of the pump laser light is absorbed by the single SP, therefore the threshold values reported will be higher than the SPs could achieve. [12] ANOVA shows that

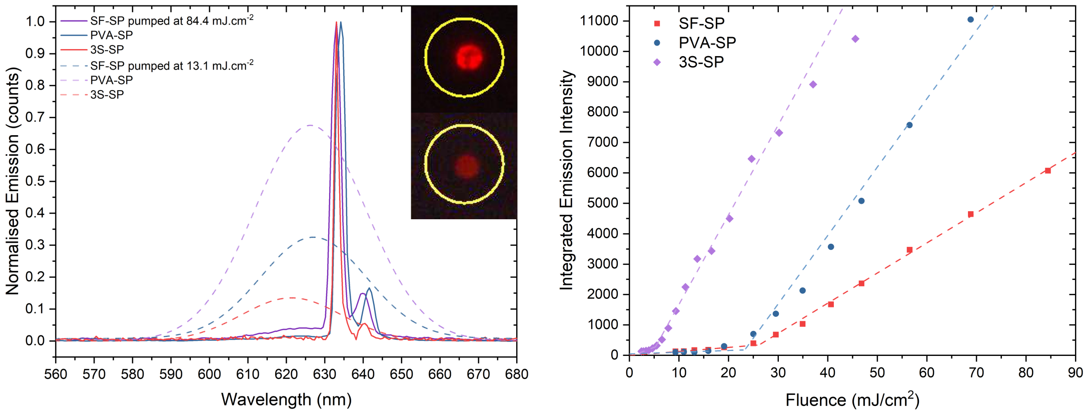

Figure 3.4: (a) Photoluminescence Spectra of single PVA-, 3S- and SF-SPs pumped above and below threshold. Spectra were normalised to the maximum signal and were not used for the threshold calculations. The diameters of the SPs shown are 9.1 µm, 7.7 µm, and 9.1 µm for the PVA-, 3S- and SF-SP, respectively. Inset shows the PVA-SP pumped above (top) and below (bottom) threshold, captured on the CCD camera. The yellow circle was used to approximate the position of the pump laser on the sample. (b) Laser transfer function plots of the SPs in (a) used to estimate the laser threshold fluences. The thresholds of the SPs shown were 23.3 ± 3.2, 4.7 ± 0.6, and 26.1 ± 3.6 mJ/cm^2 for PVA-, 3S-, and SF-SPs respectively.

there is no statistically significant differences between these average threshold values, implying that the assembly method used does not impact the optical characteristics as much as first thought. However, it is also important to note that the method for optically characterising these SPs requires the 'selection' of each individual SP in the sample, therefore the measurements are often the best representatives of the wider sample. The related box plots showing the laser diameters and thresholds found for all lasing SPs found in PVA-, 3S-, and SF-OA samples are shown in Figure 3.5. There are a myriad of factors that can affect the optical properties of WGM lasers, such as the surrounding environment, cavity quality and the size of the cavity. [13] The size of the cavity is particularly important as cavities which are too small are unable to confine light as effectively, resulting in lossy cavities and higher thresholds. [14] Therefore, the diameter of the lasing SPs was also measured and the average laser diameters were found to be 9.3 ± 3.2, 20.3 ± 8.8, and 13.3 ± 5.4 µm for PVA-, 3S-, and SF-SPs respectively. The statistically significant average diameter was that of the 3S-SPs compared to PVA- and SF-SPs. As stated above, larger cavities can lead to improved light confinement

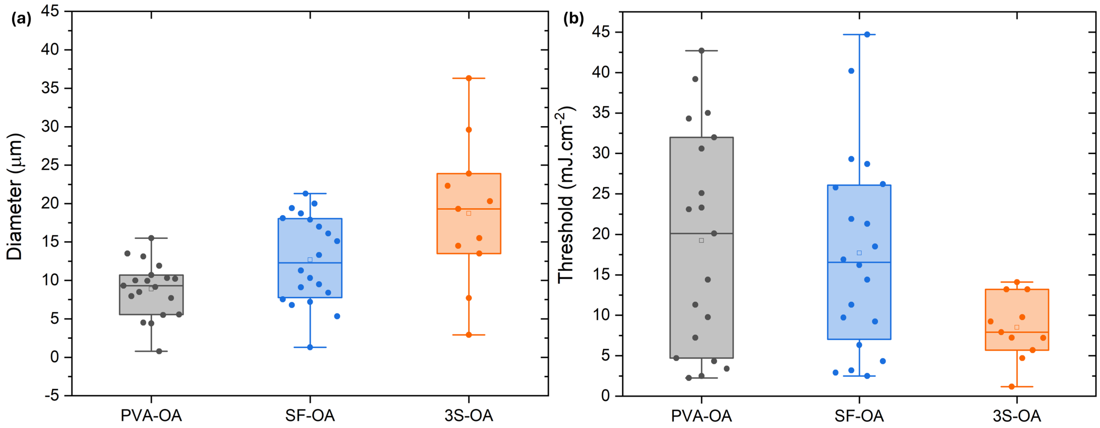

Figure 3.5: (a) Box plot showing the laser diameters of all SP lasers found in PVA-, SF-, and 3S-OA samples. The average laser diameters were 9.3 ± 3.2 µm, 13.3 ± 5.4 µm, and 20.3 ± 8.8 µm for PVA-, SF-, and 3S-OA-SPs respectively. (b) Box plots showing the corresponding laser thresholds of all SP lasers found in PVA-, SF-, and 3S-OA-SP samples tested. Average thresholds were estimated to be 20.1 ± 13.9 mJ/cm^2, 18.5 ± 12.3 mJ/cm^2, and 9.2 ± 3.5 mJ/cm^2 for the PVA-, SF-, and 3S-OA-SPs respectively. A full list of the measurements is in Appendix A.1, Table A.1.

within the SPs, therefore the large average diameter of 3S-SP lasers could be the factor leading to the low average laser threshold observed. The higher concentration of CQD solution used in the 3S method could also lead to more densely packed SPs which could also contribute to lower thresholds.

3.4 Conclusion

In summary, three different variants of emulsion templated self-assembly methods were trialled for the synthesis of SPs. For the standard emulsion method, two different surfactants were used along with two different wavelength emissions of CQDs. The average diameters of SPs synthesised were compared to assess the results of each method. The type of CQD used seemed to affect the average diameter of SPs even though polydispersity and size of the CQDs was in a similar range for both solutions and would not affect the properties of the emulsion. There are many other reasons that could be behind this somewhat unexpected observation including slight solution concentration changes, temperature, and humidity fluctuations between each SP fabrication. Altering the surfactant used in the standard emulsion method demonstrated a change in the average diameter of produced SPs, which was expected. Comparing the HLB values of the two surfactants used, SDS and PVA, does not explain the increased average diameter of SPs seen between PVA- and SDS-SPs as a higher HLB value surfactant is expected to create smaller emulsion droplets and, by extension, SPs. [5] When it came to attempts at further functionalisation, it was found that PVA-SPs were much more stable towards chemical reactions and solution processing than SDS-SPs, making PVA-SPs more suitable moving forward to biosensing applications. PVA-SPs made with CQDs emitting at 630 nm were compared with SPs made from two other emulsion methods, three-surfactant (3S) and surfactant-free (SF). Both new emulsion methods were found to produce larger SPs, which was possibly due to emulsification being carried out at a lower shear rate for 3S-SPs and the lack of surfactant reducing stability towards droplet coalescence for SF-SPs. SEM images of samples and single SPs were also compared between the three assembly methods which demonstrated PVA- and 3S-SPs have rougher surfaces compared to SF-SPs, which was attributed to surfactants being present at the oil/water interface and the hydrophobic sections of the surfactants packing between the CQDs during the evaporation stage. Optical measurements of the SPs made with the different emulsion variants were taken to determine the effect, if any, the fabrication method has on the optical characteristics of the SP lasers. Average thresholds of SPs tested were estimated to be 20.1 ± 2.8, 9.2 ± 1.3 and 18.4 ± 3.5 mJ/cm^2 for PVA-, 3S- and SF-SPs respectively. The lower average threshold observed in 3S-SPs was attributed to the, on average, larger diameters of lasing 3S-SPs which can reduce losses in WGM cavities. [13] On top of that, there is a higher cross-section at the pump wavelength and therefore a higher absorption of pump photons could also be contributing to the lower threshold. [12] While the favourable optical characteristics observed in 3S-SPs would suggest the 3S method would be preferred for SPs, the stability towards further solution processing and surface functionalisation is even more important for assessing the suitability of the fabrication methods.

References

[1] F. Montanarella, D. Urbonas, L. Chadwick, P. G. Moerman, P. J. Baesjou, R. F. Mahrt, A. van Blaaderen, T. Stöferle, and D. Vanmaekelbergh, "Lasing Supraparticles Self-Assembled from Nanocrystals," *ACS Nano*, vol. 12, no. 12, pp. 12788–12794, 2018.

[2] C. J. Eling, N. Laurand, N.-K. Gunasekar, P. R. Edwards, and R. W. Martin, "Silica Coated Colloidal Semiconductor Quantum Dot Supracrystal Microlasers," in *2022 IEEE Photonics Conference (IPC)*, pp. 1–2, IEEE, 2022.

[3] E. Marino, A. W. Keller, D. An, S. van Dongen, T. E. Kodger, K. E. MacArthur, M. Heggen, C. R. Kagan, C. B. Murray, and P. Schall, "Favoring the Growth of High-Quality, Three-Dimensional Supercrystals of Nanocrystals," *The Journal of Physical Chemistry C*, vol. 124, no. 20, pp. 11256–11264, 2020.

[4] J. Wang, E. Kang, U. Sultan, B. Merle, A. Inayat, B. Graczykowski, G. Fytas, and N. Vogel, "Influence of Surfactant-Mediated Interparticle Contacts on the Mechanical Stability of Supraparticles," *The Journal of Physical Chemistry C*, vol. 125, no. 42, pp. 23445–23456, 2021.

[5] A. Plunkett, C. Eldridge, G. A. Schneider, and B. Domènech, "Controlling the Large-Scale Fabrication of Supraparticles," *The Journal of Physical Chemistry B*, vol. 124, no. 49, pp. 11263–11272, 2020.

[6] C. T. S. Turk, U. C. Oz, T. M. Serim, and C. Hascicek, "Formulation and Optimization of Nonionic Surfactants Emulsified Nimesulide-Loaded PLGA-Based Nanoparticles by Design of Experiments," *AAPS PharmSciTech*, vol. 15, no. 1, pp. 161–176, 2014.

[7] W. Chen, L. Wang, R. Liu, H. Shen, J. Du, and F. Fan, "Self-Assembled and Wavelength-Tunable Quantum Dot Whispering-Gallery-Mode Lasers for Backlight Displays," *Nano Letters*, vol. 23, no. 2, pp. 437–443, 2023.

[8] A. Mejía, H. Segura, M. Cartes, and J. A. Coutinho, "Vapor-liquid equilibrium, densities, and interfacial tensions of the system hexane + 2,5-dimethylfuran," *Journal of Chemical and Engineering Data*, vol. 57, no. 10, pp. 2681–2688, 2012.

[9] D. M. Lloyd, I. T. Norton, and F. Spyropoulos, "Processing effects during rotating membrane emulsification," *Journal of Membrane Science*, vol. 466, pp. 8–17, 2014.

[10] B. Mendiboure, A. Graciaa, J. Lachaise, G. Marion, M. Bourrel, and J. L. Salager, "Influence of the intensity of mixing on the droplet size distribution of emulsions: Theory and experiment," in *Trends in Colloid and Interface Science V* (M. Corti and F. Mallamace, eds.), (Heidelberg), pp. 338–341, Steinkopff, 1991.

[11] D. Luo, X. Qin, Q. Song, X. Qiao, Z. Zhang, Z. Xue, C. Liu, G. Mo, and T. Wang, "Ordered Superparticles with an Enhanced Photoelectric Effect by Sub-Nanometer Interparticle Distance," *Advanced Functional Materials*, vol. 27, no. 44, p. 1701982, 2017.

[12] C. J. Eling, N. Bruce, N.-K. Gunasekar, P. U. Alves, P. R. Edwards, R. W. Martin, and N. Laurand, "Biotinylated Photocleavable Semiconductor Colloidal Quantum Dot Supraparticle Microlaser," *ACS Applied Nano Materials*, vol. 7, no. 8, pp. 9159–9166, 2024.

[13] J. Ward and O. Benson, "WGM microresonators: sensing, lasing and fundamental optics with microspheres," *Laser & Photonics Reviews*, vol. 5, no. 4, pp. 553–570, 2011.

[14] S. Yang, Y. Wang, and H. Sun, "Advances and Prospects for Whispering Gallery Mode Microcavities," *Advanced Optical Materials*, vol. 3, no. 9, pp. 1136–1162, 2015.

Chapter 4

Surface Functionalisation

4.1 Overview

Surface functionalisation is one of the main focuses of this thesis as it is incredibly important to be able to alter the surface of SPs and carry out biosensing experiments Achieving surface functionalisation of SPs is a novel contribution to the field and had not been demonstrated until the publication of our paper in 2023. [1] First, SPs are modified with the protein Neutravidin, a popular protein used for biological applications by exploiting the avidin-biotin interaction. Neutravidin modification is also carried out on SPs fabricated using the emulsion variants detailed in Chapter 3 to be able to see if the fabrication emulsion has an effect on surface alterations. SPs were also functionalised with a DNA aptamer, a short strand of DNA that can bind specifically to a certain biomolecule, using the EDC/NHS coupling method to prepare SP for sensing the protein Thrombin. Finally, the optical characteristics of SPs before and after functionalisation were measured to establish the suitability of the different fabrication emulsions and surface functionalisation methods for further biosensing tests.

4.2 Functionalisation with Neutravidin

The surface functionalisation procedure detailed in this section was chosen for two main reasons. First, ligand exchange is necessary to make these SPs water soluble and to replace the inert alkyl chains with carboxylic acids that can undergo simple and mild coupling reactions. Secondly, EDC/NHS is one of the more suitable coupling reactions to attach TBA to the SP surface as it does not involve the introduction of spacer groups. It is important to keep the surface chemistry within the evanescent field of the WGM cavity as the binding of the target analyte to the SP surface must occur within the evanescent field to produce any changes in the laser emission.

Synthesis of SPs was carried out using the PVA emulsion method detailed in Chapters 2 and 3. Surface functionalisation, shown in Fig 4.1, was achieved by first exchanging the inert and hydrophobic oleic acid ligands with MPA ligands to introduce hydrophilic carboxylic acid moieties onto the SP surface to make them water soluble and able to undergo further EDC/NHS coupling. Ligand exchange is able to proceed as a result of a number of different thermodynamic factors at play. First and foremost, thiols are able to bind more strongly to the surface of the CQDs that make up SPs [2,3]. However, the overall thermodynamic picture will be slightly less clear as the reduction in van der Waals forces by replacing the long alkyl chains of oleic acid with the three carbon chains of MPA will contribute to a reduction in enthalpy, even with possible hydrogen bonding between the carboxylic acid groups of MPA. The entropy would increase significantly after exchange due to the increase in conformational entropy that will occur with oleic acid unbound and free in solution. The overall Gibbs Energy would decrease, making the ligand exchange thermodynamically favourable. [2] As detailed in Section 1.5.1, ligand exchange rate also increases as ligand chain length

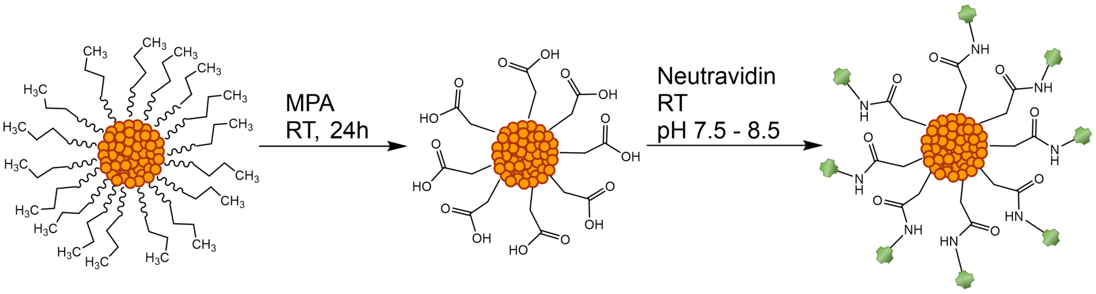

Figure 4.1: Reaction scheme depicting the procedure used to functionalise the surface of an SP with Neutravidin. The first step is a direct ligand exchange of OA with MPA, and the second step is an coupling reaction between the MPA and an amine group attached to Neutravidin.

decreases. [4] After successful ligand exchange introduced carboxylic acid groups on the surface, made possible due to the higher affinity of the thiol moiety at the other end of the chain to the CQD surface, the protein Neutravidin was coupled to the SP surface using basic conditions. [5, 6]

Successful surface functionalisation was confirmed using Fourier Transform Infrared Spectroscopy (FTIR), with the spectra shown in Fig 4.2. For OA-SPs, the black spectrum, the sharp, strong peak at 1547 cm^{-1} is attributed to the symmetric stretch of the C=O bond within the carboxylic acid group. This vibration is shifted from the expected wavenumber of around 1700 cm^{-1} due to the carboxylic acid group binding to the surface of CQDs in SPs. [7, 8] Other characteristic peaks are at 1414 cm^{-1} and 1463 cm^{-1} (methyl end group C−H, $\mathrm{CH_2}$ C−H), 2864 cm^{-1} and 2924 cm^{-1} (alkene and alkane C−H stretch), and a broad peak between 3000-3500 cm^{-1} (O−H stretch). [8–10]

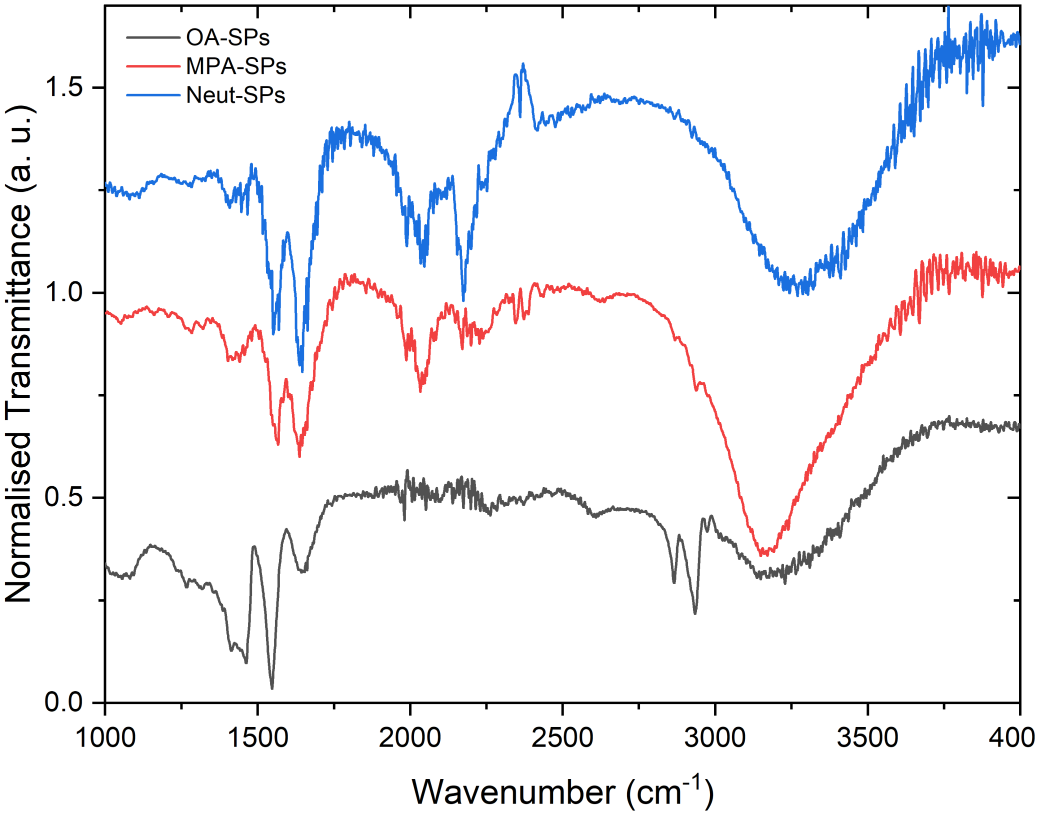

Figure 4.2: FTIR Spectra of OA-coated SPs (black), MPA-coated SPs (red), and Neutravidin-coated SPs (blue).

After ligand exchange with MPA (red spectrum), two distinct peaks at 1566 cm^{-1} and 1637 cm^{-1} are present, attributed to the C=O carboxylic acid bond. The presence of two peaks could indicate incomplete ligand exchange as the peak at 1637 cm^{-1} would be due to the carboxylic acid group being at the SP surface and not bound to the CQDs while the peak at 1566 cm^{-1} could correspond to remaining oleic acid. Peaks between 2000-2500 cm^{-1} is usually where absorption of triple bonds are located on the spectrum, however this is extremely unlikely in this case. These peaks could be due to carbon dioxide from the local environment, the water the SPs were storied in, or water vapour from sample evaporation during obtaining the spectra. [11] Background spectra were taken to mitigate this but concentrating samples onto the spectrometer took a slightly longer than it would usually due to the small scale of the samples being analysed, therefore there was more time for water to evaporate and the local environment to change. The increased intensity of the broad O−H peak between 3000-3500 cm^{-1} can also be explained by the carboxylic acid group being at the outer SP surface rather than bound to the SP CQDs. There is a large reduction in the intensity of the peak at 1424 cm^{-1}, corresponding to the alkyl C−H bonds, which is expected because of the significantly shorter chain of MPA compared to oleic acid. [8,12] The assumption that MPA binds to the surface of the CQDs within the SPs through the thiol group is backed up in this spectrum due to the lack of a peak at 1289 cm^{-1}. [13] Finally, after conjugation of Neutravidin to the SP surface (blue spectrum) the main peaks in the spectrum are at 1408 cm^{-1}, 1550 cm^{-1}, 1645 cm^{-1}, and the broad peak at 3000-3700 cm^{-1} with a slight shoulder at approximately 3400 cm^{-1}. The main difference between MPA-SPs and Neut-SPs is the presence of an amide group. The peaks at 1408 cm^{-1}, 1550 cm^{-1}, and 1645 cm^{-1} correspond to alkyl CH_2 C−H bonds, C−N, and C=O bonds, however the peak at 1550 cm^{-1} could also be attributed to any remaining oleic acid from the ligand exchange. The slight shoulder of the O−H peak at around 3400 cm^{-1} could correspond to the amide N−H stretch. [14]

Overall, due to the similarity in the types of bonds at each step of the surface functionalisation procedure, using only FTIR analysis can not provide definitive proof of success. Zeta potential measurements, shown in Table 4.1, were also taken to be

Table 4.1: Zeta Potential measurements for samples after each functionalisation step. All measurements were taken at pH 6.

Sample	ζ (mV)	σ (mV)
OA-SPs	-17.1	$\pm$ 4.05
MPA-SPs	-14.7	$\pm$ 5.73
Neut-SPs	-7.11	$\pm$ 4.67

used in conjuction with the above FTIR spectra. Zeta potential measures the electrical charge at the boundary between the rest of the solution and the part of the solution which is bound to the surface of a particle, called the slipping plane. Alterations to the surface chemistry of particles within solution has a measurable effect on the charge at the slipping plane which can indicate whether surface modifications have been successful. Surface charge measurements are sensitive to any pH changes in the solution so all measurements were taken at pH 6 to account for this. Zeta potential values were measured to be -17.1 ± 4.05 mV, -14.7 ± 5.73 mV, and -7.11 ± 4.67 mV for OA-, MPA-, and Neut-SPs respectively. Measurements between OA- and MPA- capped SPs does not show any significant change where zeta potential would usually be expected to become more negative where carboxylic acid groups are present on a surface. [13] This could also be explained by measurements being taken at pH 6 which is slightly on the acidic scale, meaning it is more likely that more carboxylic acid groups are protonated on the SP surface which would contribute to a more positively charged surface than expected, however this could also be a result of incomplete ligand exchange when the FTIR spectrum is also considered. [15, 16] Neut-SPs were found to have a more positive zeta potential which is expected and does indicate successful surface functionalisation. [17] This is because neutravidin has an isoelectric point (the pH at which the protein has a neutral charge) of pH 6.3 therefore the surface charge of Neut-SPs should be closer to 0 mV at pH 6. [18]

Measuring the size distribution of SPs after each step in the functionalisation procedure can indicate the stability of SPs to the surface alterations. Figure 4.3 shows the size distributions and corresponding average size of SPs at each step of the neutravidin functionalisation procedure, along with examples of the microscope images used to measure the microsphere diameters. Microspheres could be differentiated from the background by their bright red colour and were selected based on this criteria, along with circularity and whether the microsphere exhibited any damage or malformation. Batch to batch variance of produced microspheres did occur due to variations in temperature and humidity of the environment, however these were not found to be significant therefore the standard deviation of mixed batches were reported here. The average SP size of OA-, MPA-, and Neut-SPs are measured to be 5.9 ± 4.8 µm, 7.1 ± 3.7 µm, and 4.3 ± 3.7 µm respectively. ANOVA statistical analysis shows that each average diameter value is statistically significant and therefore can conclude the functionalisation procedure has an effect on SP diameter. In this case, the changes in average SP diamet-

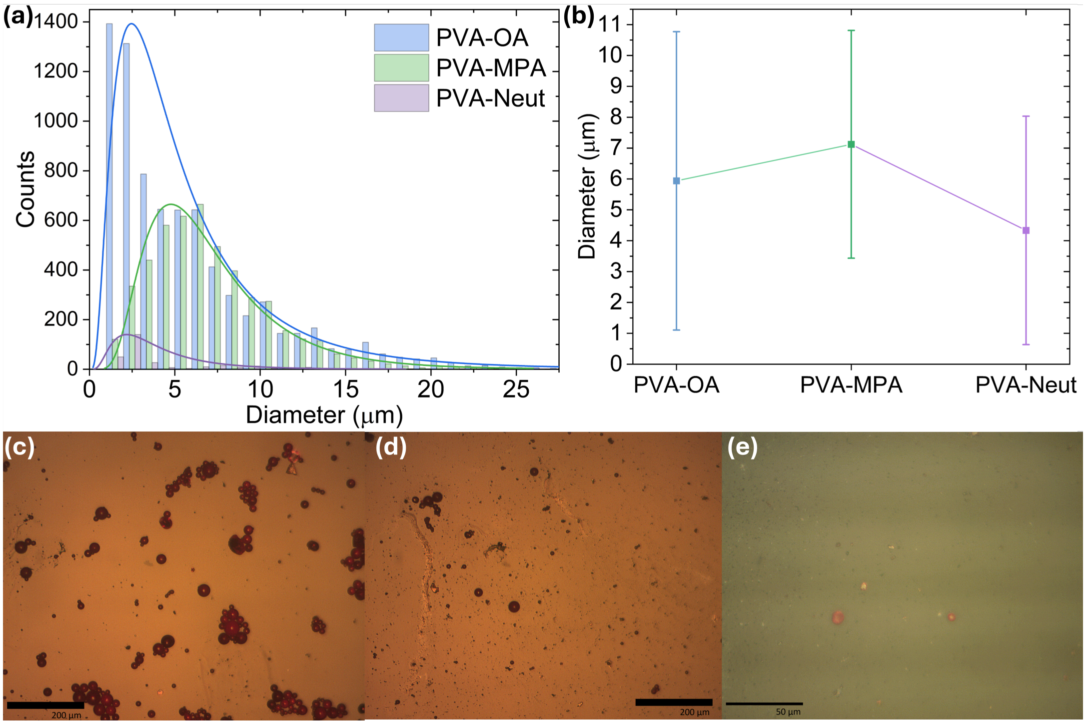

Figure 4.3: Left: Size distributions of OA- (blue), MPA- (green), Neut-SPs (purple). For the distributions, lognormal fits were used. Right: Corresponding average diameters for OA- (blue), MPA- (green), Neut-SPs (purple). Error bars represent standard deviation and the line between each point is a guide for the eye to show the difference in average diameter values more clearly. (c-e) are microscope images of PVA-OA, -MPA, and -Neut samples, respectively.

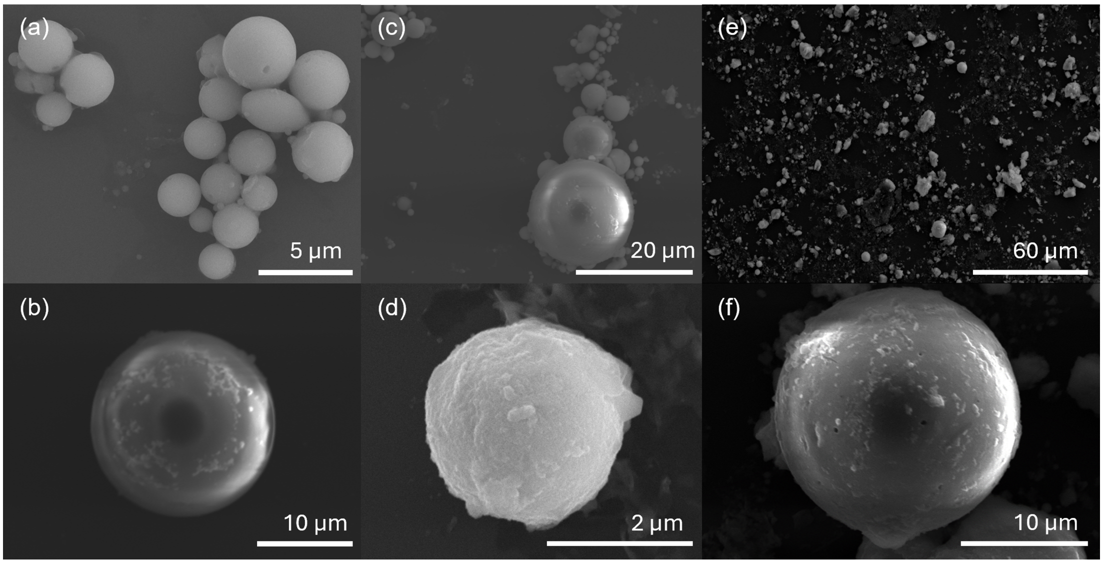

Figure 4.4: SEM micrographs of SP samples after each surface functionalisation step. (a,b) An image of a cluster of OA-SPs and a close up of a single OA-SP. (c,d) An image of a cluster of MPA-SPs and a close up of a single MPA-SP. (e,f) An image of the Neut-SP sample and a close up of a single Neut-SP.

ers do not come from the process of altering the molecules attached to the surface, but rather the effect carrying out these processes has on the SPs resulting in a reduction in population at particular sizes. All three samples demonstrate a wide size distribution, with a reduction in the number of SPs in the sample after each subsequent procedure indicating care must be taken to design a surface modification with the fewest steps possible. In particular, there is marked decrease in the number and average size of SPs after conjugation of Neutravidin which is carried out at a basic pH in an adaptation of a literature procedure. [5, 6] This indicates these SPs are only stable at neutral pH environments, as thiol ligands are reported to also be unstable in lower pH environments as the thiol groups can be protonated and detach from the surface of CQDs. [3] To be able to assess the quality of SPs within the samples SEM micrographs were taken of some wider samples and clusters and single SPs, shown in Figure 4.4. Figures 4.4(a) and (b) are images of a cluster of OA-SPs and a single OA-SP respectively. SPs within the cluster can be seen with some holes, cracked and misshapen SPs, however the majority are spherical and could be used as WGM lasers. The surface of the single SP can also be seen as relatively smooth. MPA-SPs, shown in Fig 4.4(c) and (d), also shows a small proportion of misshapen SPs, however single SPs demonstrate an altered surface and increased surface roughness. For Neut-SPs shown in Figure 4.4(e) and (f), there are many amorphous artefacts throughout the sample with fewer spherical SPs present and surface roughness can still be observed at the single SP level. The single Neut-SP also has small holes and cracks in the SP which could affect the optical characteristics of such SPs.

4.2.1 Comparison of SP Fabrication Methods

Analysing the suitability of the three variants of fabrication emulsions detailed in Chapter 3 cannot be complete without comparing their stability towards surface

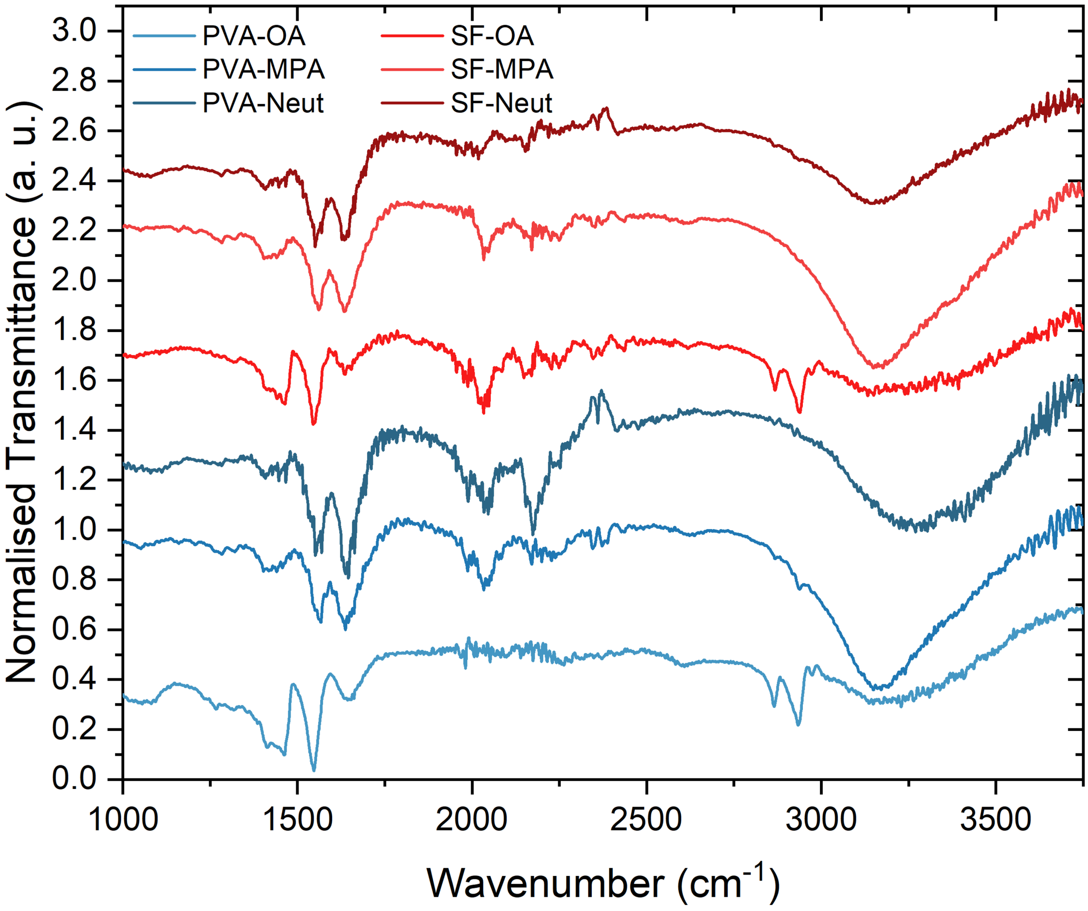

Figure 4.5: FTIR spectra of PVA- (red spectra) and SF-SPs (blue spectra) after each step in the assembly and subsequent functionalisation with Neutravidin. The yield of 3S-SPs was too small to be able to obtain suitable spectra.

Table 4.2: Zeta Potential measurements for samples made with the different fabrication emulsions after each functionalisation step, where possible. There was not a high enough yield of 3S-Neut SPs to be able to obtain reliable zeta potential measurements. All measurements were taken at pH 6.

	PVA-SPs		SF-SPs		3S-SPs	
Surface	ζ (mV)	σ (mV)	ζ (mV)	σ (mV)	ζ (mV)	σ (mV)
OA	−17.1	± 4.05	−22.0	± 3.42	−13.5	± 6.15
MPA	−14.7	± 5.73	−17.3	± 4.37	−1.27	± 5.24
Neut	−7.11	± 4.67	−3.90	± 3.39	–	–

functionalisation due to how important being able to alter the SP surface is for use. Neutravidin functionalisation was attempted for each of the fabrication methods, PVA, Surfactant free (SF), and 3-Surfactant (3S). All three samples had spherical SPs left after functionalisation, however only PVA- and SF-SPs had a yield sufficient enough to obtain proper FTIR spectra and zeta potential data. FTIR spectra of PVA- and SF-SPs after each synthetic step are shown below in Figure 4.5. The SF-OA spectrum has the expected peaks at 1464 cm^{-1} (CH$_2$ C−H), 1544 cm^{-1} (C=O), 1636 cm^{-1} (C=O), 2867 cm^{-1} and 2933 cm^{-1} (alkene and alkyl CH$_2$ C−H), and the weak, broad peak at 3100-3400 cm^{-1} (O−H). After ligand exchange, the marked increase in intensity of the broad peak corresponding to the O−H bond along with the peak at 1636 cm^{-1} corresponding to the unbound C=O bond indicates that the carboxylic acid group is unbound at the SP surface and therefore ligand exchange was successful, at least partially. The SF-Neut spectrum is incredibly similar to that of the PVA-Neut with peaks at 1409 cm^{-1}, 1550 cm^{-1}m, and 1634 cm^{-1}, indicating successful functionalisation with Neutravidin for SF-SPs however, as detailed above, this is not conclusive.

Zeta potential measurements are shown in Table 4.2, which shows a similar trend as the PVA-SPs between each fabrication method after each synthetic step in the surface functionalisation. A complete set of measurements was obtained for PVA- and SF-SPs and both sets of samples had similar zeta potential values at pH 6. As detailed in the previous subsection, the increase in surface charge seen after ligand exchange is possibly due to a combination of the pH at which the measurements are being taken and incomplete exchange leaving oleic acid molecules at the surface. Either way, both PVA-Neut and SF-Neut SPs demonstrate a significant positive shift in zeta potential expected with successful Neutravidin conjugation due to the isoelectric point of Neutravidin being at pH 6.3 [18]. This means as the pH of the solution tends towards 6.3, the overall charge of the protein nears neutrality hence the zeta potential measurements shown being close to zero. 3S-SPs were shown not to be stable towards further functionalisation, hence the yield after Neutravidin conjugation not being sufficient enough to obtain zeta potential measurements. One possible reason for this instability could be the surfactants used in the fabrication process. As discussed in Chapter 3, it is possible that during the fabrication process the surfactants used to stabilise the oil droplets are incorporated into the SP structure with the hydrophilic groups remaining on the surface [19]. This could explain the lack of stability 3S-SPs have towards further functionalisation as Tween 20 and Span 20 are bulky surfactants, and the presence of these bulky chains at the surface of the SPs could prevent the modification of the surface chemistry of CQDs and cause the breakdown of SP structures instead. Comparing 3S-OA and 3S-MPA SPs, the same increase in zeta potential after ligand exchange remains, however both values are generally more positive than those for the respective samples of PVA- and SF-SPs which could be due to the longer, neutral alkyl chains of the surfactants used in the 3-surfactant method at the surface of the SPs.

Finally, size distributions and average sizes of SPs used in tandem with SEM images can often give good indications of how stable SPs are towards further functionalisation. Figure 4.6 shows SEM micrographs of SP samples and single SPs for PVA-, 3S-, and SF-Neut samples and Figure 4.7 is the size distribution and average sizes of the SP samples. The figures with the wider samples clearly shows the dramatic decrease in the amount of spherical SPs present after each functionalisation step, with the image of the SF-Neut sample, Figure 4.6e, being the most obvious example. Upon closer inspection of SEM micrographs of single SPs shown in Figure 4.6, it is also clear that the surface of the SF-Neut SP is rougher than the PVA- and 3S-Neut SPs, which should lead to lower quality cavity, and therefore higher, unfavourable laser thresholds.

However, SEM provides a small snapshot of a sample, so size distributions of SPs were estimated using larger samples of SPs from images taken with an optical microscope with SP diameters measured using imageJ. The distributions and average diameters of PVA-, 3S- and SF- samples are shown in Figure 4.7 and give some more insight into the effect the fabrication method has on whether these SPs are suitable for further functionalisation, and therefore biosensing. PVA-SPs have a narrower size distribution, indicating there is more control over the droplet size, and therefore SP size. The average diameter of PVA-OA, PVA-MPA and PVA-Neut SP samples are 5.9 ± 4.8 µm, 7.1 ± 3.7 µm, and 4.3 ± 3.7 µm respectively. There is a reduction in the yield of SPs after Neutravidin functionalisation, and ANOVA analysis of the samples indicates the reduction in average diameter seen is significant. 3S-SPs had an average diameter of 11.2 ± 6.4 µm, 8.1 ± 4.5 µm, and 3.9 ± 2.5 µm for OA-, MPA-, and Neut-capped SPs respectively, with each average value being statistically significant. Finally, SF-OA, -MPA, and -Neut SPs were found to have average diameters of 13.7 ± 6.5 µm, 11.6 ± 3.7 µm, and 4.7 ± 2.6 µm respectively, with statistical analysis showing no significant change in diameter between SF-OA and SF-MPA samples. As shown in Figure 4.7,

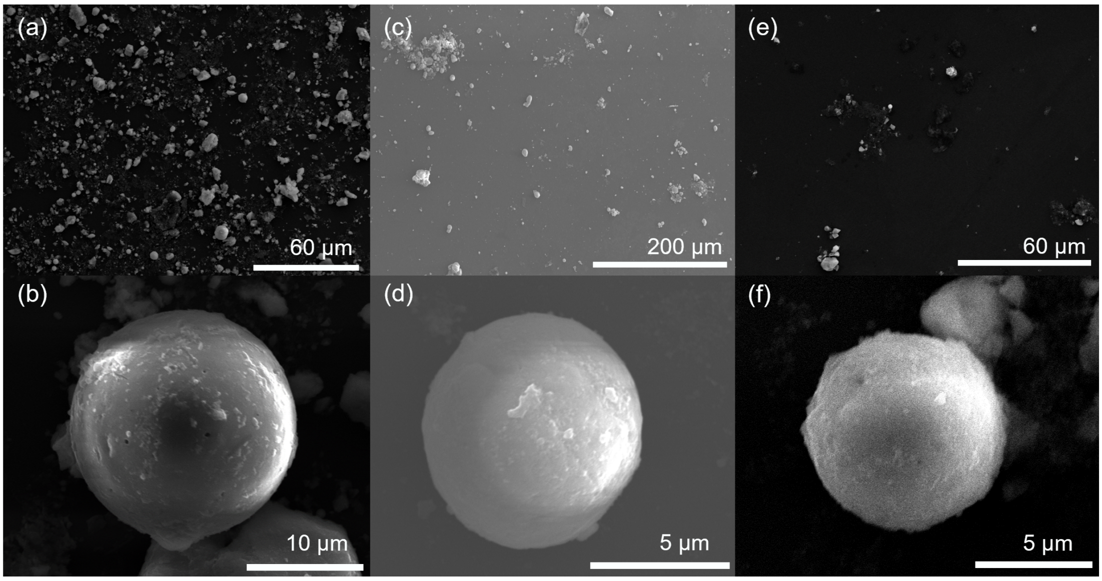

Figure 4.6: SEM micrographs of (a,b) a sample and close up of neutravidin coated PVA-SPs, (c,d) a sample and a close up of neutravidin coated 3S-SPs, (e,f) a sample and a close up of neutravidin coated SF-SPs.

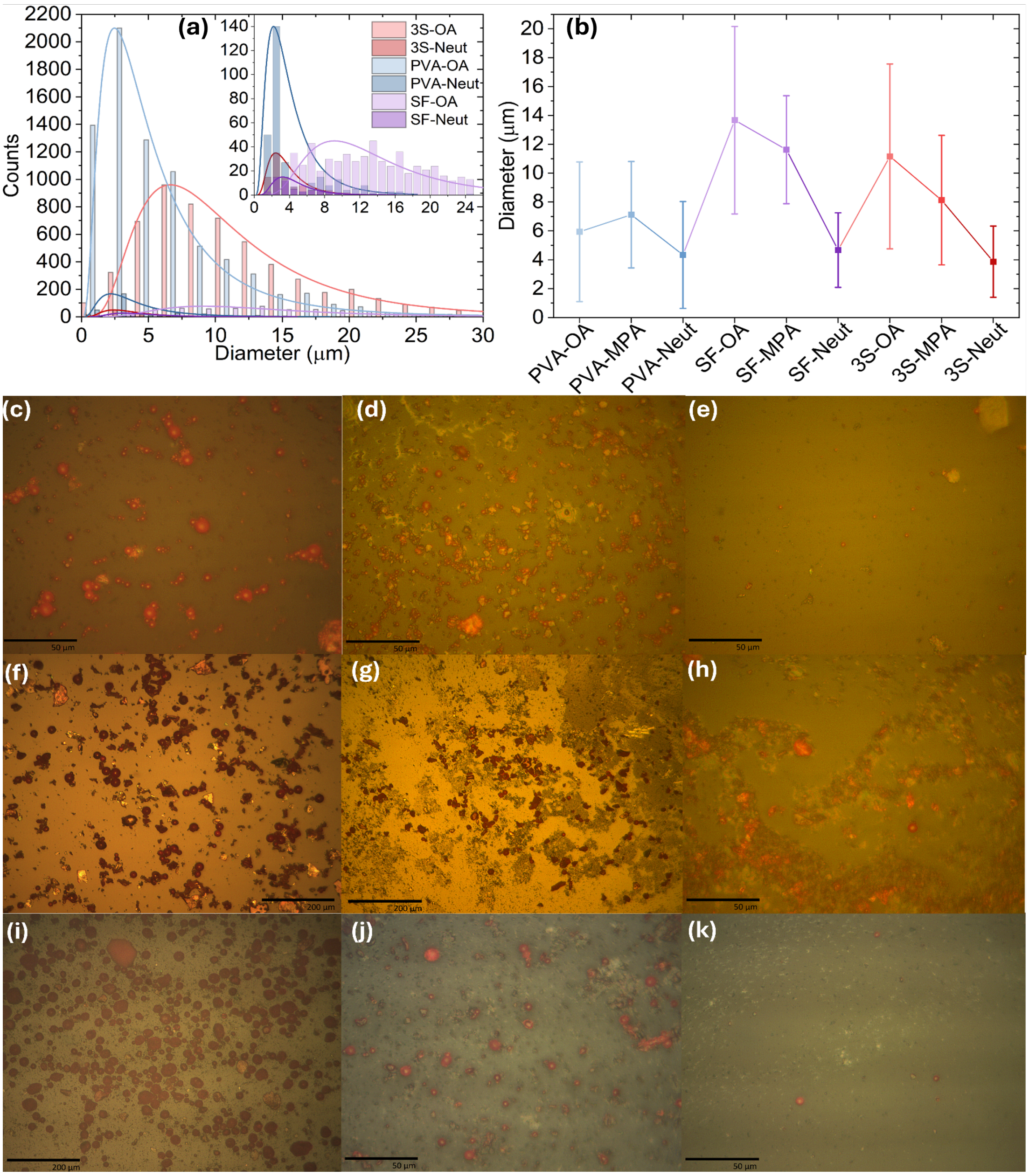

Figure 4.7: (a) Size distributions of the 3S- (red), PVA- (blue), and SF-SPs (purple) before and after surface functionalisation with Neutravidin. For the distributions, lognormal fits were used. (b) The corresponding average sizes of PVA-, SF-, and 3S-SPs at each step of the surface functionalisation procedure. Error bars represent standard deviation and the line between each point is to show the difference in average diameter values more clearly.(c-k) Microscope images of SP samples produced after each step. (c-e) are PVA-OA, -MPA, and -Neut samples, (f-h) are SF-OA, -MPA, -Neut samples and (i-k) are 3S-OA, -MPA, and -Neut samples.

with the exception of PVA-MPA, the average diameters of SPs tend to reduce after each step in the surface functionalisation procedure, with each Neut-SP sample having a statistically identical average diameter, demonstrating a level of instability towards further reactions across all SPs regardless of the emulsion method used in fabrication. The 3S method produces generally much larger SPs than those made using the PVA method with a similarly higher yields, with 3S-SPs being more polydisperse, whereas the SF method, while also producing larger SPs, has a dramatically lower SP yield in comparison. The SF method also did not produce reliable results that could be easily replicated with each synthesis attempt, therefore is not suitable for further study particularly when focusing on biosensing or other applications that require further chemical treatment. It is possible that this method could be made more reliable and produce more suitable results if carried out in a smaller vial than used in this work, as is the case within the literature, as scaling the reaction up did not produce viable samples. [20] As the main difference between the methods is in the presence and absence of surfactants, it is therefore not unreasonable to infer the importance of this factor when it comes to further solution processing and surface functionalisation. As discussed in Chapter 3, it is possible that surfactants used in fabrication remain within the structure of SPs with the hydrophobic chains remaining embedded between CQDs and the hydrophillic sections remaining at the SP surface. [19, 21] As the 3S method uses three different surfactants, with Span 20 and Tween 20 having significantly bulkier hydrophilic end groups than PVA shown in Figure 4.8, there would be more of the hydrophilic and reactive sections of the surfactant at the SP surface to interfere with surface functionalisation. This could result in the breakdown of SPs and lower yields seen after each functionalisation step. It is also possible for the −OH groups attached to both PVA, Span 20, and Tween 20, to bind to the surface of CQDs within the SP, therefore attempts to alter the surface chemistry of CQDs in the SP would require displacing the surfactants from the surface, along with the possibility of attempted EDC/NHS coupling at the carboxylic acid groups within Tween 20 and Span 20, both leading to SP dissolution. As the 3S surfactants and PVA would be able to bind to the surface of multiple CQDs within SPs, they could also be responsible for increasing

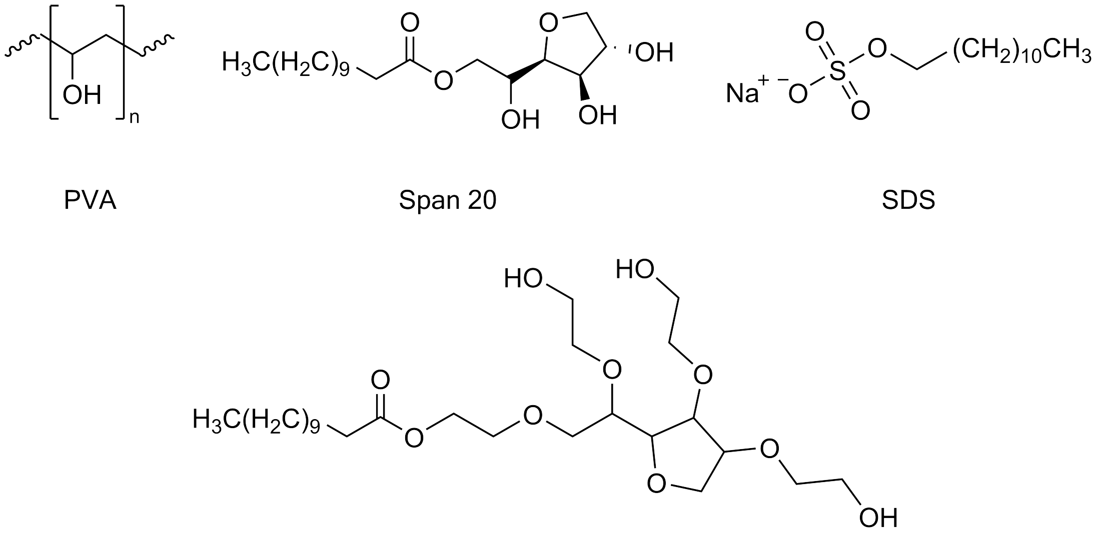

PVA

Span 20

SDS

Tween 20

Figure 4.8: The chemical structure of PVA and the three surfactants used in the 3S synthesis: Span 20, Sodium Dodecyl Sulfate (SDS), and Tween 20.

the stability of SPs by counteracting the steric repulsion between the oleic acid ligands on the surface of the SP CQDs and binding the CQDs together. [22] PVA being less bulky would be more favourable for binding between CQDs, which could go towards explaining the superior stability of PVA-SPs when compared to 3S-SPs. Surfactants binding between CQDs with SPs also goes towards explaining the significantly poorer yields and stability of SF-SPs compared to syntheses that used surfactants. Without the surfactants to bind CQDs together and counteract the steric and electrostatic repulsion between CQDs and the oleic acid ligands, the SPs would be much more susceptible to dissolution and break down.

4.3 Functionalisation with a DNA Aptamer

Functionalisation with a DNA Aptamer, shown in Fig. 4.9, was achieved using SPs fabricated using the PVA method due to their superior stability towards further functionalisation demonstrated in comparison to the two alternative emulsions trialled. Ligand exchange with MPA was still required to introduce the necessary carboxylic acid moieties onto the SP surface for the subsequent EDC/NHS coupling to conjugate the

DNA aptamer, Thrombin Binding Aptamer with 15 bases in the chain (TBA-15), to the SP surfaces. Although usually carried out in buffer solution to control the pH of the reaction effectively, MPA-SPs were found to be unstable in buffer and dissolve back into QDs hence the coupling being carried out in water with 2 µL of 10 mM NaOH added every 20 minutes to control the reaction pH. The TBA used in this work consists of 15 bases within the main DNA chain, a methyl group at the 3' terminus and an NHS group with a 6-carbon linker at the 5' terminus of the DNA strand. This short chain TBA was chosen to ensure the molecules at the sensor surface are within the evanescent field of the WGMs as WGM biosensing requires the target analyte binding to be within that field to induce a change in laser wavelength. [23,24] As above, FTIR and zeta potential were used to determine whether the surface functionalisation was successful. The FTIR spectra of OA-, MPA-, and TBA-SPs are shown in Figure 4.10. For OA-SPs (black line), the broad peak between approximately 3000-3500 cm^{-1} and the strong, sharp peak at 1635 cm^{-1} correspond to the symmetric stretching of O−H and C=O bonds of the carboxylic acid group of the oleic acid ligands. For OA-SPs, other characteristic peaks can be seen at 2933 and 2971 cm^{-1} corresponding to stretching of C−H bonds attached to alkane and alkene carbons in the oleic acid chain along with peaks at 1411 and 1462 cm^{-1} corresponding to the bending of these same bonds. [12] The main difference seen between the FTIR spectra of OA- and MPA- capped SPs is the near disappearance of the C−H bending and stretching peaks which is expected as oleic acid ligands with

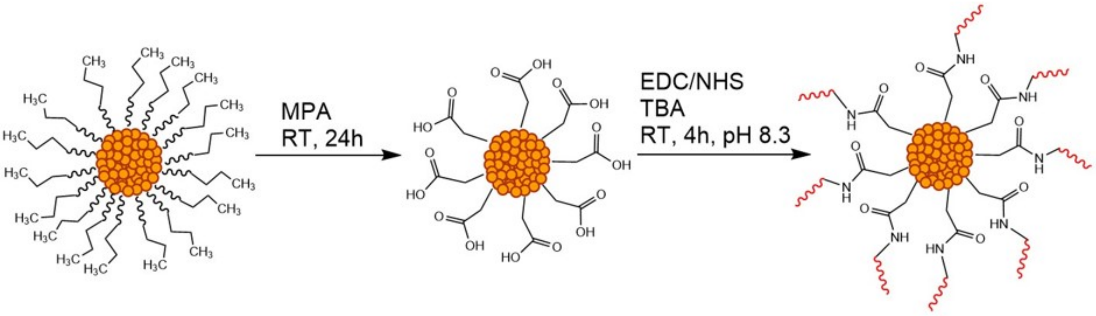

Figure 4.9: Reaction scheme depicting the procedure used to functionalise the surface of an SP with TBA-15. The first step is a direct ligand exchange of OA with MPA, and the second step is an EDC/NHS coupling reaction between the MPA and the amine end group of TBA-15.

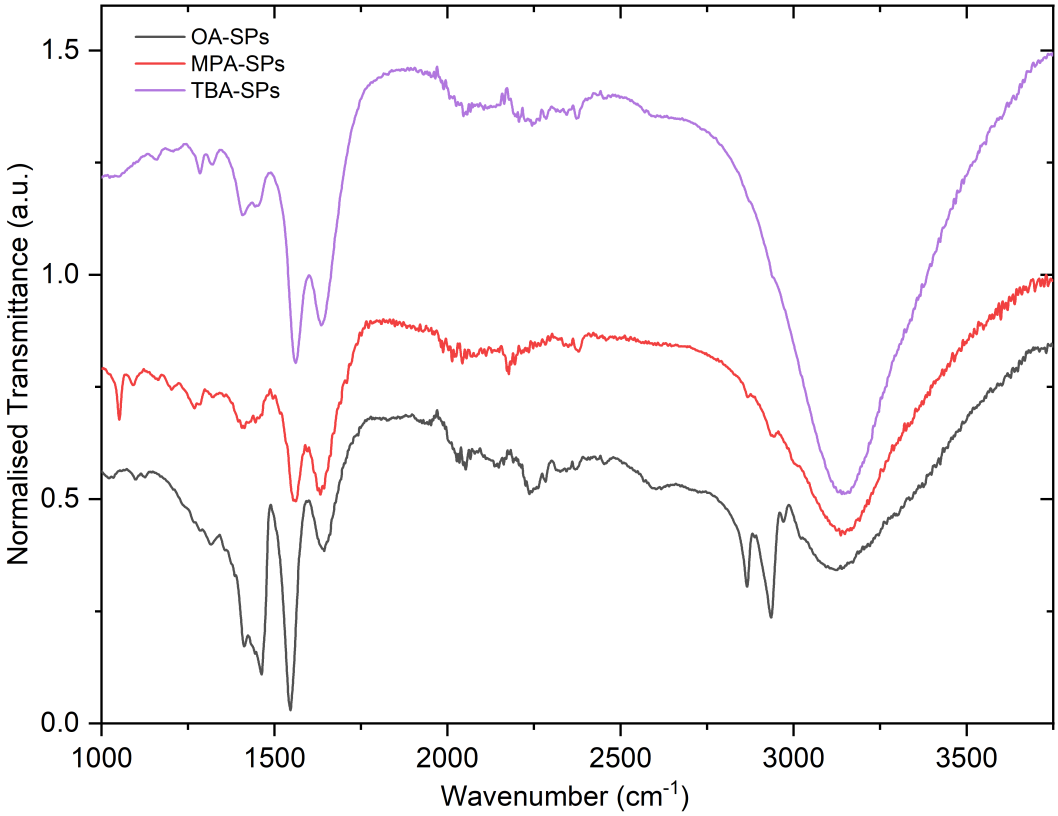

Figure 4.10: FTIR spectra of OA-SPs (black), MPA-SPs (red) and TBA-SPs (purple).

18-carbon long chains are replaced with MPA molecules which contains only a three carbon chain. There is a marked increase in the intensity of the broad O−H peak between 2900-3500 cm^{-1} which is possibly due to the carboxylic acid not being bound to the surface of the CQDs within the SPs due to the thiol group of MPA being the binding group anchoring the ligands to the CQDs instead. The lack of a peak between 2500-2600 cm^{-1} corresponding to S−H stretching demonstrates that MPA binds to the CQDs through the thiol end of the chain. [2,25] The reduction in intensity of the bound C=O peak at 1560 cm^{-1} and the peak at 1632 cm^{-1}, corresponding to C=O groups at the surface of SPs instead of what is binding the ligands to the surface of CQDs, indicates that the ligand exchange may not be fully complete. [8] For a more complete ligand exchange, the reaction could be left for more than 24 hours, however this would be to the detriment of the stability and yield of MPA-SPs as they are not as stable in solvents as OA-SPs. Another somewhat significant peak is the weak, sharp peak at

Table 4.3: Zeta Potential measurements for samples after each step of the surface functionalisation with TBA-15. All measurements were taken at pH 6.

Sample	ζ (mV)	σ (mV)
OA-SPs	-19.7	$\pm$ 4.76
MPA-SPs	-31.7	$\pm$ 3.62
TBA-SPs	-12.5	$\pm$ 3.13

1145 cm^{-1}, and this is likely due to residual ethanol from the ligand exchange mixture in the water MPA-SPs were stored in. The FTIR spectrum of the TBA-SPs sample has peaks at 1635 and 1561 cm^{-1} corresponding to C=O and C−N, the amide I and II bands respectively, with the amide III band also being visible at 1321 cm^{-1}, indicating successful EDC/NHS coupling and formation of amide bonds. [14, 26, 27] FTIR, as detailed above, is not conclusive by itself due to the similarity in the types of bonds present, therefore zeta potential measurements were taken which are shown in Table 4.3. Each sample was taken at pH 6 to be able to compare the zeta values to determine whether TBA-15 was successfully attached to the surface of SPs. Zeta potential values were measured to be -19.7 ± 4.76, -31.7 ± 3.62, and -12.5 ± 3.13 mV for OA-, MPA-, and TBA-SPs respectively. The significant decrease in surface charge between OA- and MPA-SPs can be explained by the deprotonation of the carboxylic acid of the MPA ligands on the SP surface in solution, which would contribute to the more negative zeta potential measurement. [13, 15] TBA is a more bulky molecule, explaining the increase in surface charge however the aptamer is still negatively charged, contributing to the overall negative surface. [28] Combining the FTIR spectra and zeta potential measurements indicates successful conjugation of the DNA Aptamer TBA-15 to the surface of the SPs.

Average sizes and the size distribution of SP samples after each step of surface functionalisation are shown in Figure 4.11, with the average sizes of OA-, MPA-, and TBA-SPs measured as 5.9 ± 4.8 µm, 7.1 ± 3.7 µm, and 2.9 ± 1.2 µm respectively. The size distributions also demonstrate the decreasing yield of SPs after each surface alteration, with EDC/NHS coupling having the biggest effect, indicating a lack of

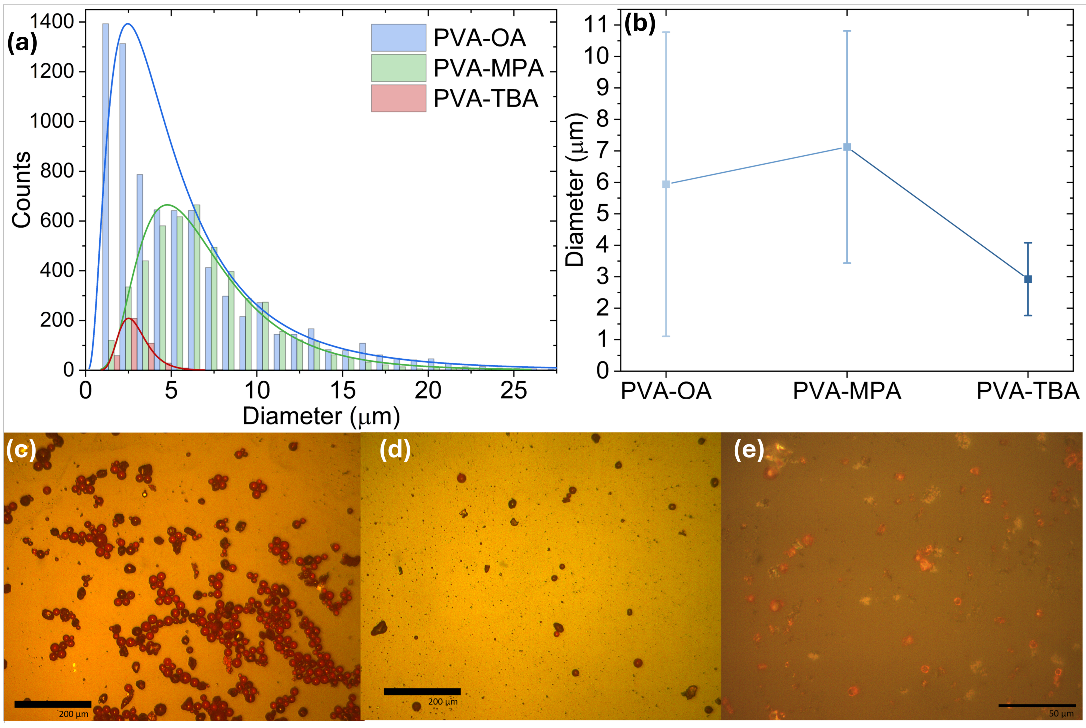

Figure 4.11: (a) Size distributions of PVA-SPs at each step of the surface functionalisation step. For the distributions, lognormal fits were used. (b) Corresponding average diameters of SP samples after each functionalisation step. These average diameters were found to be 5.9 ± 4.8 µm, 7.1 ± 3.7 µm, and 2.9 ± 1.2 µm for OA-, MPA-, and TBA-capped SPs respectively. Error bars represent standard deviation and the line between each point is a guide for the eye to show the difference in average diameter values more clearly. (c-e) Microscope images of OA-, MPA-, and TBA-capped SP samples.

stability towards pH controlled reactions. EDC/NHS coupling has an optimal reaction pH of 8.5 [29] which caused these SPs to dissolve back into CQDs, therefore the coupling had to be carried out at pH 6−7 and the reaction left for 4 hours to compensate for the reduced rate of aptamer coupling. [30] SEM micrographs of samples are also shown in Figure 4.12 showing the wider samples and individual SPs. Figure 4.15 clearly demonstrates the reduction in SP surface quality and SP size, with the surface of individual SPs shown to become more rough along with the appearance of defects and holes, particularly obvious in Figure 4.12d. For the wider sample micrographs, the main observation is the reduction in the amount of SPs, and the malformed side products, after each functionalisation step. The proportion of SPs to inadequate side

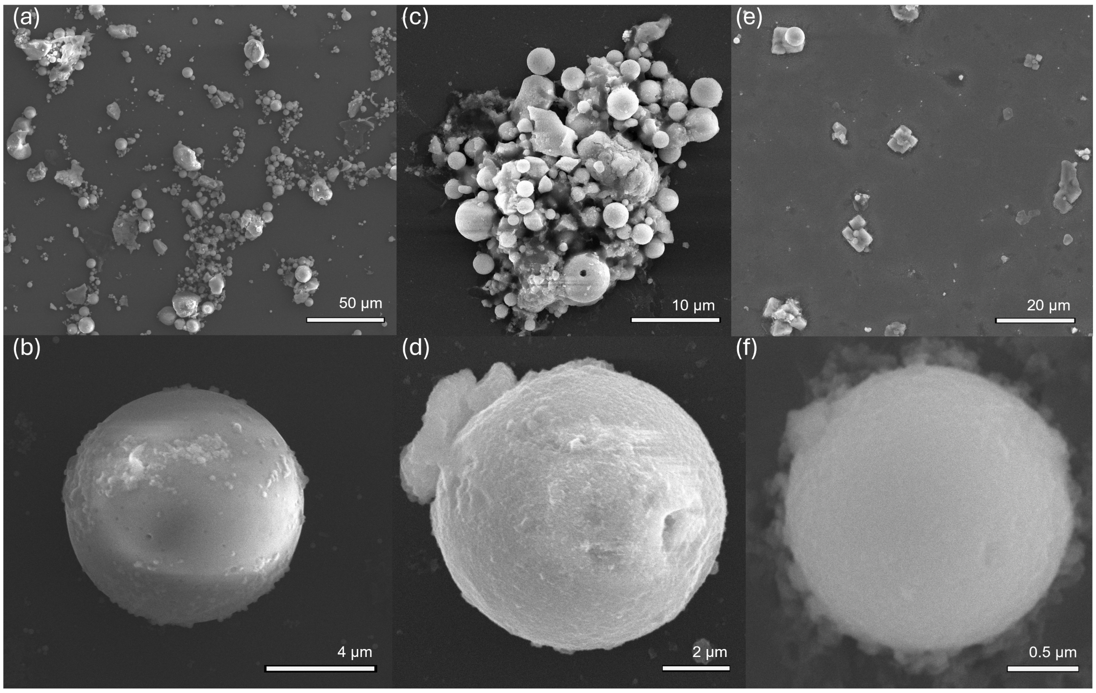

Figure 4.12: SEM Micrographs of SP samples. (a,b) An OA-SP sample and a close-up of a single OA-SP. (c,d) An MPA-SP cluster and a close up of a single MPA-SP. (e,f) A TBA-SP sample and a close-up of a single TBA-SP.

products also decreases which further highlights the decrease in stability towards further functionalsiation. In summary, these data shows that any application for these SPs that requires surface engineering requires careful planning to reduce the number of steps in the functionalisation procedure and to understand the limitations imposed on the reactions that can be conducted without damaging the resulting SPs and reducing the SP yield too much. Unfortunately, the conclusion is that there are also limitations on the possible applications of these SPs currently. One possible method that could be used to mitigate the damage to SPs is to coat the SPs in a protective shell, such as silica or PEG chains. Using PEG may allow us to introduce moieties onto the surface of SPs without subsequent reactions.

4.4 Optical Measurements

For measurement of PL spectra and estimation of laser thresholds for SPs after each functionalisation step, where possible, the setup described in Chapter 2 and shown in Figure 2.1 was used to pump individual SPs. The pump source was a 350 nm, 5 ns pulsed Nd:YaG diode laser with a repetition rate of 10 Hz.

PL spectra and laser transfer function (LTF) plots for PVA-SPs after each synthetic step are shown in Figure 4.14. The thresholds of these SPs are estimated using Figure 4.14b at the intersection of the linear fits of the emission intensity as a function of pump fluence of the SP laser operating above and below threshold. Using this method, the thresholds of single PVA-SPs before and after surface functionalisation were estimated to be 23.3 ± 3.2 mJ/cm^2, 22.6 ± 3.1 mJ/cm^2, and 25.1 ± 3.5 mJ/cm^2 for the OA-, MPA-, and Neut-capped SP respectively. These SP samples were tested from the same batch used for the modification process, and these SPs were selected as they were the most similar in diameter that could be found from those measured, even though they are quite different. Both the OA- and MPA-SPs shows two laser modes at 634 and 641 nm and 628 and 635 nm respectively, however the Neut-SP does not

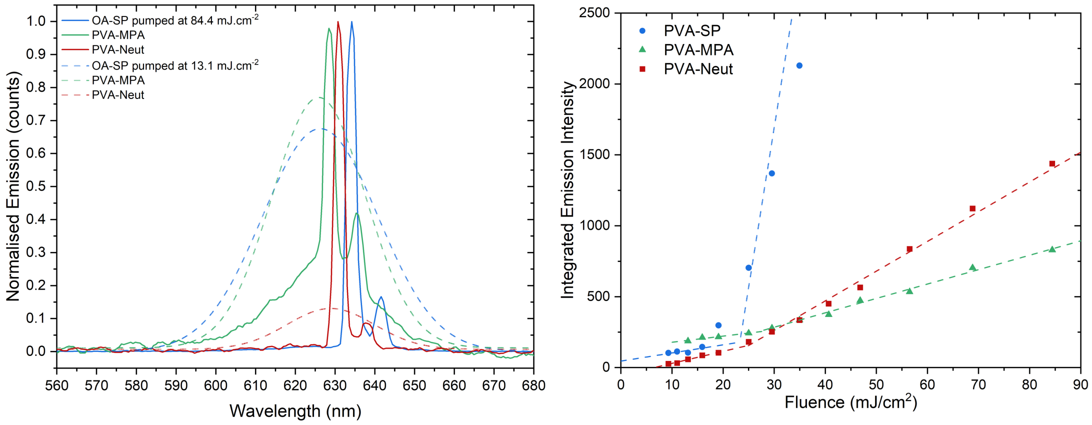

Figure 4.13: (a) Normalised PL spectra above (solid lines) and below (dashed lines) threshold for OA- (dark blue), MPA- (green) and Neut-SPs (red). The diameters of the SPs are 9.1 µm, 5.1 µm, and 2.8 µm for the OA-, MPA-, and Neut-SP respectively. (b) Laser transfer function plot used to estimate the threshold of the three SPs shown in (a). Thresholds were estimated to be 23.3 ± 3.2 mJ/cm^2, 22.6 ± 3.1 mJ/cm^2, and 25.1 ± 3.5 mJ/cm^2 for the OA-, MPA-, and Neut-SP respectively.

demonstrate any additional modes which is likely due to the size disparity of the SPs measured. The OA-SP has a diameter of 9.1 µm and the MPA-SP has a diameter of 5.1 µm, whereas the diameter of the Neut-SP is 2.8 µm as measured by ImageJ using images taken below threshold with the camera integrated into the optical setup used to collect the PL spectra (setup schematic is shown in Figure 2.2, Chapter 2). The number of lasing modes in a WGM laser is dependent on the size of the cavity, with smaller cavities more able to achieve single mode lasing, which could explain the single lasing peak only seen with the Neut-SP. [31] While the SP is demonstrating a single polar mode, it is also possible that this is not true single mode lasing as the limited resolution of the spectrometer (1 nm) means other modes, if there, have not been detected. Even above threshold, the PL emission of the MPA-SP shown in Figure 4.14a has a significant contribution to the spectrum, compared to the OA- and Neut-SP. There are many factors that could contribute to this but the main factor is likely to be the size mismatch between the SP being measured and the pump beam spot size, meaning a lower percentage of the pump beam power is absorbed into the SP, which also increases the estimated threshold for smaller SPs. Other contributing factors could include lower Q factor meaning cavity losses are increased. [31] Smaller SPs or artefacts being attached to the surface of the SP could increase the PL emission collected, which can be seen on SEM images (see Figure 4.12) but are not visible on the camera attached to the PL setup as the images only show single SPs. It would also be expected that MPA-SPs would have reduced PL emission relative to OA-SPs due to the lower SP size to beam spot size as ligand exchange reduces the quantum yield of CQDs. [3, 15] The smaller SP cross-sectional area to beam spot size ratio, along with the lower quantum yield, can be seen clearly in the LTF plots after each step in the functionalisation process, with the slope efficiency of the MPA- and Neut-SP dramatically lower than that of the OA-SP.

For comparison between different SP assembly methods and their suitability for further applications, optical measurements were attempted with SPs after each functionalisation step for each method. Neither the 3S nor the SF method produced favourable results, with only 3S-MPA SPs capable of demonstrating lasing post functionalisation.

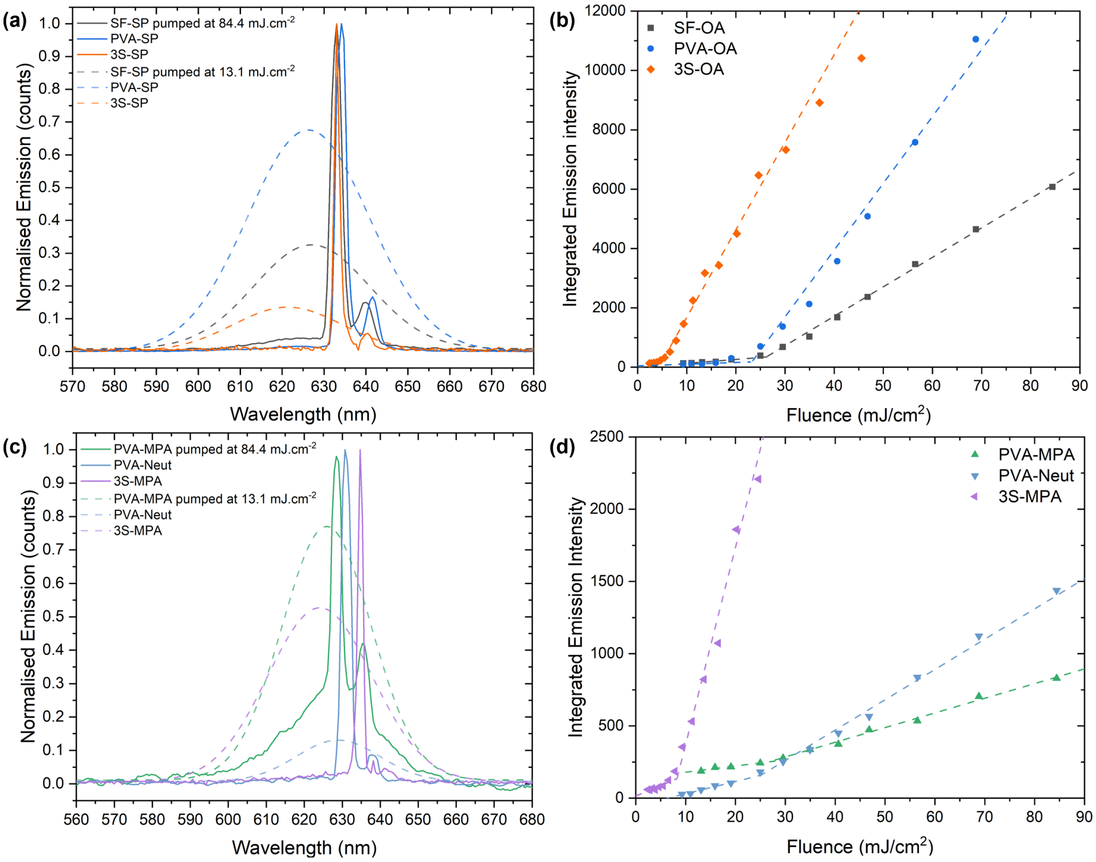

Figure 4.14: (a,b) Normalised PL spectra above (solid lines) and below (dashed lines) threshold and corresponding LTF plots for single oleic acid coated SPs assembled using the SF, PVA, and 3S methods. Thresholds were estimated to be 26.2 ± 2.6 mJ/cm^2, 23.3 ± 3.2 mJ/cm^2, and 4.7 ± 0.4 mJ/cm^2 for the SF-OA, PVA-OA, and 3S-OA SPs respectively. (c,d) PL spectra above (solid lines) and below (dashed lines) threshold and corresponding LTF plots for single MPA and Neutravidin coated SPs fabricated using the PVA and 3S methods. Thresholds were estimated to be 22.6 ± 3.1 mJ/cm^2, 25.1 ± 3.5 mJ/cm^2, and 9.0 ± 0.8 mJ/cm^2 for the PVA-MPA, PVA-Neut, and 3S-MPA SPs respectively.

Figure 4.14 shows the PL spectra and LTF of PVA-, 3S-, and SF-SPs before (a,b) and after surface functionalisation (c,d), where possible to be able to compare the impact on surface functionalisation between SPs fabricated with the different methods. The main, and most obvious, difference was the inability to find lasing in any SF-SP or 3S-Neut samples post-functionalisation, thus these fabrication methods are not suitable for producing functional laser biosensors. Lasing ability was found in 3S-MPA SPs, with the threshold estimated to be 9.0 ± 0.8 mJ/cm^2 which is significantly lower in comparison to the estimated thresholds of 22.6 ± 3.1 mJ/cm^2 and 25.1 ± 3.5 mJ/cm^2 for the PVA-MPA and PVA-Neut respectively. The LTF for the PVA-Neut SP does not go to zero as the PL signal below threshold is below the noise floor. Small SPs, such as the PVA-Neut here, seem to have negligible PL signal below threshold which could be due to the lower PLQY of CQDs after surface alterations mentioned earlier or possibly the presence of fewer CQDs in a smaller SP. The MPA-SP LTF also does not extrapolate to zero, which is possibly due to the nonlinear relationship between pump fluence and CQDs PL due to saturation. [32] As established earlier, size of the cavity is an important factor influencing the threshold for WGM lasers and the diameter of the SPs shown in Figure 4.14c and d are 5.1, 2.8, and 10.3 µm for PVA-MPA, PVA-Neut, and 3S-MPA respectively which will be a significant factor to explain the favourable lower laser threshold for the 3S-MPA SP. This may also be a contributing factor to the improved slope efficiency of the 3S-SPs both before and after functionalisation. In addition, the 3S method uses a CQD solution that is 8 times more concentrated than the PVA and SF methods - 160 mg/mL compared to 20 mg/mL - leading to an increased density of CQDs within SPs, therefore contributing to the lower thresholds and higher slope efficiency seen here. Unfortunately, the promising optical properties do not translate to stability after surface functionalisation steps. As discussed earlier, surfactant molecules remaining at the SP surface could be causing the reduction in quality and yield of 3S-SPs post functionalisation, however the optical characteristics of the extremely few lasers that are able to withstand ligand exchange do not seem to be negatively affected. [19]

SPs functionalised with the DNA Aptamer TBA-15 were also tested to determine whether they could be used as functional laser biosensors. Figure 4.15 shows the normalised PL spectra, above and below thresholds, and corresponding LTF plots for single OA-, MPA-, and TBA-SPs tested on the microPL setup. All SPs shown in Figure 4.15 are within a micron of each other, with diameters of 5.5 µm, 6.4 µm, and 5.0 µm for the OA-, MPA-, and TBA-SP respectively, allowing for better comparison of the optical properties of these SPs. The laser thresholds of these SPs were estimated to be 4.1 ± 0.4 mJ/cm^2, 7.6 ± 0.4 mJ/cm^2, and 19.8 ± 2.7 mJ/cm^2 for the OA-, MPA-, and

TBA-SP respectively. Threshold values increasing, along with the slope efficiency decreasing, after each surface functionalisation process further entrenches the importance of reducing the required synthetic steps as much as possible, however the threshold of 19.8 mJ/cm^2 is sufficiently low enough to be able to achieve sufficient lasing signal without damaging or melting the SP after one use. It is also important to remember that the incident pump laser beam spot size is larger than a single SP so not all of the energy from the pump laser is able to be absorbed by the SP, therefore the 'real' laser thresholds for these SPs will be lower than reported. [33] The PL spectra above threshold for the TBA-SP shown in Figure 4.15a also demonstrates single mode lasing which will be important for bionsensing applications as any wavelength shifts due to presence of analytes are easier to detect and track. [34] Figure 4.16 contains the box plots produced to show the diameters and thresholds of all lasing SPs found across the OA-, MPA-, and TBA-SPs samples tested. One of the more glaring differences between each of the samples is the sample size of lasing SPs decreasing after each functionalisation reaction, however this will also be linked to the decrease in SP yield after each surface alteration and does not necessarily prove a significant reduction in laser quality. ANOVA shows that only the average diameter values for OA- and MPA-SPs

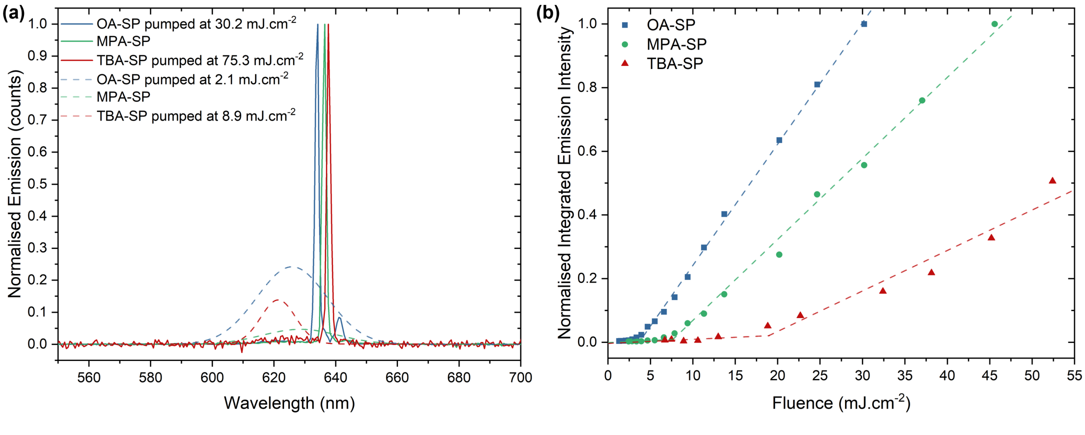

Figure 4.15: (a) Normalised PL spectra of single OA- (blue), MPA- (green) and TBA-SPs (red) above (solid lines) and below (dashed lines) threshold. The diameters of these SPs were 5.5 µm, 6.4 µm, and 5.0 µm for the OA-, MPA-, and TBA-SP respectively. (b) LTF of the OA-, MPA-, and TBA-SPs with the emission intensity normalised for clarity. Thresholds were estimated to be 4.1 ± 0.4 mJ/cm^2, 7.6 ± 0.4 mJ/cm^2, and 19.8 ± 2.7 mJ/cm^2 for the PVA-OA, PVA-MPA, and PVA-TBA SPs respectively.

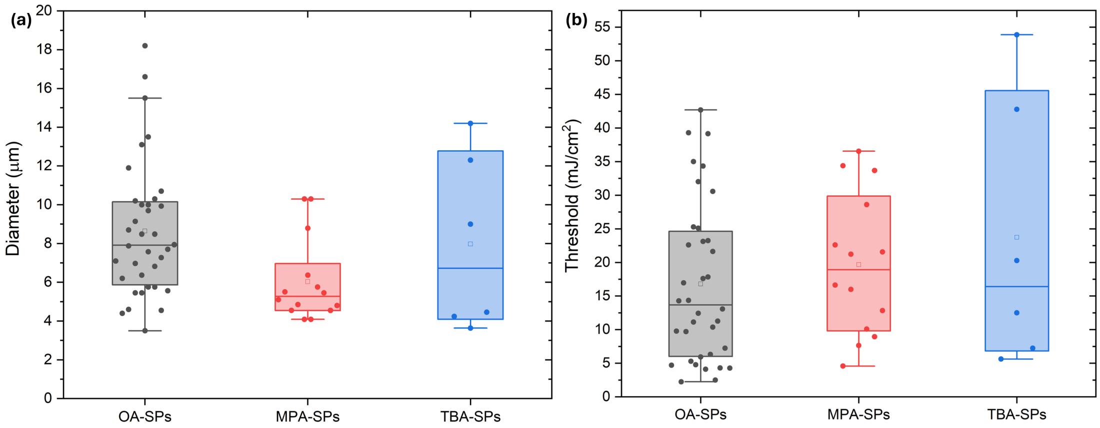

Figure 4.16: (a) Box plot showing the laser diameters of all SP lasers found in OA-, MPA-, and TBA-SP samples. The average laser diameters were 8.6 ± 3.5 µm, 6.0 ± 2.2 µm, and 7.3 ± 4.7 µm for OA-, MPA-, and TBA-SPs respectively. (b) Box plots showing the corresponding laser thresholds of all SP lasers found in OA-, MPA-, and TBA-SP samples tested. Average thresholds were estimated to be 16.8 ± 11.8 mJ/cm^2, 19.7 ± 10.5 mJ/cm^2, and 23.7 ± 20.1 mJ/cm^2 for the OA-, MPA-, and TBA-SPs respectively. A full list of the measurements is in Appendix A.2, Table A.2.

are statistically significant from each other, however all three average diameter values of 8.6 ± 3.5 µm, 6.0 ± 2.2 µm, and 7.3 ± 4.7 µm for OA-, MPA-, and TBA-SPs, respectively, are very similar to each other regardless. All three samples demonstrate SPs as small as 3.5 - 4.0 microns are able to demonstrate lasing which is promising for developing lab on a chip biosensing devices. The average thresholds of OA-, MPA-, and TBA-SPs that were found to lase were 16.8 ± 11.8 mJ/cm^2, 19.7 ± 10.5 mJ/cm^2, and 23.7 ± 20.1 mJ/cm^2, respectively, with all of these values being statistically insignificant from each other. The box plot for TBA-SP laser thresholds shown in Figure 4.16b does demonstrates that TBA-SPs are capable of achieving thresholds much lower than 19.8 ± 2.7 mJ/cm^2 reported above, with the lowest threshold TBA-SP found to be 5.6 mJ/cm^2 with a diameter of 3.6 µm, further indicating that TBA-SPs would be able to be trialled as laser biosensors.

4.5 Conclusion

Surface functionalisation of SP lasers with the protein Neutravidin and DNA aptamer TBA-15 was successfully achieved for the first time using a simple and mild procedure.

First, OA molecules were exchanged with MPA molecules to introduce carboxylic acid groups onto the SP surface and subsequently coupled with Neutravidin using a mildly basic solution, or TBA using EDC/NHS coupling. Functionalisation was confirmed using FTIR spectroscopy and zeta potential measurements, with the increase in surface charge indicating successful functionalisation with both biomolecules. It would be interesting to attempt to obtain ^{1}H NMR spectra for SPs after each step to be able to more definitively conclude successful surface functionalisation, however spectra may be too difficult to analyse and the issue of SPs precipitating at the bottom of the sample tube would also prove problematic. Thermogravimetric analysis could also be trialled with SPs to test how many Neutravidin and TBA molecules were able to be attached to the SP surface. Both TGA and ^{1}H NMR have been used on samples of CQDs alone, so it would be interesting to see if these methods are as effective with SPs in comparison. The functionalisation methods used were chosen due to their simplicity and mild reaction conditions because average diameters and yields show that SPs are not fully stable towards pH controlled coupling methods, which requires improvement. This could be achieved through coating SPs with a silica shell or PEG, which would have the added bonus of being able to be functionalised prior to coating SPs, however caution is needed to ensure the shell is thin enough for the addition of the target analyte to be within the evanescent field of the WGMs to enable sensing.

PVA-SPs after functionalisation with Neutravidin and TBA-15 were found to retain lasing functionality and therefore could be used as laser biosensors. TBA-SPs were found to have lower thresholds than Neut-SPs on average, with the thresholds reported in this work of 19.8 ± 2.7 mJ/cm^2 and 25.1 ± 3.5 mJ/cm^2, respectively. These thresholds are low enough for lasing to be achieved at a pump energy that will not damage SPs which is obviously beneficial for trying to manufacture reusable and durable laser biosensors. These functionalised lasers also demonstrated lasing at small diameters, with Neut- and TBA-SPs with diameters as small as 2.4 µm and 3.6 µm able to lase, therefore it could be possible to use them in chipscale sensors. Future work should focus on streamlining the functionalisation process and improving SP stability towards more harsh solution processing, along with trialling integration of SPs into microfluidic chips to attempt to produce an easy to use biosensor using a lab on a chip configuration.

SPs made using the difference fabrication methods detailed in Chapter 3 were also trialled to determine if the other methods may be favourable for further functionalisation. SF-SPs could be functionalised successfuly, but no lasing MPA- or Neut-coated SF-SPs could be found in the samples produced and the low yield of SPs from this method even from the initial self assembly make these SPs unsuitable for use as biosensors. 3S-SPs were able to withstand ligand exchange with MPA, however after coupling with Neutravidin, the complete collapse in the number of SPs yielded was insufficient to prove successful coupling and no lasing SPs could be found in the samples produced after coupling. Optical measurements of the single MPA-capped 3S-SP did demonstrate favourable slope efficiency and a low threshold of 9.0 ± 0.8 mJ/cm^2, indicating that these SPs are promising for further use. However, the inability to produce substantial yields of functionalised 3S-SPs means the PVA method remains the preferred choice of fabrication method for producing SP laser biosensors.

References

[1] B. K. Charlton, D. H. Downie, I. Noman, P. U. Alves, C. J. Eling, and N. Laurand, "Surface Functionalisation of Self-Assembled Quantum Dot Microlasers with a DNA Aptamer," *International Journal of Molecular Sciences*, vol. 24, p. 14416, 9 2023.

[2] O. Elimelech, O. Aviv, M. Oded, and U. Banin, "A Tale of Tails: Thermodynamics of CdSe Nanocrystal Surface Ligand Exchange," *Nano Letters*, vol. 20, no. 9, pp. 6396–6403, 2020.

[3] Y. Zhang and A. Clapp, "Overview of Stabilizing Ligands for Biocompatible Quantum Dot Nanocrystals," *Sensors*, vol. 11, no. 12, pp. 11036–11055, 2011.

[4] J. Aldana, N. Lavelle, Y. Wang, and X. Peng, "Size-dependent dissociation pH of thiolate ligands from cadmium chalcogenide nanocrystals," *Journal of the American Chemical Society*, vol. 127, no. 8, pp. 2496–2504, 2005.

[5] M. Bäumle, D. Stamou, J.-M. Segura, R. Hovius, and H. Vogel, "Highly Fluorescent Streptavidin-Coated CdSe Nanoparticles: Preparation in Water, Characterization, and Micropatterning," *Langmuir*, vol. 20, no. 10, pp. 3828–3831, 2004.

[6] M. Stanisavljevic, L. Janu, K. Smerkova, S. Krizkova, N. Pizurova, M. Ryvolova, V. Adam, J. Hubalek, and R. Kizek, "Study of streptavidin-modified quantum dots by capillary electrophoresis," *Chromatographia*, vol. 76, no. 7-8, pp. 335–343, 2013.

[7] A. George, H. K. Choudhary, B. Satpati, and S. Mandal, "Synthesis, characterization and optical properties of ligand-protected indium nanoparticles," *Physical Chemistry Chemical Physics*, vol. 17, pp. 7109–7113, 3 2015.

[8] N. Bel Haj Mohamed, M. Haouari, Z. Zaaboub, F. Hassen, H. Maaref, and H. Ben Ouada, "Effect of surface on the optical structure and thermal properties of organically capped CdS nanoparticles," *Journal of Physics and Chemistry of Solids*, vol. 75, no. 8, pp. 936–944, 2014.

[9] A. Sabah, S. Tasleem, M. Murtaza, M. Nazir, and F. Rashid, "Effect of Polymer Capping on Photonic Multi-Core–Shell Quantum Dots CdSe/CdS/ZnS: Impact of Sunlight and Antibacterial Activity," *The Journal of Physical Chemistry C*, vol. 124, no. 16, pp. 9009–9020, 2020.

[10] X. Qian, J. Li, and X. Peng, "a Liquid-Phase Infrared Strategy for Quantification of Surface Alkanoate Ligands on Colloidal Nanocrystals," *Chemistry of Materials*, vol. 34, pp. 7006–7014, 8 2022.

[11] J. A. Schott, C.-L. Do-Thanh, W. Shan, N. G. Puskar, S. Dai, and S. M. Mahurin, "FTIR investigation of the interfacial properties and mechanisms of CO2 sorption in porous ionic liquids," *Green Chemical Engineering*, vol. 2, no. 4, pp. 392–401, 2021.

[12] N. Singh, S. Prajapati, Prateek, and R. K. Gupta, "Investigation of Ag doping and ligand engineering on green synthesized CdS quantum dots for tuning their optical properties," *Nanofabrication*, vol. 7, pp. 89–103, 2022.

[13] N. T. Vo, H. D. Ngo, N. P. Do Thi, K. P. Nguyen Thi, A. P. Duong, and V. Lam, "Stability Investigation of Ligand-Exchanged CdSe/ZnS-Y (Y = 3-Mercaptopropionic Acid or Mercaptosuccinic Acid) through Zeta Potential Measurements," *Journal of Nanomaterials*, vol. 2016, pp. 1–8, 2016.

[14] V. Bharathi M., N. Roy, P. Moharana, K. Ghosh, and P. Paira, "Green synthesis of highly luminescent biotin-conjugated CdSe quantum dots for bioimaging applications," *New Journal of Chemistry*, vol. 44, no. 39, pp. 16891–16899, 2020.

[15] A. S. Karakoti, R. Shukla, R. Shanker, and S. Singh, "Surface functionalization of quantum dots for biological applications," *Advances in Colloid and Interface Science*, vol. 215, pp. 28–45, 2015.

[16] K. X. Tan, S. Ujan, M. K. Danquah, and S. Y. Lau, "Design and characterization of a multi-layered polymeric drug delivery vehicle," *Canadian Journal of Chemical Engineering*, vol. 97, pp. 1243–1252, 6 2019.

[17] M. C. Estévez, M. B. O'Donoghue, X. Chen, and W. Tan, "Highly fluorescent dye-doped silica nanoparticles increase flow cytometry sensitivity for cancer cell monitoring," *Nano Research*, vol. 2, pp. 448–461, 6 2009.

[18] A. Jain, A. Barve, Z. Zhao, W. Jin, and K. Cheng, "Comparison of Avidin, Neutravidin, and Streptavidin as Nanocarriers for Efficient siRNA Delivery," *Molecular Pharmaceutics*, vol. 14, pp. 1517–1527, 5 2017.

[19] A. Plunkett, C. Eldridge, G. A. Schneider, and B. Domènech, "Controlling the Large-Scale Fabrication of Supraparticles," *The Journal of Physical Chemistry B*, vol. 124, no. 49, pp. 11263–11272, 2020.

[20] W. Chen, L. Wang, R. Liu, H. Shen, J. Du, and F. Fan, "Self-Assembled and Wavelength-Tunable Quantum Dot Whispering-Gallery-Mode Lasers for Backlight Displays," *Nano Letters*, vol. 23, no. 2, pp. 437–443, 2023.

[21] F. Montanarella, J. J. Geuchies, T. Dasgupta, P. T. Prins, C. van Overbeek, R. Dattani, P. Baesjou, M. Dijkstra, A. V. Petukhov, A. van Blaaderen, and

D. Vanmaekelbergh, "Crystallization of Nanocrystals in Spherical Confinement Probed by in Situ X-ray Scattering," *Nano Letters*, vol. 18, no. 6, pp. 3675–3681, 2018.

[22] J. Wang, E. Kang, U. Sultan, B. Merle, A. Inayat, B. Graczykowski, G. Fytas, and N. Vogel, "Influence of Surfactant-Mediated Interparticle Contacts on the Mechanical Stability of Supraparticles," *The Journal of Physical Chemistry C*, vol. 125, no. 42, pp. 23445–23456, 2021.

[23] X.-C. Yu, S.-J. Tang, W. Liu, Y. Xu, Q. Gong, Y.-L. Chen, and Y.-F. Xiao, "Single-molecule optofluidic microsensor with interface whispering gallery modes," *Proceedings of the National Academy of Sciences*, vol. 119, no. 6, p. e2108678119, 2022.

[24] F. Vollmer and D. Yu, "Single-Molecule Sensing," in *Optical Whispering Gallery Modes for Biosensing: From Physical Principles to Applications* (B. S. F. I. U. Gerstman, ed.), Biological and Medical Physics, Biomedical Engineering, ch. 5, pp. 233–298, Cham: Springer International Publishing, 1 ed., 2020.

[25] J. Choi, W. Choi, and D. Y. Jeon, "Ligand-Exchange-Ready CuInS2/ZnS Quantum Dots via Surface-Ligand Composition Control for Film-Type Display Devices," *ACS Applied Nano Materials*, vol. 2, no. 9, pp. 5504–5511, 2019.

[26] P. Li, C. Luo, X. Chen, and C. Huang, "An off-on fluorescence aptasensor for trace thrombin detection based on FRET between CdS QDs and AuNPs," *RSC Advances*, vol. 12, no. 55, pp. 35763–35769, 2022.

[27] Y. Ji, X. Yang, Z. Ji, L. Zhu, N. Ma, D. Chen, X. Jia, J. Tang, and Y. Cao, "DFT-Calculated IR Spectrum Amide I, II, and III Band Contributions of N-Methylacetamide Fine Components," *ACS Omega*, vol. 5, no. 15, pp. 8572–8578, 2020.

[28] Y. H. Lao, C. W. Chi, S. M. Friedrich, K. Peck, T. H. Wang, K. W. Leong, and L. C. Chen, "Signal-on Protein Detection via Dye Translocation between Aptamer and

Quantum Dot," *ACS Applied Materials and Interfaces*, vol. 8, no. 19, pp. 12048–12055, 2016.

[29] Marcel J. E. Fischer, "Amine Coupling Through EDC/NHS: A Practical Approach," in *Surface Plasmon Resonance: Methods and Protocols* (N. J. Mol and M. J. E. Fischer, eds.), vol. 627 of *Methods in Molecular Biology*, ch. Amine Coup, pp. 55–73, New Jersey: Humana Totowa, 1 ed., 2010.

[30] Q. Zhang, R.-X. Li, X. Chen, X.-X. He, A.-L. Han, G.-Z. Fang, J.-F. Liu, and S. Wang, "Study of Efficiency of Coupling Peptides with Gold Nanoparticles," *Chinese Journal of Analytical Chemistry*, vol. 45, pp. 662–667, 5 2017.

[31] L. Cai, J. Pan, Y. Zhao, J. Wang, and S. Xiao, "Whispering Gallery Mode Optical Microresonators: Structures and Sensing Applications," *Physica Status Solidi (A) Applications and Materials Science*, vol. 217, no. 6, pp. 1–18, 2020.

[32] M. Bhowmick, B. Ullrich, M. Murchland, X. Zhou, and C. Ramkumar, "Substrate and Excitation Intensity Dependence of Saturable Absorption in Perovskite Quantum Dot Films," *Nanomaterials*, vol. 13, p. 871, 2 2023.

[33] C. J. Eling, N. Bruce, N.-K. Gunasekar, P. U. Alves, P. R. Edwards, R. W. Martin, and N. Laurand, "Biotinylated Photocleavable Semiconductor Colloidal Quantum Dot Supraparticle Microlaser," *ACS Applied Nano Materials*, vol. 7, no. 8, pp. 9159–9166, 2024.

[34] A. Francois and M. Himmelhaus, "Whispering gallery mode biosensor operated in the stimulated emission regime," *Applied Physics Letters*, vol. 94, no. 3, pp. 1–4, 2009.

Chapter 5

Biosensing

5.1 Overview

After successful surface functionalisation of SP lasers, the natural progression is to test whether these materials can be used as biosensors. Before biosensing tests could be undertaken, a dedicated optical setup was built to be able to obtain PL spectra from SP samples placed on a horizontal surface so solutions could be placed on top of the SPs. The optical setup is described and characterisation of the incoming pump laser beam to be able to calculate pump fluence is detailed. Using SPs functionalised with the aptamer TBA-15, biosensing experiments were carried out with four different concentrations of BSA and Thrombin to test the selectivity and sensing capabilities of these lasers.

5.2 Optical Setup and Characterisation

As biosensing tests requires the SPs to be submerged in liquid, a dedicated optical setup needed to be built to be able to carry out sensing tests on a horizontal surface to allow solutions to be placed on top of the SP sample. Using small volume cuvettes to be able to do this on the main PL setup was considered, however SPs need to be fixed to be able to confidently pump the same SP over time and this dedicated setup allows SPs to be more spread out to make it easier to find single SPs. Figure 5.1 is an image of this optical setup built for this experiment. The blue line shows the direction of the pump laser beam as the beam is directed into a dichroic mirror, reflected into a 10x objective lens to focus the beam onto the sample stage. A small piece of polished silicon wafer was attached to the sample stage to reflect as much SP signal as possible back in to the objective lens to be collected. The sample signal is directed through the dichroic mirror, through a 50 mm focus lens, a long pass filter to filter out the remaining pump laser beam, and into the optical fibre mount. To aid with alignement, the optical fibre mount was placed within an xyz cage translation stage. As this is a cage setup, the beam profiler to measure the beam spot size of the pump laser was too big to fit under the objective lens, so to find the beam spot size and focus point of the pump laser, knife edge measurements were carried out. Figure 5.2 is a schematic of the basic setup used for knife edge measurements. A razor blade was used and was mounted to the stage and moved through the z direction to determine where the focus of the laser beam was. At each z position, the blade was moved through the x direction and power readings were taken to create a power profile of the laser beam at each z position, which can be fitted to the following equation

$$P(x,z) = p(z) \int_{0}^{\infty} \exp\left[\frac{-2\left(x-x_0\right)^2}{\left(w(z)\right)^2}\right] \tag{5.1}$$

$$= \frac{P_0}{2} \operatorname{erfc}\left[\frac{\sqrt{2}\left(x-x_0\right)^2}{w(z)}\right] \tag{5.2}$$

where erfc is the following complementary error function:

$$p(z) = \sqrt{\frac{\pi}{2}} I_0 \frac{{w_0}^2}{w(z)} \tag{5.3}$$

$$P_0 = \frac{\pi}{2} I_0 {w_0}^2 \tag{5.4}$$

Fitting the beam profiles is done to measure the beam radius, $w(z)$, at each z position to create a radius profile of the incoming laser beam to find the position the stage needs to be in for the sample to be at the beam focus, z_0, and the beam waist radius, w_0.

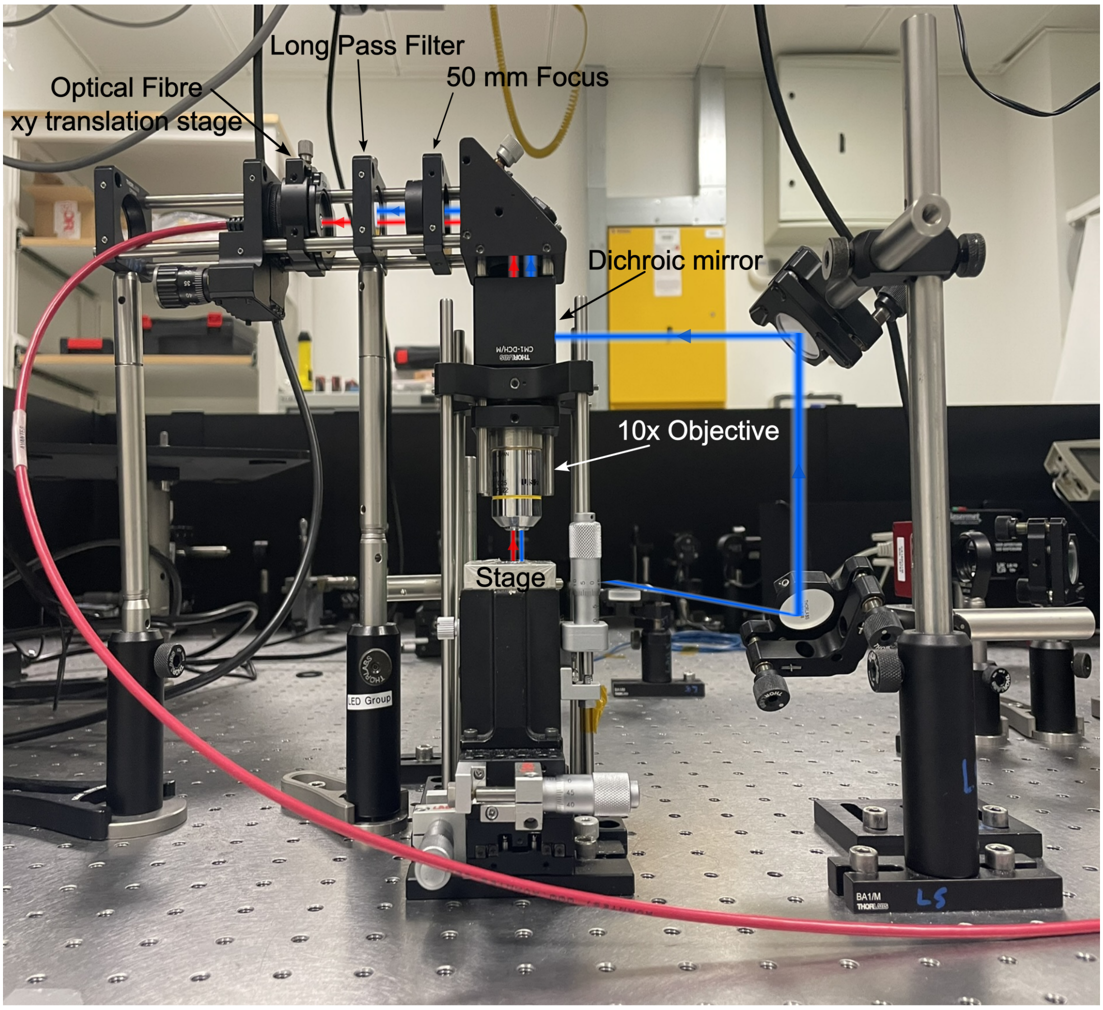

Figure 5.1: Image of the optical setup built for biosensing with the different optics and beam directions labelled. The cover of the periscope has been removed for this picture.

This profile can then be fitted to the following expression for $w(z)$

$$w(z) = w_0\sqrt{1 + \left(\frac{M^2\lambda(z - z_0)}{\pi {w_0}^2}\right)^2} \tag{5.5}$$

The resulting beam radius profile from the knife edge measurements for this setup is shown in Figure 5.3. P_0 was set at 225 ± 4 nJ and λ was 355 nm. From the beam waist profile, z_0 was measured to be at 7.96 mm, and w_0 was found to be $2.0 \pm 0.9 \times 10^{-3}$ cm, therefore the beam spot size could be calculated to be $1.32 \pm 0.25 \times 10^{-5}$ cm^2. The M^2 value which indicates the beam quality and divergence can also be determined from the fit of the radius profile, and this was found to be 5.6 ± 1.2.

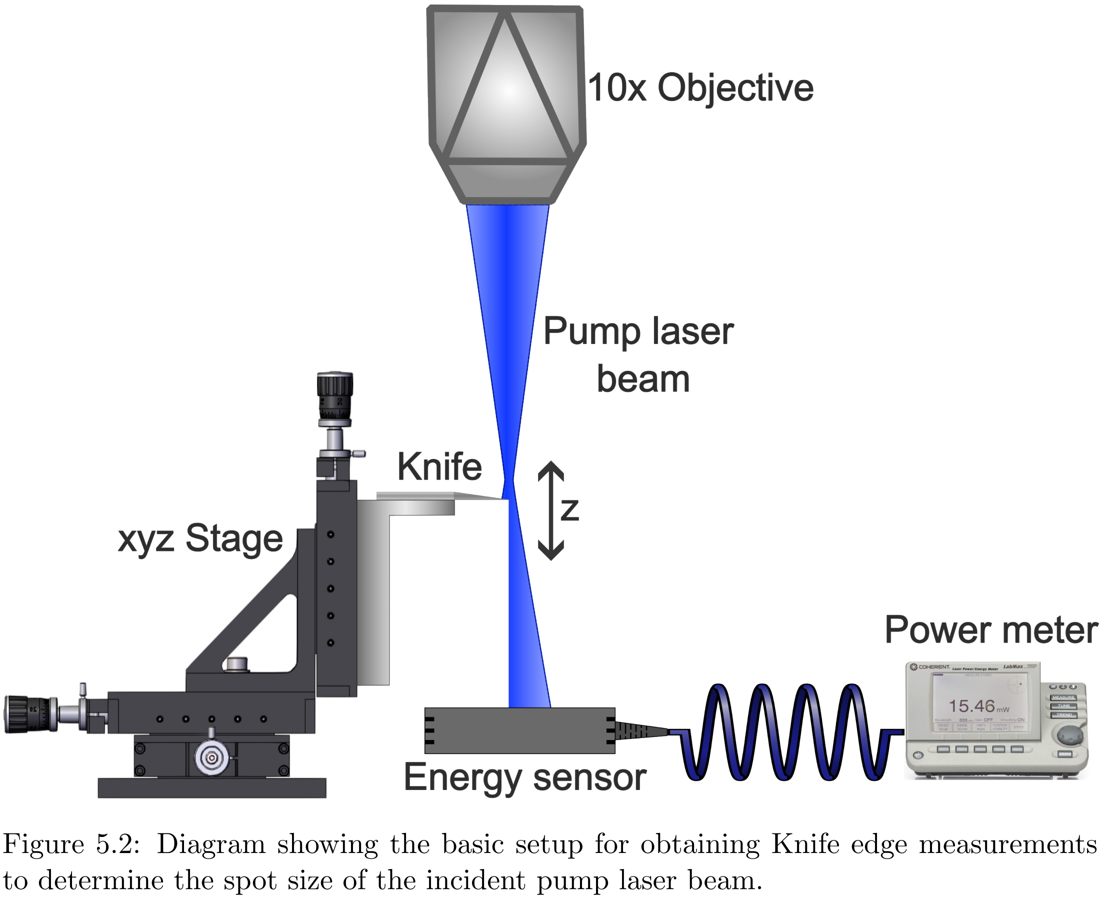

Figure 5.2: Diagram showing the basic setup for obtaining Knife edge measurements to determine the spot size of the incident pump laser beam.

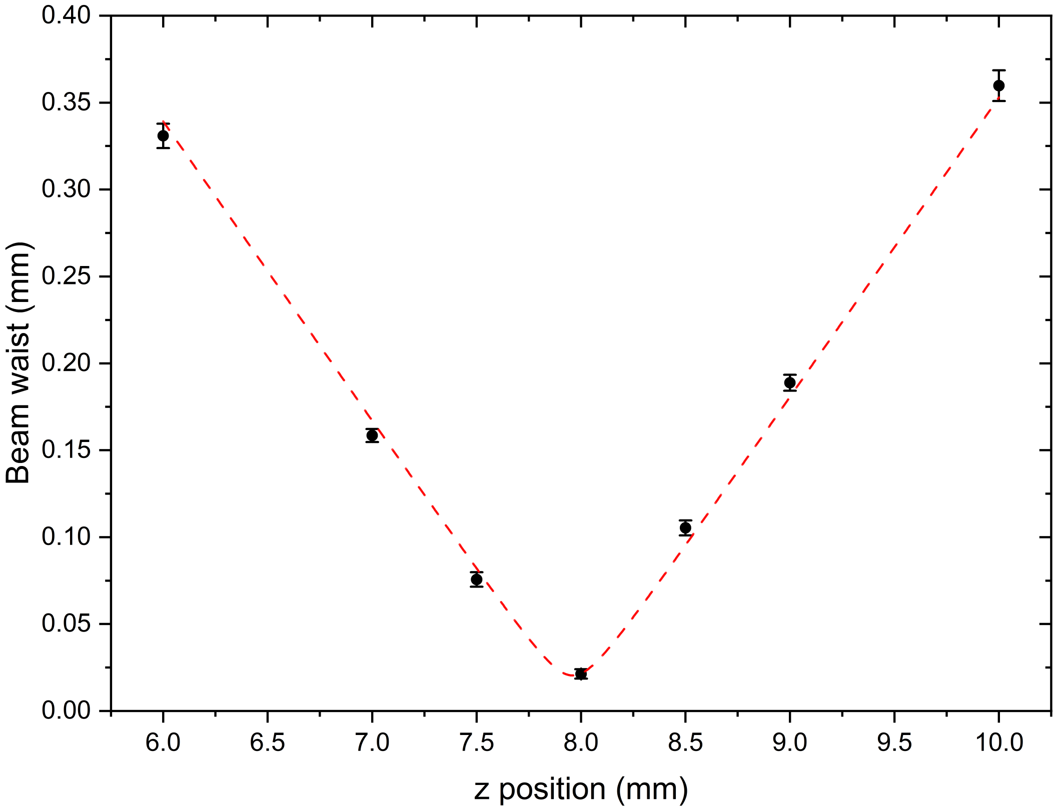

Figure 5.3: Beam waist measurements at each z position and fit used to calculate the beam spot size for the biosensing setup. Incident laser beam was assumed to be perfectly circular so beam waist measurements were taken for the x axis only.

5.3 Thrombin Sensing

Thrombin sensing with TBA-capped SPs was trialled to obtain proof of concept data to determine whether these lasers could feasibly be used as biosensors. SP samples were cast on glass microscope slides and left to dry. SPs were found to readily stick to glass slides when dried and could not easily be rinsed away with water, possibly due to hydrogen bonding between the aptamer molecules attached to the SPs and the glass. 10 µL of water was added on top of the SP sample while attached to the stage to be able to keep the sample positioning consistent. Finding a suitable lasing SP with good signal before adding water did not produce stable results, so finding a suitable SP laser was done while the sample was covered in water. To account for evaporation of the water, 10 µL was continually added to make sure the SPs did not completely dry. Once a suitable

SP was found, measurements were taken every 5 minutes in water to find a baseline, then 10 µL of BSA solution was added and measurements taken every 5 minutes for up to 25 minutes. 10 µL of Thrombin solution of the same concentration as the BSA used was subsequently added and measurements taken every minute, where possible and 5 minutes if not, for up to 1 hour. This was due to the spectrometer integration time sometimes needing to be altered for some TBA-SPs where the laser signal strength needed to be increased to be able to more easily track any wavelength shifts. 10 µL water was added as required to avoid the protein solutions drying on the SPs as signal recovery after drying was not possible, particularly at the higher concentrations. This issue of solution evaporation will not be a problem for SPs integrated into a microfluidic chip due to the continuous flow of solution that will be possible with this design, and the size of the channels should be small enough to reduce this effect on the laser signal as much as possible. OA-SPs were also tested with the same concentrations of BSA and Thrombin to be able to compare the observed peak shifts to determine if TBA-SPs are successful biosensors. BSA was tested with the SPs before Thrombin to be able to test the specificity of the TBA-SPs and account for any non-specific binding that may occur during sensing runs. [1–3] These BSA runs are also important for testing whether reference samples could be used for being able to detect target analytes in more complex solutions, such as blood samples. [4]

Results of the sensing tests are shown in Table 5.1 and Figure 5.4. Figure 5.4 shows

Table 5.1: Table showing the wavelength shifts, shown visually in Figure 5.6, in nm for OA- and TBA-coated SPs over each stage of the sensing experiments at each protein concentrations. Beginning in water, then BSA solution, and finally finishing with the Thrombin solution.

Protein Conc.	1.5 mg/mL		10 mg/mL		15 mg/mL	
Medium	OA-SP	TBA-SP	OA-SP	TBA-SP	OA-SP	TBA-SP
H_2O	−0.4	−0.5	−0.2	−0.8	−0.4	+0.1
BSA	−0.4	−1.0	−0.9	−0.9	−0.2	+0.8
Thrombin	−0.4	−0.6	−1.7	+4.4	+0.3	+2.3

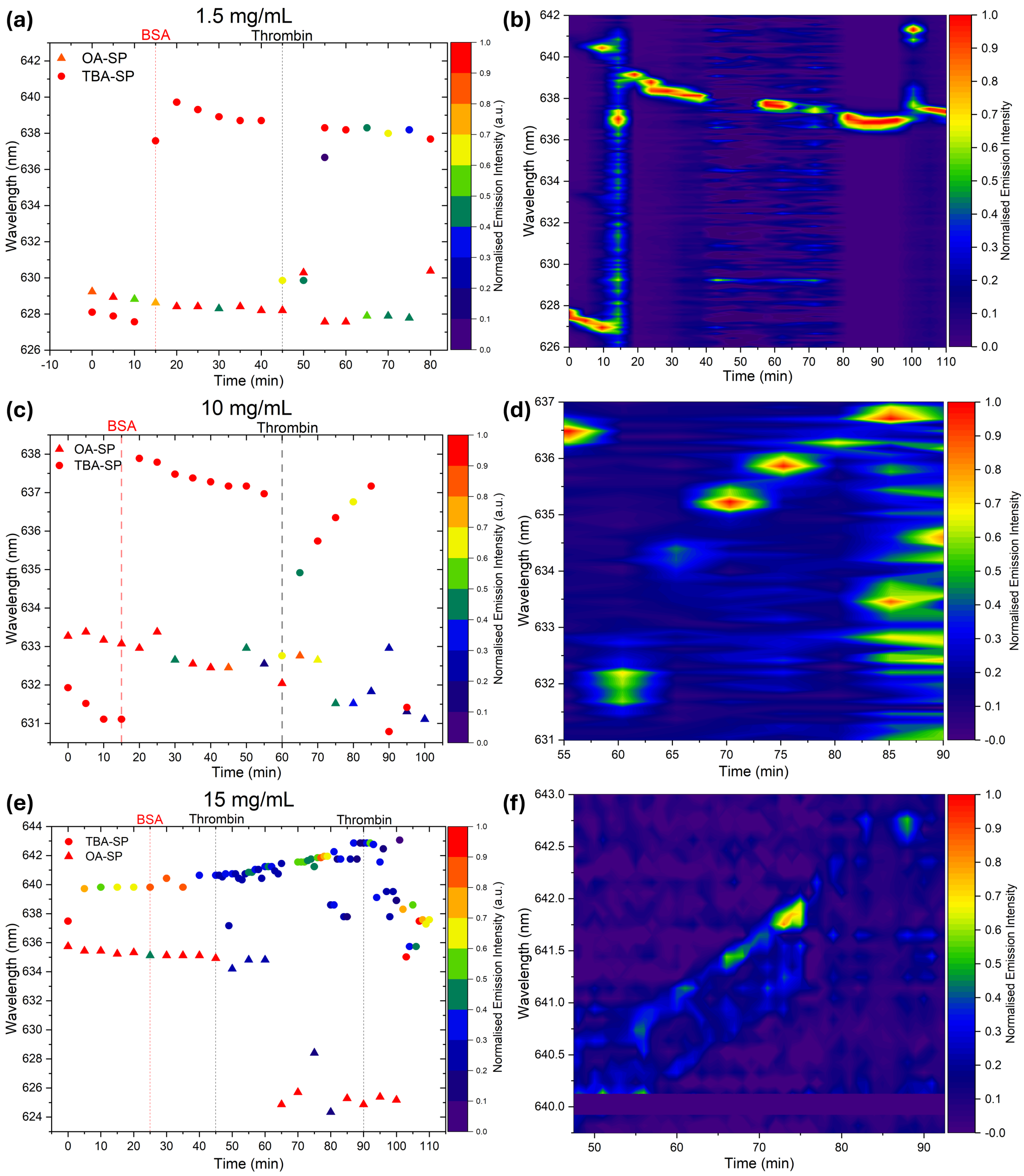

Figure 5.4: Plots tracking the wavelength change over time for OA- and TBA-SPs after the addition of BSA and Thrombin solutions with concentrations of 1.5 mg/mL (a,b), 10 mg/mL (c,d), and 15 mg/mL (e,f). Left (a,c,e) are plots of the wavelength of the peak with the highest emission against the time elapsed for OA- and TBA-SPs with the time of BSA and Thrombin additions marked. Right (c,d,f) are the corresponding contour maps of the TBA-SP emission spectra.(d,f) shows the contour map only after Thrombin addition for clarity.

plots of the dominant laser peak wavelength over time for TBA- and OA-SPs and the corresponding contour plots extracted from the spectra taken for the TBA-SP. The red and black dashed lines on the peak wavelength plots notate when the BSA and Thrombin solutions were added, respectively. Table 5.1 shows the overall wavelength shifts of OA- and TBA-SPs shown in Figure 5.4 when exposed to the three different media: water, BSA solution, and Thrombin solution. Samples were pumped at fluences low enough to prevent SP degradation over time while also producing a strong enough laser signal to be able to detect any wavelength shifts. For OA-SPs this pump fluence was lower due to their superior lasing ability with the SP used for 1.5 mg/mL and 10 mg/mL solutions pumped at 64.4 mJ/cm^2 and the SP used for 15 mg/mL solutions pumped at 76.8 mJ/cm^2. The TBA-SPs used for 1.5 mg/mL and 15 mg/mL solutions were pumped at 76.8 mJ/cm^2 and the TBA-SP used for the 10 mg/mL solutions was pumped at 93.5 mJ/cm^2. All SPs were still able to demonstrate lasing after over 100 minutes, however this was not with continuous laser pumping as between obtaining each spectra the pump laser safety shutter was closed to attempt to protect the SPs as much as possible.

As shown in Figure 5.4, there was only significant redshifts observed for Thrombin solutions with concentrations of 10 and 15 mg/mL, with only blueshifts being seen for the majority of the other SPs in the different media. There are small redshifts seen for the OA-SP after Thrombin addition and the TBA-SP at all stages of the experiment with the 15 mg/mL solution, which could be due to local environmental changes or non-specific binding. The comparison of wavelength shifts seen in TBA-SPs after BSA and Thrombin addition in addition to the comparison with OA-SPs means we can conclude the significant redshifts, in the order of nm, observed after addition of 10 and 15 mg/mL solutions is due to the binding of Thrombin to the SP surface, therefore these SPs could be used as laser biosensors. These redshifts were observed in 40 minutes or less, which is a promising timescale for producing sensing devices for rapid diagnoses. However, this is initial data for a proof of concept study and tests with many more solution concentrations with repeats need to be carried out to determine the limit of detection by plotting the wavelength shifts against Thrombin concentrations. More readings of wavelength shifts for more concentrations could also be used to test if these sensors could produce a calibration curve so a quantitative value for analyte concentrations could be determined for complex samples. Due to the difficulty of finding TBA-SPs with stable detectable signals in the water, the single SPs were selected based on their signal which is why the SPs are lasing at different wavelengths. There are also sudden jumps in the wavelength after the addition of BSA (Fig. 5.4a-d) compared to SPs just in water, which could be due to a change in refractive index between just water and water containing protein. [2, 5] Sudden jumps in wavelength for SPs between BSA and Thrombin addition may have been due to sample evaporation, which would be solved if SPs were integrated within a microfluidic chip. Other causes of the sudden wavelength jumps could also be alterations in temperature and mode hopping between the different modes which can lase. The sensitivity of these SP lasers may be difficult to improve until the cause of the observed blueshift is investigated, as it is possible the SPs tested with the lower protein concentrations are detecting Thrombin however the redshift caused by the addition of Thrombin to the SP surface is competing with the possible effects causing blueshift, such as refractive index change from the different protein solutions [6], temperature fluctuations due to laser heating effects [7, 8], cavity degradation [9], and in some cases even the substrate the WGM cavity is attached to [10, 11], and at higher protein concentrations there is enough surface binding for the redshift to 'win out' and become observable. [12] Photocorrosion is another factor which could be causing this anomalous blueshift as CQDs can act as photocatalysts in liquid, leading to ligand loss and therefore photocorrosion or photooxidation, reducing the refractive index at the SP surface which would manifest as a blueshift. [13] The wavelength shifts of the SP lasers can also indicate the level of undesirable non-specific binding and the desired specific binding as the shift observed depends on the number of binding sites filled by an analyte. [14] Table 5.1 shows that for lower concentrations, the observed wavelength shifts are very small for BSA solutions, indicating the levels of non-specific binding are low. This bodes well for the suitability of these TBA-SPs for biological samples without requiring time consuming sample preparation.

Slight blueshifts could be seen in the spectra for SPs tested with Thrombin con-

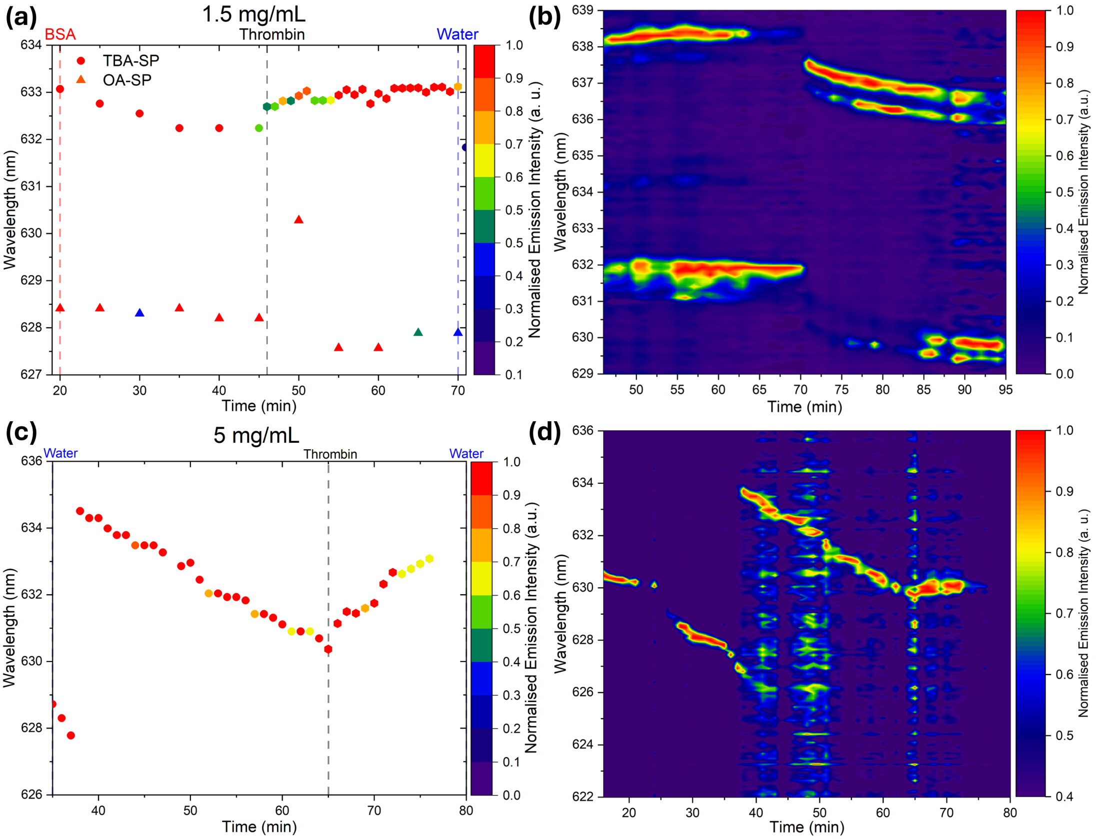

Figure 5.5: (a,b) Plot tracking the wavelength change over time for OA- and TBA-SPs after the addition of BSA and Thrombin solutions with concentrations of 1.5 mg/mL and the corresponding contour plot of the spectra taken after Thrombin addition, without any baseline correction. (c,d) Plot tracking the wavelength change over time for the TBA-SP tested with 5 mg/mL BSA and Thrombin solutions and the corresponding contour plot of the spectra taken after Thrombin addition, without baseline correction.

centrations of 1.5 mg/mL and 5 mg/mL (Appendix A.3, Figures A.1 and A.2), with constant degradation blueshifts demonstrated by the SPs in water and BSA solutions. To see if there was a sensing response ‘hidden’ behind the blueshift present due to degradation, the degradation shift was used as a baseline and subtracted from the SP laser response after thrombin addition. These plots of the wavelength shift over time with the baseline corrected shifts are shown in Fig 5.5. For 1.5 mg/mL, the shift used for the baseline was after BSA addition between t $= 20-40$ mins, and for the 5 mg/mL the baseline was taken as the linear blueshift after the mode hopping to 635 nm between t = 40−64 mins. After the baseline correction, there are redshifts of 2.7 nm and 0.4 nm for 5 mg/mL and 1.5 mg/mL Thrombin concentrations respectively, which is a dramatic improvement in the sensitivity of these SP biosensors. The small redshift of 0.4 nm observed with a Thrombin concentration of 1.5 mg/mL possibly indicates this is relatively close to the limit of detection, given the current setup. Even with this improvement, this is not comparable to the current state of the art detection limits of WGM resonator-based biosensors which have demonstrated detection limits at micro-, nano-, and femtogram scales. [15–17]

5.4 Future Work

As there are only a small number of initial results reported above, much more study is required to fully verify whether these lasers were successfully detecting thrombin binding to the SP surface. Before anything else, the experimental setup should be improved by creating a very simple microfluidic chip with a chamber containing SPs to be measured. This can be done by using a mould to produce a PDMS layer containing an inlet and an outlet channel with a chamber in the centre which can be fused to the surface of a glass slide. A 3D printed mould could be used to cure PDMS over the top and create the shape for the microfluidic chip. Ozone plasma treatment of both the PDMS and the glass slide would then be used to be able to fuse the two materials together and create the final chip. A very simple and easy to produce setup like this would solve problems with solution evaporation and keep SPs fully immersed in solution throughout the experiments and allow for real time monitoring of the laser wavelengths while solutions are altered. Alongside this, refractive index sensing could first be trialled by tracking the laser peak wavelength of a single SP while immersed in different solvents and sequentially adjusting the solvent dilution ratio to alter the refractive index of the SP environment. The laser peak wavelength would be plotted against the refractive index of the solutions the SPs are immersed in to demonstrate the response to local refractive index changes to gauge whether there is a response to refractive index alterations and prove whether SPs are suitable for continuing with further sensing experiments.

To be able to fully assess the suitability of SP lasers for the sensing of thrombin, more experiments need to be carried out with suitable blank solutions to compare the signal response of the SPs with that of thrombin solutions. A suitable buffer solution for the blank and protein solution which does not dissolve the SPs must also be found and the binding kinetics of thrombin to the laser surface should be calculated, as these are important parameters to understand when undergoing sensing tests. Sensitivity of the SPs would also be determined by plotting the wavelength shift against the concentration of target analyte after running more experiments with different thrombin concentrations. This could also be used to create a calibration curve to be able to test whether SPs could also be used to not only detect proteins, but also for determining the concentration of analyte within solution. Testing different conditions to find the optimal environmental conditions for sensing and being able to properly calculate the sensitivity of the SP biosensors will be very important to be able to critically analyse how these SPs compare to the current commercial laboratory sensing methods for thrombin. Shifting the focus from thrombin as a target analyte to interrogate other clinically relevant biomolecules, such as VEGF or micro-RNA may also be beneficial for future work on these SP lasers.

5.5 Conclusion

In summary, TBA-capped CQD SP lasers have possibly demonstrated biosensing capabilities for the protein Thrombin. Redshifts were observed in 40 minutes or less in TBA-SPs after the addition of Thrombin solutions with concentrations as low as 1.5 mg/mL, implying successful selective binding of Thrombin to the surface of the SP lasers, increasing the effective diameter of the SPs and the path length of the resonating light, inducing the redshift observed. As highlighted above, more study is required to be able to definitively show specific binding of Thrombin to the SP surface. The limit of detection for these SP laser biosensors, likely limited by the current crude set-up, is estimated to be around 1.5 mg/mL which leaves much to be desired and requires much further study, particularly into the cause of the anomalous blueshifts observed with lower concentrations of Thrombin. Once the cause of this phenomenon is identified and understood, the detection limit of these laser biosensors could be significantly improved to approach the reported sensitivity of other WGM laser biosensors. [4,9,18–20] It is important to note the current commercial methods for detecting and measuring thrombin involve continuously measuring thrombin production in a plasma sample, usually by tracking signal response from thrombin displacing a substrate and can detect thrombin concentrations at the µg/mL scale with scan times of up to 120 minutes in samples as small as 100 µL, however these methods require sample pretreatment to generate platelet poor plasma to remove interferents. [21] As detailed above, there is much more work to be done with these lasers and after thrombin sensing is demonstrated with a calibration curve produced, these SPs could be able to produce measurements for thrombin concentration in less time than the current commercially available scans. Other future work would include integrating these SP laser biosensors into a microfluidic chip and to simplify signal analysis of these devices, smaller SP sizes should be used to minimise the number of detectable lasing modes while also improving sensitivity as a result of the increased surface to volume ratio. It is possible to design microfluidic chips with multiple channels to be able to inject multiple different solutions to be able to easily test against multiple reference solutions and biological samples. [22–24] Design and manufacture of a microfluidic chip suitable for carrying out biosensing tests similar to the simple test detailed in this work has been reported using a simple fabrication process of curing PDMS over a resin mould and fusing the subsequent microfluidic cell to a glass slide. [25] Transfer printing has also developed enough to be able to pick and place single SPs onto substrates which would enable single SPs to be placed and integrated into such microfluidic chips. [26] SP laser biosensors could also be trialled with different target analytes, such as VEGF which controls blood vessel formation and is not easily detectable [1], or any other disease markers that have a suitable aptamer within the size limitations needed for sensing within the evanescent field of the WGM modes. Micro RNA detection could also be trialled with aptamer functionalised SP laser biosensors as being able to quickly and reliably detect the presence of abnormal RNA is garnering huge interest for the early detection and monitoring of certain cancers. [27]

References

[1] L. Pasquardini, S. Berneschi, A. Barucci, F. Cosi, R. Dallapiccola, M. Insinna, L. Lunelli, G. N. Conti, C. Pederzolli, S. Salvadori, and S. Soria, "Whispering gallery mode aptasensors for detection of blood proteins," *Journal of Biophotonics*, vol. 6, no. 2, pp. 178–187, 2013.

[2] G. Nunzi Conti, S. Berneschi, and S. Soria, "Aptasensors Based on Whispering Gallery Mode Resonators," *Biosensors*, vol. 6, no. 3, p. 28, 2016.

[3] H. Zhu, J. D. Suter, I. M. White, and X. Fan, "Aptamer based microsphere biosensor for thrombin detection," *Sensors*, vol. 6, pp. 785–795, 8 2006.

[4] T. Reynolds, A. François, N. Riesen, M. E. Turvey, S. J. Nicholls, P. Hoffmann, and T. M. Monro, "Using whispering gallery mode micro lasers for biosensing within undiluted serum," in *SPIE BioPhotonics Australasia* (M. R. Hutchinson and E. M. Goldys, eds.), vol. 10013, p. 100132X, SPIE, 2016.

[5] H. Zhao, P. H. Brown, and P. Schuck, "On the Distribution of Protein Refractive Index Increments," *Biophysical Journal*, vol. 100, pp. 2309–2317, 5 2011.

[6] M. Humar and S. H. Yun, "Whispering-gallery-mode emission from biological luminescent protein microcavity assemblies," *Optica*, vol. 4, p. 222, 2 2017.

[7] M. Loyez, M. Adolphson, J. Liao, and L. Yang, "From Whispering Gallery Mode Resonators to Biochemical Sensors," *ACS Sensors*, vol. 8, no. 7, pp. 2440–2470, 2023.

[8] F. Vollmer and D. Yu, "Single-Molecule Sensing," in *Optical Whispering Gallery Modes for Biosensing: From Physical Principles to Applications* (B. S. F. I. U. Gerstman, ed.), Biological and Medical Physics, Biomedical Engineering, ch. 5, pp. 233–298, Cham: Springer International Publishing, 1 ed., 2020.

[9] M. R. Foreman, J. D. Swaim, and F. Vollmer, "Whispering gallery mode sensors," *Advances in Optics and Photonics*, vol. 7, no. 2, p. 168, 2015.

[10] F. Azeem, L. S. Trainor, P. A. Devane, D. S. Norman, A. Rueda, N. J. Lambert, M. Kumari, M. R. Foreman, and H. G. L. Schwefel, "Dielectric perturbations: anomalous resonance frequency shifts in optical resonators," *Optics Letters*, vol. 46, no. 10, p. 2477, 2021.

[11] D. W. Vogt, A. H. Jones, H. G. L. Schwefel, and R. Leonhardt, "Anomalous blue-shift of terahertz whispering-gallery modes via dielectric and metallic tuning," *Optics Letters*, vol. 44, p. 1319, 3 2019.

[12] Z. Wang, Y. Zhang, X. Gong, Z. Yuan, S. Feng, T. Xu, T. Liu, and Y. C. Chen, "Bio-electrostatic sensitive droplet lasers for molecular detection," *Nanoscale Advances*, vol. 2, no. 7, pp. 2713–2719, 2020.

[13] N. Bruce, F. Farrell, and N. Laurand, "Temperature Stability of Elastomeric Colloidal Quantum Dot Colour Converter," in *2019 IEEE 2nd British and Irish Conference on Optics and Photonics (BICOP)*, pp. 1–4, IEEE, 2019.

[14] S. Arnold, R. Ramjit, D. Keng, V. Kolchenko, and I. Teraoka, "MicroParticle photophysics illuminates viral bio-sensing," *Faraday Discuss.*, vol. 137, pp. 65–83, 2008.

[15] S. Mostufa, B. Rezaei, S. Ciannella, P. Yari, J. Gómez-Pastora, R. He, and K. Wu, "Advancements and Perspectives in Optical Biosensors," *ACS Omega*, vol. 9, no. 23, pp. 24181–24202, 2024.

[16] B. Guan, T.-W. Kok, N. Riesen, D. Lancaster, K. Suu, and C. Priest, "Microsphere-Enabled Micropillar Array for Whispering Gallery Mode Virus Detection," *ACS Applied Materials & Interfaces*, vol. 16, no. 9, pp. 12042–12051, 2024.

[17] Y. Fu, S. Lin, and X.-H. Wang, "Whispering Gallery Mode Micro/Nanolasers for Intracellular Probing at Single Cell Resolution," *ACS Sensors*, vol. 9, no. 11, pp. 5683–5698, 2024.

[18] C. E. Soteropulos, K. M. Zurick, M. T. Bernards, and H. K. Hunt, "Tailoring the protein adsorption properties of whispering gallery mode optical biosensors," *Langmuir*, vol. 28, no. 44, pp. 15743–15750, 2012.

[19] X. Cao, Y. Luo, X. Liu, C. Shang, J. Lu, G. Song, and C. Deng, "Aptamer-thrombin loaded magnetic microspheres for bio-specific extraction and precise detection of hirudin," *Talanta*, vol. 267, no. August 2023, p. 125244, 2024.

[20] X.-C. Yu, S.-J. Tang, W. Liu, Y. Xu, Q. Gong, Y.-L. Chen, and Y.-F. Xiao, "Single-molecule optofluidic microsensor with interface whispering gallery modes," *Proceedings of the National Academy of Sciences*, vol. 119, no. 6, p. e2108678119, 2022.

[21] J. Kintigh, P. Monagle, and V. Ignjatovic, "A review of commercially available thrombin generation assays," *Research and Practice in Thrombosis and Haemostasis*, vol. 2, pp. 42–48, 1 2018.

[22] M. Charlebois, A. Paquet, L. S. Verret, K. Boissinot, M. Boissinot, M. G. Bergeron, and C. N. Allen, "Toward Automatic Label-Free Whispering Gallery Modes Biodetection with a Quantum Dot-Coated Microsphere Population," *Nanoscale Research Letters*, vol. 5, no. 3, pp. 524–532, 2010.

[23] T. Wienhold, S. Kraemmer, S. F. Wondimu, T. Siegle, U. Bog, U. Weinzierl, S. Schmidt, H. Becker, H. Kalt, T. Mappes, S. Koeber, and C. Koos, "All-polymer photonic sensing platform based on whispering-gallery mode microgoblet lasers," *Lab on a Chip*, vol. 15, no. 18, pp. 3800–3806, 2015.

[24] B. C. Paulus, J. K. Banh, K. D. Rector, B. W. Stein, and L. M. Lilley, "Whispering gallery mode resonators in continuous flow: spectral assignments and sensing with monodisperse microspheres," *Analytical Methods*, vol. 14, no. 17, pp. 1690–1697, 2022.

[25] X. Ouyang, T. Liu, Y. Zhang, J. He, Z. He, A. P. Zhang, and H. Y. Tam, "Ultrasensitive optofluidic enzyme-linked immunosorbent assay by on-chip integrated

polymer whispering-gallery-mode microlaser sensors," *Lab on a Chip*, vol. 20, no. 14, pp. 2438–2446, 2020.

[26] P. U. Alves, B. J. E. Guilhabert, J. R. McPhillimy, D. Jevtics, M. J. Strain, M. Hejda, D. Cameron, P. R. Edwards, R. W. Martin, M. D. Dawson, and N. Laurand, "Waveguide-Integrated Colloidal Nanocrystal Supraparticle Lasers," *ACS Applied Optical Materials*, vol. 1, pp. 1836–1846, 11 2023.

[27] C. S. Martins, A. P. Lagrow, and J. A. Prior, "Quantum Dots for Cancer-Related miRNA Monitoring," *ACS Sensors*, vol. 7, no. 5, pp. 1269–1299, 2022.

Chapter 6

Conclusion

Self assembled SP lasers consisting entirely of CQDs are a novel class of laser material with lots of promise for a variety of different applications. In this thesis, the focus was on their possible applications as laser biosensors which could be integrated into a lab on a chip sensing device. Although CQD SP lasers were only first reported in 2018, there have already been a number of different variations of the emulsion used to fabricate these SPs reported. Three different variants of the emulsion templated self-assembly used to fabricate SPs were trialled: using poly(vinyl alcohol) (PVA) as a surfactant, three different surfactants (3S), and no surfactants at all (SF). The 3S and SF methods were found to produce larger SPs than the standard PVA method, which in turn affected the optical properties of SPs produced with these methods. Average (incident) thresholds of SPs tested were estimated to be 20.1 ± 2.8, 9.2 ± 1.3 and 18.4 ± 3.5 mJ/cm^2 for PVA-, 3S- and SF-SPs respectively. Although exhibiting more favourable optical characteristics, 3S- and SF-SPs were found to be unstable towards further surface modification therefore making them unsuitable as laser biosensors.

Developing functional SP laser biosensors requires the functionalisation of the laser surface with a recognition element to enable the capture of a target analyte for detection. In this novel case, SPs were modified with the protein Neutravidin which can detect biotinylated targets through the avidin-biotin interaction. PVA-SPs after surface modification with Neutravidin (Neut-SPs) did retain lasing functionality with a threshold of 19.8 ± 2.7 mJ/cm^2 and a diameter of 2.4 μm reported. For Neut-SPs to be used as biosensors, either a biotinylated recognition element would still need to be added to the SP surface or the sensing sample would require pretreatment to be able to detect biotinylated biomarkers which is not ideal. To combat this, SPs were instead functionalised with a DNA aptamer TBA-15 using a two step process; first, a ligand exchange to replace oleic acid with MPA, then attaching TBA-15 using EDC/NHS coupling with successful surface functionalisation confirmed using FTIR spectroscopy and zeta potential measurements. SPs were found to be stable in water and ethanol, however using organic solvents and altering the pH for EDC/NHS coupling did cause SPs to disintegrate and dissolve back into CQDs therefore care must be taken when designing surface functionalisation syntheses for specific applications. The average threshold of TBA-SPs was found to be 23.7 ± 20.1 mJ/cm^2 which is comparable to the average thresholds of 16.8 ± 11.8 mJ/cm^2 and 19.7 ± 10.5 mJ/cm^2 for OA- and MPA-SPs, respectively. The positive optical properties of TBA-SPs reported with the average diameter of lasing TBA-SPs being 7.3 ± 4.7 μm indicated these SPs could be used to develop label-free laser biosensors.

In the final step, a simple proof of concept biosensing test was carried out in which TBA-SPs successfully demonstrated biosensing capabilities for the protein thrombin in solution. A redshift of 0.4 nm in 40 minutes or less was obtained for TBA-SPs after the addition of 1.5 mg/mL thrombin solutions after correction against the constant cavity degradation blueshift. This, along with the consistent and usually constant blueshifts seen with TBA-SPs in water or BSA, indicates successful selective binding of thrombin to the surface of the SP lasers. The limit of detection for these SP laser biosensors is estimated to be close to 1.5 mg/mL which leaves much to be desired, however the timescale of the wavelength shift response is very positive. Further work is required to determine the actual LoD of these sensors by carrying out more sensing experiments with more concentrations of thrombin with repeats and to develop a calibration curve which could be used to quantitatively determine thrombin concentrations in complex media. There were also anomalous blueshifts observed with lower concentrations of thrombin, before baseline correction, which requires further understanding. Once the cause of this phenomenon is identified, the detection limit of these biosensors could be further improved upon. The natural next step for these SP lasers is integration into a microlfuidic chip to create a sensing device, which could stabilise signal problems arising from sample evaporation. Further work could also integrate multiple SPs, each functionalised with different DNA aptamers, operating at different wavelengths into single microfluidic chips for multiplexed sensing of complex media.

Overall, this study is a promising first step towards creating a functional microfluidic sensing chip with such lasers and creates an exciting precedent with many different possibilities and avenues to explore for further study.

Appendix A

Data

A.1 Chapter 3

Table A.1: Diameter and threshold measurements used for the ANOVA. Measurements of SPs were taken after fabrication with the three different emulsions, the thresholds reported are those of the dominant lasing peak.

PVA-SPs		**SF-SPs**		**3S-SPs**	
Diameter (μm)	Threshold (mJ/cm^2)	Diameter (μm)	Threshold (mJ/cm^2)	Diameter (μm)	Threshold (mJ/cm^2)
4.4	25.1	17.9	28.7	15.5	9.77
10.7	35.0	18.7	21.3	13.5	7.23
13.1	42.7	7.2	29.3	7.7	4.70
9.1	23.3	9.1	26.2	23.9	5.70
9.9	30.6	9.5	16.2	22.3	7.90
11.9	23.1	6.8	16.9	29.6	7.20
5.5	2.50	17.0	21.9	36.3	14.1
10.0	2.25	19.4	6.32	19.3	13.2

Continued on next page

PVA-SPs		**SF-SPs**		**3S-SPs**	
Diameter (μm)	Threshold (mJ/cm^2)	Diameter (μm)	Threshold (mJ/cm^2)	Diameter (μm)	Threshold (mJ/cm^2)
10.3	14.4	16.1	9.72	14.5	13.2
8.5	11.3	10.3	2.50	–	–
4.5	4.31	8.4	3.19	–	–
15.5	9.77	20.0	14.4	–	–
13.5	7.23	21.3	11.3	–	–
7.7	4.70	18.1	4.31	–	–
10.2	34.3	7.5	9.23	–	–
7.9	32.0	5.3	25.8	–	–
5.6	39.2	15.1	44.7	–	–
–	–	11.3	40.2	–	–

A.2 Chapter 4

Table A.2: Diameter and Threshold measurements for all SPs tested after each step in the fabrication and surface functionalisation procedure. Where there were multiple peaks, the thresholds reported are those of the dominant lasing peak.

OA-SPs		**MPA-SPs**		**TBA-SPs**	
Diameter (μm)	Threshold (mJ/cm^2)	Diameter (μm)	Threshold (mJ/cm^2)	Diameter (μm)	Threshold (mJ/cm^2)
5.8	17.6	4.1	10.1	4.5	7.23
7.6	5.92	6.4	7.65	4.2	12.5

Continued on next page

OA-SPs		**MPA-SPs**		**TBA-SPs**	
Diameter (μm)	Threshold (mJ/cm^2)	Diameter (μm)	Threshold (mJ/cm^2)	Diameter (μm)	Threshold (mJ/cm^2)
6.4	4.78	4.1	4.58	3.6	5.63
5.5	4.10	5.8	28.6	14.2	53.9
6.8	12.4	4.8	21.2	5.0	19.9
7.0	23.1	5.5	36.6	12.3	42.8
7.3	17.8	4.5	34.4	–	–
5.8	11.1	8.8	33.7	–	–
7.9	10.4	4.5	16.0	–	–
10.0	5.31	10.3	8.96	–	–
9.7	6.32	10.3	12.8	–	–
8.5	9.72	5.5	16.6	–	–
5.5	2.50	4.8	21.6	–	–
10.0	2.25	5.1	22.6	–	–
10.3	14.4	–	–	–	–
8.5	11.3	–	–	–	–
4.5	4.31	–	–	–	–
4.6	17.0	–	–	–	–
6.2	4.27	–	–	–	–
3.5	13.1	–	–	–	–
10.2	20.3	–	–	–	–
7.9	19.0	–	–	–	–

Continued on next page

OA-SPs		**MPA-SPs**		**TBA-SPs**	
Diameter (μm)	Threshold (mJ/cm^2)	Diameter (μm)	Threshold (mJ/cm^2)	Diameter (μm)	Threshold (mJ/cm^2)
5.6	23.2	–	–	–	–
4.4	14.9	–	–	–	–
10.7	20.7	–	–	–	–
13.1	25.3	–	–	–	–
9.1	13.8	–	–	–	–
9.9	18.1	–	–	–	–
11.9	15.0	–	–	–	–
18.2	12.8	–	–	–	–
7.1	8.46	–	–	–	–
16.6	23.3	–	–	–	–
8.7	13.4	–	–	–	–

A.3 Chapter 5

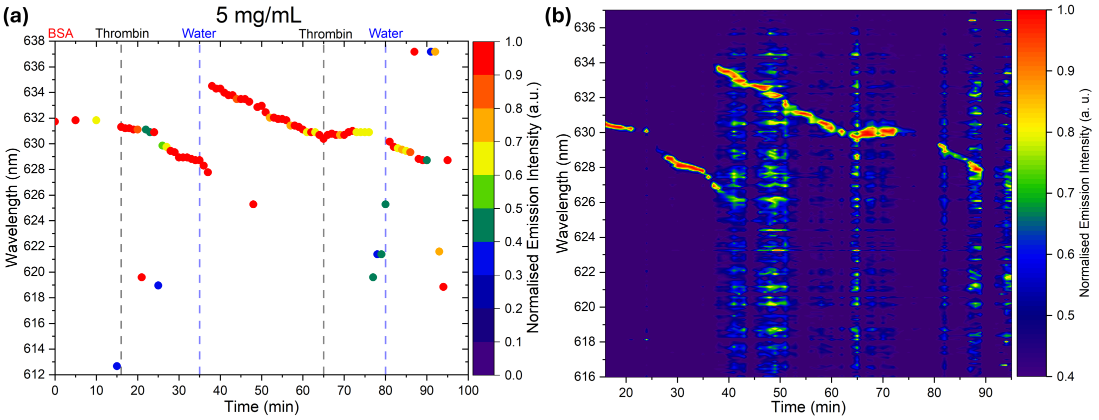

Figure A.1: Plot tracking the wavelength change over time for TBA-SP after the addition of 5 mg/mL BSA and thrombin solutions. Left is the plot of the wavelength of the peak with the highest emission against the time elapsed for TBA-SP with the time of BSA, thrombin, and water additions marked for clarity. Right is the corresponding contour map of the TBA-SP emission spectra.

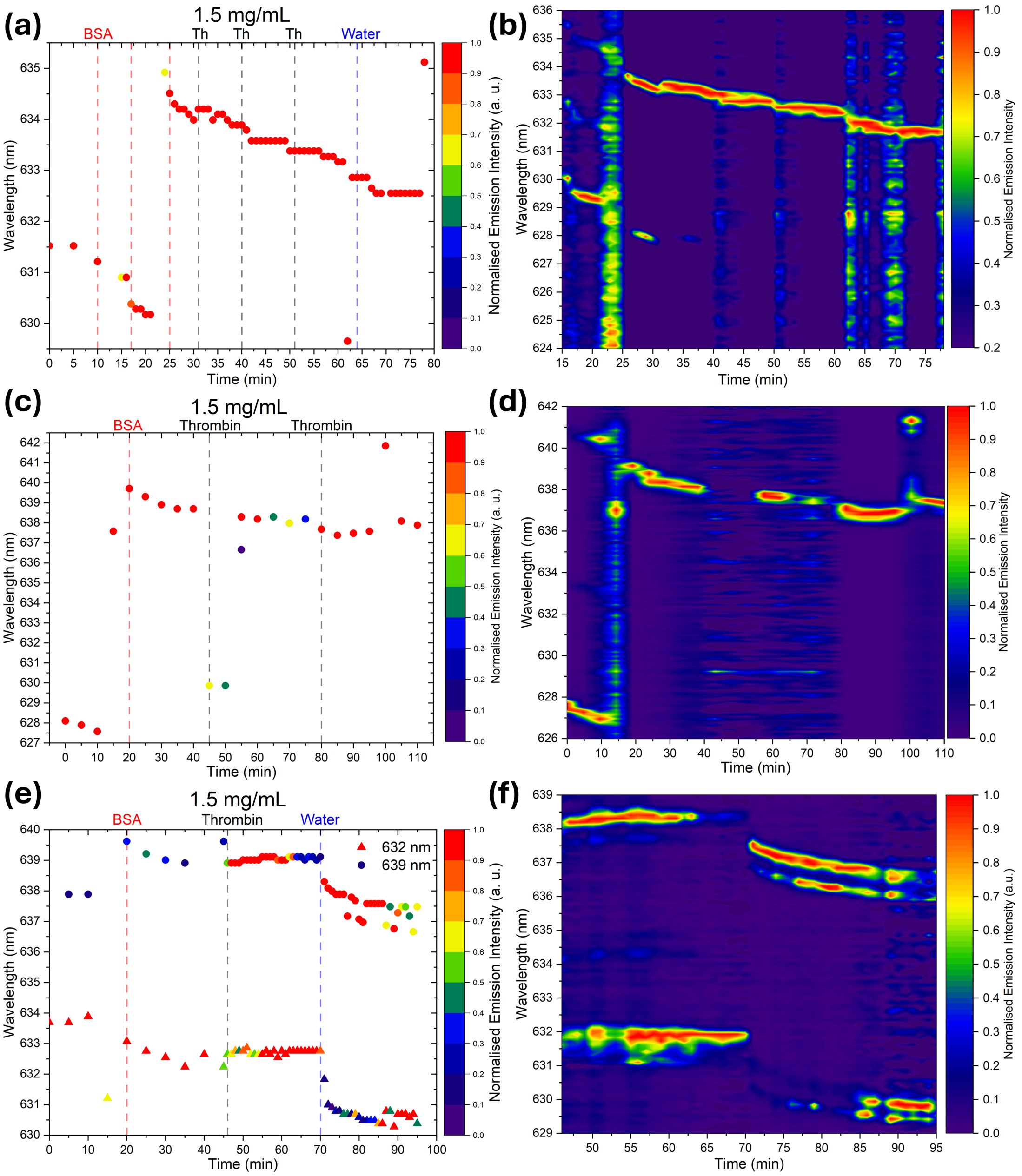

Figure A.2: Plots tracking the wavelength change over time for TBA-SPs after the addition of BSA and thrombin solutions with concentrations of 1.5 mg/mL. Left (a,c,e) are plots of the wavelength of the peak with the highest emission against the time elapsed for TBA-SPs with the time of BSA, thrombin, and water additions marked. Right (c,d,f) are the corresponding contour maps of the TBA-SP emission spectra.(f) shows the contour map only after thrombin addition for clarity.

Appendix B

List of Publications

B.1 Written Articles

B. K. Charlton, D. H. Downie, I. Noman, P. U. Alves, C. J. Eling, N. Laurand, *Int. J. Mol. Sci.*, 2023, 24(19), 14416, https://doi.org/10.3390/ijms241914416.

B.2 Oral Presentations

Charlton, B. K., Eling, C. J., Laurand, N. (2022). Surface modification of self-assembled semiconductor quantum dot microlasers. Abstract from Photon 2022, Nottingham, United Kingdom.

Charlton, B. K., Downie, D. H., Eling, C. J., Alves, P. U., Laurand, N. (2023). Impact of Surfactants in the Biofunctionalisation of Supraparticle Lasers. Abstract from NANOP, Barcelona, Spain.